Quantitative analysis of spatially resolved electroluminescence of $Cu(In,Ga)Se_2$ and a-Si:H thin-film solar cells and modules

Thi-Minh-Hang Tran

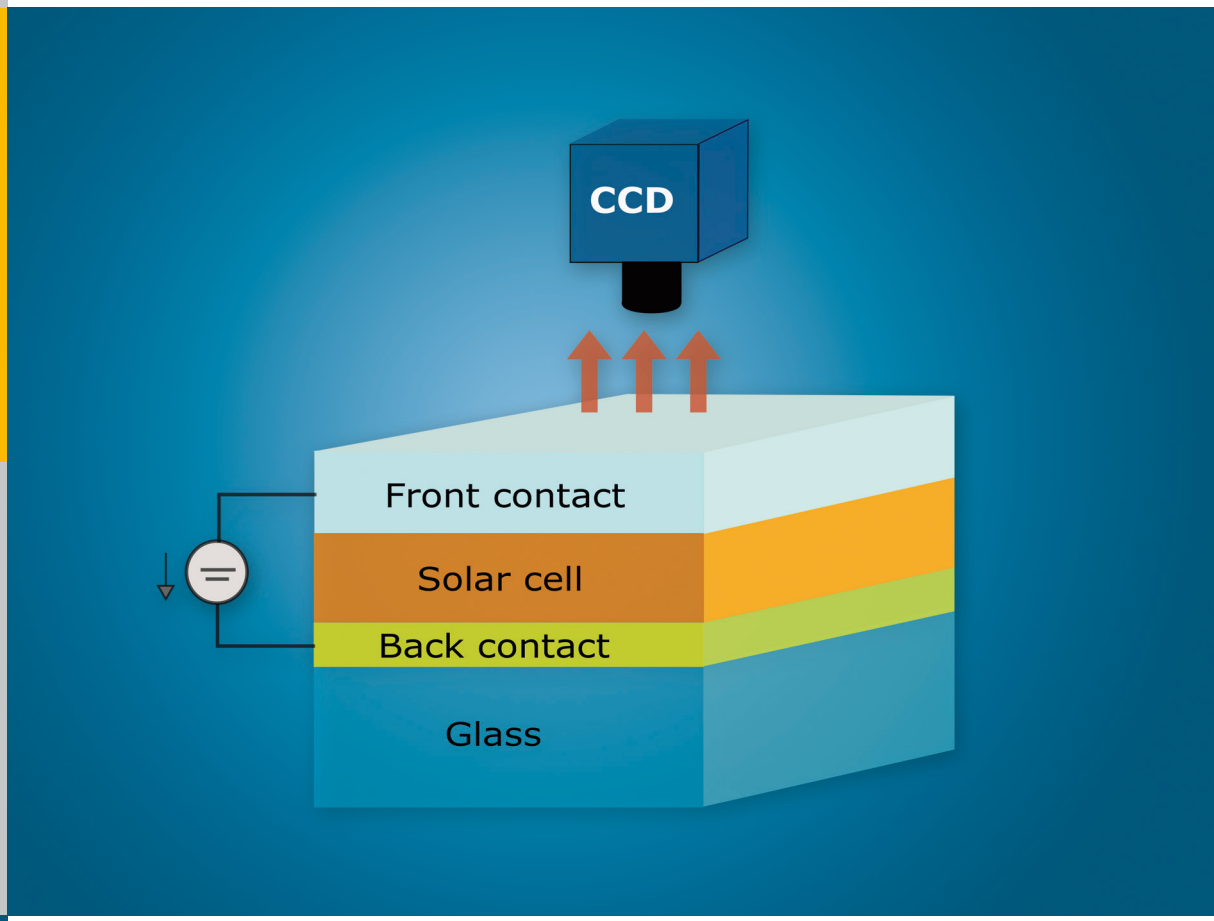

Energie & Umwelt / Energy & Environment
Band / Volume 260
ISBN 978-3-95806-050-0

JÜLICH
FORSCHUNGSZENTRUM

Schriften des Forschungszentrums Jülich
Reihe Energie & Umwelt / Energy & Environment Band / Volume 260

Forschungszentrum Jülich GmbH
Institute of Energy and Climate Research
IEK-5 Photovoltaics

Quantitative analysis of spatially resolved electroluminescence of Cu(In,Ga)Se_2 and a-Si:H thin-film solar cells and modules

Thi-Minh-Hang Tran

Schriften des Forschungszentrums Jülich
Reihe Energie & Umwelt / Energy & Environment Band / Volume 260

ISSN 1866-1793 ISBN 978-3-95806-050-0

Bibliographic information published by the Deutsche Nationalbibliothek.
The Deutsche Nationalbibliothek lists this publication in the Deutsche Nationalbibliografie; detailed bibliographic data are available in the Internet at http://dnb.d-nb.de.

Publisher and Distributor: Forschungszentrum Jülich GmbH
Zentralbibliothek
52425 Jülich
Tel: +49 2461 61-5368
Fax: +49 2461 61-6103
Email: zb-publikation@fz-juelich.de
www.fz-juelich.de/zb

Cover Design: Grafische Medien, Forschungszentrum Jülich GmbH

Printer: Grafische Medien, Forschungszentrum Jülich GmbH

Schriften des Forschungszentrums Jülich
Reihe Energie & Umwelt / Energy & Environment, Band / Volume 260

D 82 (Diss. RWTH Aachen University, 2015)

ISSN 1866-1793
ISBN 978-3-95806-050-0

The complete volume is freely available on the Internet on the Jülicher Open Access Server (JuSER) at www.fz-juelich.de/zb/openaccess.

This work is dedicated to my family.

"Your work is to discover your world and then with all your heart give yourself to it."

Buddha Shakyamuni

Contents

Abstract

Electroluminescence (EL) is the reciprocal process of the standard operational mode of a solar cell. EL imaging technique allows a fast detection of defects in solar cells and modules with low noise and high resolution. Recently, EL has become one of the most commonly used characterization tools for photovoltaic devices. There has been a significant amount of research into the interpretation and analysis of EL of silicon wafers, solar cells and modules, but very little, to date, on thin-film solar technologies. This work presents a number of varied applications of EL imaging to the analysis of both industrially produced copper indium gallium diselenide Cu(In,Ga)Se_2 (CIGS), and in-house produced hydrogenated amorphous silicon (a-Si:H) thin-film solar cells and modules.

The quantitative interpretation of the EL intensity and spectrum is based on the reciprocity theorem, which relates the EL emission with the external photovoltaic quantum efficiency of the device. In this work, this theorem is validated for industrially produced CIGS solar cells using spectrally resolved EL and photoluminescence (PL). The validation shows that PL and EL emission obeys a linear superposition in a limited range of the applied bias or illumination.

The metastable effects are also observed via EL and PL spectroscopy measurements, i.e., the increase of the luminescence efficiency by a factor of three by light soaking experiments. The metastable changes were also observed in a series of successive EL images of a CIGS module. The experiments are conducted in the dark either under constant current or constant voltage. For both situations, the EL intensities increase with the exposure time, whereas a decrease of the overall measured module voltage (at constant current) or an increase of the measured current (at constant voltage) is observed. These observations are ascribed to the simultaneous decrease of the bulk series resistance R_s and the reduction of recombination currents (an increase in the junction resistance R_j) during the forward bias experiments. A

quantitative analysis of the data shows that the reduction of R_s is much stronger than the increase of R_j. This analysis also shows that the bulk series resistance hampers the determination of the sheet resistance of the front ZnO contact from EL images.

Resistive defects (shunts) in CIGS solar modules significantly affect the module efficiency. The combination of EL and dark lock-in thermography (DLIT) imaging techniques is a useful method for the investigation of such defects. In EL images, the effects of shunts on the neighboring cells in the module (the so-called cross-talk effect) are clearly visible. Lock-in thermography is well suited for the localization and determination of the geometry of the shunts. With the help of a simulation model using a network simulation method (NSM)-based tool with a variable, adaptive mesh, the values of the sheet resistances of the front and back electrodes are determined. The analysis of the simulation results shows consistent modelling of EL and DLIT images for CIGS devices. The experimental and simulation results are in a good agreement. A measure for the cross-talk effect is also defined from the simulation results. Furthermore, the junction voltage of the shunted cell is strongly affected by the neighboring cells, and increasing the sheet resistances of the front and back electrodes can reduce the losses of the junction voltage.

A classification of defects in CIGS modules using EL imaging is shown in this thesis. We classified four types of defects, which are named according to their respective appearance in EL images as 'Normal shunts', 'Smears', 'Freckles', and 'Doughnuts'. Normal shunts strongly affect the performance of the cells and modules. In both EL and LIT images, Smears appear as strong shunts, which also affect the device performance. Freckles are defects, which appear as very weak shunts in DLIT images and seem to be primarily caused by differences in emissivity. A large amount of Freckles will reduce the short circuit current of the device. Doughnuts may originate from impurities or difference in material properties of the device and also affect the device performance.

This thesis also presents a method for extracting the absolute local junction voltage of *a*-Si:H thin-film solar cells and modules from EL images. It is shown that the EL emission of *a*-Si:H devices follows a diode law with a radiative ideality factor n_r larger than one. In this work, an evaluation method that allows the determination of the absolute local junction voltage in cases of $n_r > 1$ is developed, while existing

approaches rely on the assumption of $n_r = 1$. Furthermore, the experimentally determined values of n_r are found to vary from sample to sample. It is also explained why the derived radiative ideality factor is influenced by the spectral sensitivity of the camera system used in the experiment.

Zusammenfassung

Elektrolumineszenz (EL) ist die Umkehrung des Prozesses, der normalerweise in einer Solarzelle auftritt. In letzter Zeit wurde EL zu einem der meistgenutzten Werkzeuge zur Charakterisierung von photovoltaischen Bauelementen. Es gab ausgiebige Forschung im Bereich der Interpretation und Anlyse von EL für Siliziumwafer, -zellen und module. Bisher allerdings wurde EL für Dünnschichtsolarzellen nur sehr wenig erforscht. Diese Arbeit zeigt eine Reihe von verschiedenen Anwendungen von bildgebenden EL-Verfahren auf die Analyse von Kupfer-Indium-Gallium-Diselenid $Cu(In,Ga)Se_2$, wie sie in der Industrie hergestellt werden, sowie von vor Ort produzierten amorphen Silizium (a-Si:H) Dünnschichtsolarzellen und -modulen.

Die quantitative Interpretation des EL-Signals basiert auf dem Reziprozitätstheorem, das die EL-Emission mit der externen photovoltaischen Quanteneffizienz korreliert. In dieser Arbeit wird dieses Theorem für industriell gefertigte CIGS-Solarzellen mithilfe von spektral aufgelöster Photolumineszenz (PL) bestätigt. Diese Bestätigung zeigt, dass PL- und EL-Emission einer linearen Superposition gehorchen, zumindest in einem begrenzten Bereich der angelegten Spannung und der Beleuchtung. Metastabile Effekte können ebenfalls per EL und PL beobachtet werden, z.B. die Erhöhung der Lumineszenzeffizienz nach Light-Soaking Experimenten um einen Faktor drei. Solche metastabilen Änderungen konnten auch in einer Reihe aufeinanderfolgender EL-Messungen eines CIGS-Moduls beobachtet werden. Die Experimente dazu wurden in Dunkelheit entweder unter konstantem Strom oder konstanter Spannung durchgeführt. In beiden Fällen erhöht sich die EL-Intensität mit der Belichtungszeit, wobei insgesamt eine Verringerung der am Modul gemessenen Spannung (konstanter Strom) oder eine Erhöhung des gemessenen Stroms (konstante Spannung) beobachtet wird. Diese Beobachtung kann durch die gleichzeitige Verringerung des bulk-Serienwiderstandes R_s und die Reduktion der Rekombinationsströme (Erhöhung des Übergangswiderstandes R_j während der Experimente

unter Bias-Spannung) erklärt werden. Eine quantitative Analyse der Daten zeigt, dass die Verringerung von R_s wesentlich stärker ist als die Erhöhung von R_j. Diese Analyse zeigt auch, dass der aus der EL für den transparenten Frontkontakt ermittelte Schichtwiderstand von R_s stark verfälscht werden kann.

Defekte mit hohem Widerstand (shunts) in CIGS-Modulen zeigen einen Einfluss auf die Moduleffizienz. Die Kombination aus bildgebender EL und Dunkel-Lock-In-Thermographie (DLIT) zeigen eine nützliche Methode, solche Defekte zu untersuchen. In EL-Bildern sind die Effekte von Shunts auf die benachbarten Zellen des Moduls (sog. Cross-Talk-Effekt) sehr gut sichtbar. DLIT ist dabei sehr gut geeignet, die Geometrie der Shunts zu ermitteln. Mithilfe von Simulationen, die die Network-Simulation-Methode (NSM) mit einem variablen, adaptiven Mesh nutzen, können die Schichtwiderstände der Front- und Rückelektroden ermittelt werden. Die Analyse der Simulationen zeigt, dass der Cross-Talk von den Shunts, dem Schichtwiderstand der Elektroden, sowie der Geometrie der Zellen und Module abhängt.

Eine Klassifikation der Defekte in CIGS-Modulen via EL wird ebenfalls in dieser Arbeit präsentiert. Dabei werden vier verschiedene Arten von Defekten klassifiziert, die nach ihrem Erscheingungsbild in EL-Bildern benannt sind: 'Normale Shunts' (Normal shunts) ,'Schweif' (Smears), 'Flecken' (Freckles) und 'Donuts' (Doughnuts). Normale Shunts beeinflussen die Leistung der Zellen stark. Schweife erscheinen sowohl in EL-, als auch in DLIT-Bildern als starke Shunts, die ebenfalls die Leistung des Bauelements beeinflussen. Flecken sind Defekte die aus der uterschiedlichen Emissivität der Materialien herrühren können. Eine große Anzahl dieser Flecken reduziert die Kurzschulssstromdichte des Moduls. Donuts können von Verunreinigungen oder unterschiedlichen Materialeigenschaften des Bauelements herrühren und beeinflussen auch die Leistung.

Weiterhin wird in dieser Arbeit eine Methode gezeigt, die absoluten lokalen Übergangsspannungen von a-Si:H Dünnfilmsolarzellen und -modulen aus EL-Bildern zu extrahieren. Es wird gezeigt, dass die EL-Emission eines a-Si:H Bauelements einem Diodengesetz mit einem Idealitätsfaktor n_r größer eins folgt. Eine Auswertung wird vorgestellt, die es erlaubt, die absolute Übergangsspannung zu ermitteln, falls $n_r > 1$ gilt, während existierende Ansätze auf die Annahme $n_r = 1$ angewiesen sind. Es wird außerdem geklärt, warum der abgeleitete strahlende Idealitätsfaktor von der spektralen Empfindlichkeit der genutzten Kamera abhängt.

1. Introduction

The world energy consumption is rapidly increasing and will grow by 56% between 2010 and 2040 [1]. Besides the developed countries, the emerging and developing countries are becoming important energy consumers. For example, in 2003 China had already become the world's second largest consumer with 12.1% of the world's energy consumption, second only to the United States [2]. Nowadays, almost 80% [3, 4] of the world energy consumption is still generated by fossil resources. The production of conventional energy has a considerable impact on the environment, e.g. global warming and climate change [5]. This, combined with the shortage of fossil resources, is the driving force to develop alternative energy generation methods. Renewable energies, such as wind energy, hydro-power, biomass, and solar energy, etc., have become promising alternative energy, as they already provide 16% of the total world energy supply [4]. Moreover, they are renewable resources, and cause much less CO_2-emission than their fossil fuel counterparts. References [6, 7] give a brief discussion about different renewable energy technologies. Between 2006 and 2011, the global photovoltaic (PV) capacity increased dramatically by an average of 58% annually, the fastest growth of all renewable technologies [4]. Thus, solar energy will contribute an essential part to meet the world energy needs.

The PV market is dominated by crystalline silicon (c-Si) solar cells, which holds more than 86% of the market share, whereas thin-film solar technologies have approximately 14% [8]. The aim of using thin-film technologies is to reduce the production costs and save materials. The maximum theoretical energy conversion efficiency of an ideal (Shockley and Queisser) single p-n junction solar cell is approximately 31% [9]. The record efficiencies of cells and modules of different solar cell devices are given in Refs. [10–15]. The record lab cell efficiency of mono-crystalline silicon (c-Si) is 25% [10,11,14], of cadmium telluride (CdTe) thin-film cell is 18% [12], and of single hydrogenated amorphous silicon (a-Si:H) thin-film solar cell is 10.3%

(stable) [16]. A world record efficiency for polycrystalline thin-film solar cells of 20.3% had been reported for a $Cu(In,Ga)Se_2$ (CIGS) thin-film solar cell deposited onto a glass substrate [15]. Recently, a new record efficiency for CIGS solar cells of 20.8% had also been reported [17] from the same research group. This record efficiency is also the highest efficiency achieved for all thin-film technologies. However, typical achievable efficiencies of large-area (30×30 cm^2) CIGS solar modules are about 12-15% [18–20]. The significant deviation between the efficiencies of the record CIGS solar cell and of large-area industrially fabricated solar modules mostly results from defects, such as shunts or impurities. Therefore, it is of the utmost importance to understand the physics and the origin of defects to optimize the efficiencies of the devices. This thesis investigates defects in CIGS solar devices using spatially resolved EL. Furthermore, EL imaging is also used for the quantitative analysis of both CIGS and *a*-Si:H thin-film devices.

Many characterization techniques can be used to explore the optical, physical, as well as electrical properties of the solar devices. These can be divided into two types, namely, spatially and non-spatially resolved methods. The spatially resolved methods are useful for identifying the location and effect of defects. These can also be divided into scanning and imaging methods. Scanning methods measure the sample point by point. Commonly used scanning methods include laser-beam-induced-current (LBIC) [21, 22], electron-beam-induced-current (EBIC) [23], microwave photoconductance decay (μPCD) [24], CoreScan [25], and Cello [26]. These techniques can provide detailed information at high resolution, but are usually very time-consuming, with measurement times in the order of hours for large-scale solar modules. Using camera-based (imaging) methods, such as lock-in thermography (LIT) [27], photoluminescence (PL) imaging [28, 29] and electroluminescence (EL) imaging [30, 30–42], the entire sample is recorded at once, which drastically reduces the measurement time down to minutes or even seconds for a large-scale solar module.

This work focuses on different applications of spatially resolved EL, for the characterization of both CIGS and *a*-Si:H thin-film solar cells and modules. The specific thesis structure is outlined as follows.

Chapter 2 gives a brief description of the theoretical background of solar cells, which is important for understanding both experimental and simulation results

presented in this work. First of all, this chapter introduces the basic operation principle of a solar cell. For the analysis of the EL measurement results in this thesis, the reciprocity theorem [43, 44] and its application are described in detail. The samples used for this work are CIGS and *a*-Si:H thin-film devices, therefore, their device structure and manufacturing processes are briefly shown.

In **chapter 3**, the setups and working principles of the characterization techniques such as spatially resolved EL, PL and EL spectroscopy and DLIT used in this work are also described in detail.

Chapter 4 concentrates on the analysis of the EL and PL spectra of CIGS solar cells measured at room temperature ($T = 300$ K) and the quantitative analysis of the transient EL images. As the results of these analyses, the reciprocity theorem is validated for the industrially produced CIGS solar cells. Additionally, the metastable effects in CIGS solar cells and modules under illumination and bias are observed via both EL and PL spectroscopy and EL imaging. The metastable changes of the EL intensity are ascribed in terms of the various sample resistances.

In **chapter 5**, a detailed study of commonly observable shunts in EL images of a (30×30 cm^2) CIGS module is presented by combining both EL and LIT imaging. A simulation tool based on the network simulation method (NSM) using a variable, adaptive mesh [45] is also used to determine the local EL intensity, the local voltage and the local dissipated power densities. From the experimental and simulation results, the sheet resistances of the front and the back contacts, the series resistance of the bulk, as well as the shunt geometry and shunt resistances are determined. The analysis of different simulations shows that shunts induce the so-called cross-talk effects, which depend on the current flow across the shunts, the sheet resistances of both the front and back contacts, and the geometry of the devices.

Chapter 6 presents a classification of several common defects in CIGS modules that are visible in EL images. Additionally, various characterization techniques are also introduced, such as LIT, EL and PL imaging and spectroscopy, and scanning electron microscopy (SEM) to analyze the structural, electrical and optical properties of the defects.

In **Chapter 7**, a method to determine the absolute local junction voltage from the EL images of *a*-Si:H solar cells and modules is developed.

Conclusions and possibilities for future work are presented in **Chapter 8**.

2. Fundamentals

This chapter is dedicated to the theory necessary to understand this thesis. Firstly, a brief description of the basic operational principle of a solar cell such as light absorption and emission is given. The reciprocity theorem [43] is introduced. It describes the relation between the external quantum efficiency of a solar cell and electroluminescence (EL) resulting from the radiative recombination process within a solar cell. The reciprocity theorem enables the quantitative analysis of the experimental results from both spatially and spectrally resolved EL measurements. Since this work mainly focuses on two thin-film technologies, namely, Cu(In,Ga)Se_2 (CIGS) and hydrogenated amorphous silicon (a-Si:H), their device structures and the electrical characterizations are briefly explained.

2.1. Light absorption and emission in solar cells

Solar cells are opto-electronic devices, which convert energy from incoming photons into electrical energy. Photons which enter the solar device, are absorbed and generate electron/hole (n/p)-pairs, which are extracted from the absorber to the front and back contacts. The reciprocal conversion process is called electroluminescence (EL), where charge carriers (n/p)-pairs are injected into the device, radiatively recombine, and finally the generated photons are emitted. The radiative recombination process is given in detail in Sec.2.1.3. In this section, absorption and emission, which play an important role in the conversion processes in a solar cell and in EL, are briefly introduced.

Thermal equilibrium

In thermal equilibrium, the relation between absorption and emission is described by Kirchhoff's law [46], which states that the emissivity $\zeta(E)$ of an arbitrary body

at an energy interval E equals its absorptance $a(E)$, i.e. the ratio of absorbed radiation to incident radiation at the same energy. Kirchhoff's law describes the thermal emission $\phi_{em}(E)$, which is given by

$$\phi_{em}(E) = \zeta(E)\phi_{bb}(E) = a(E)\phi_{bb}(E). \tag{2.1}$$

The black-body spectrum $\phi_{bb}(E)$ is described by Planck's law [47]

$$\phi_{bb}(E) = \frac{2\pi E^2}{h^3c^2[\exp(\frac{E}{kT}) - 1]} \approx \frac{2\pi E^2}{h^3c^2}\exp(\frac{-E}{kT}), \tag{2.2}$$

where $h = 4.136 \times 10^{-16}$ eVs is the Planck's constant, $c_0 = 2.998 \times 10^{10}$ cm/s the vacuum speed of light, $k = 8.617 \times 10^{-5}$ eV/K the Bolzmann constant, and T the temperature. Planck's law is derived from Kirchhoff's law for a black body, which absorbs all the incoming light in thermal equilibrium and emits the same radiation spectrum it absorbs, i.e. $a(E) = 1$.

Non-thermal equilibrium

Kirchhoff's and Planck's laws are only valid in thermal equilibrium. For non-thermal equilibrium, Planck's law has been generalized for non-thermal radiation by Würfel [48] by introducing a non-zero chemical potential μ of radiation, which equals the quasi-Fermi level splitting ΔE_F. The splitting of the quasi Fermi-level ΔE_F results from the injected electron and hole concentrations n and p, under illumination or an applied forward voltage V.

The emission $\phi_{em}(V, E)$ of non-thermal radiation under an applied voltage V is described by Würfel's generalized Planck's law [48]

$$\phi_{em}(V, E) = a(E)\phi_{bb}(E)\exp(qV/kT). \tag{2.3}$$

The exponential factor $\exp(qV/kT)$ in Eq. (2.3) is given by the electron and hole concentrations in non-thermal equilibrium, n and p, respectively, and the electron and hole concentrations in thermal equilibrium n_0 and p_0, respectively.

The concentrations of electrons n and holes p are the functions of the quasi-Fermi levels E_{Fn} and E_{Fp} of electrons and holes, which are defined as

$$n = N_C \exp\left(-\frac{E_C - E_{Fn}}{kT}\right), \tag{2.4}$$

$$p = N_V \exp\left(-\frac{E_{Fp} - E_V}{kT}\right), \tag{2.5}$$

where N_C and N_V are the effective densities of states in the conduction and the valence bands, and E_C and E_V are the conductance band minimum and the valence band maximum energies. The product of n and p is written as

$$np = N_C N_V \exp\left(-\frac{E_g}{kT}\right) \exp\left(\frac{E_{Fn} - E_{Fp}}{kT}\right). \tag{2.6}$$

Here, $E_g = E_C - E_V$ is the band-gap energy. The quasi-Fermi level splitting ΔE_F is the difference between the quasi-Fermi levels E_{Fn} and E_{Fp} of electrons and holes, respectively, or $\mu = \Delta E_F = E_{Fn} - E_{Fp}$.

Under an applied voltage V, the product np is written as

$$np = N_C N_V \exp\left(-\frac{E_g}{kT}\right) \exp\left(\frac{qV}{kT}\right). \tag{2.7}$$

For flat quasi-Fermi levels and, therefore, a constant quasi-Fermi level split $\Delta E_F = E_{Fn} - E_{Fp}$ equals qV.

Furthermore, in thermal equilibrium, the concentrations of electrons n_0 and holes p_0 are given by

$$n_0 = N_C \exp\left(-\frac{E_C - E_F}{kT}\right), \tag{2.8}$$

$$p_0 = N_V \exp\left(-\frac{E_F - E_V}{kT}\right). \tag{2.9}$$

The product of the equilibrium electron and hole concentrations n_0 and p_0 is given as

$$n_0 p_0 = n_i^2 = N_C N_V \exp\left(-\frac{E_g}{kT}\right), \tag{2.10}$$

where n_i is the intrinsic carrier density.

Using Eqs . (2.10) and (2.7), the product of n and p shown in Eq. (2.7) can be written as

$$np = n_i^2 \exp\left(\frac{qV}{kT}\right). \tag{2.11}$$

The exponential term $\exp(qV/kT)$ is therefore the ratio of the product np in non-thermal equilibrium to the product $n_0 p_0$ in equilibrium.

Equation (2.1) describes the thermal emission in the thermodynamic equilibrium. In non-thermal equilibrium, electroluminescence results from the radiative

recombination of electrons and holes under an applied forward voltage V and is larger than the thermal emission by an exponential factor $\exp(qV/kT)$ in Eq. (2.3). Equation (2.3) is a prerequisite for the derivation of the reciprocity theorem shown in Sec.2.2, which plays an important role for the quantitative analysis conducted in this thesis.

2.1.1. Direct and indirect semiconductors

In a semiconductor, light absorption and emission depend on the wavevector k, i.e. a vector, which has a magnitude ($k = 2\pi/\lambda$, where λ is the wavelength of the traveling wave), and gives the direction of the wave propagation.

Direct semiconductors have the maximum of the valence band and the minimum of the conduction band at the same wavevector k. Therefore, the transition of an electron between the valence band and conduction band occurs without phonon interaction, which means that the radiative recombination process is dominant in direct semiconductors. The absorption coefficient α_{dir} of a direct semiconductor material is given as

$$\alpha_{\mathrm{dir}} \propto \sqrt{(h\nu - E_{\mathrm{g}})}. \tag{2.12}$$

In indirect semiconductors, the maximum of the valence band and the minimum of the conduction band are at different wavevectors k. To excite an electron from the valence band into the conduction band at different wavevector values, a phonon with an energy E_{p} must be either absorbed or emitted. The absorption of a phonon decreases lattice vibrations, whereas the emission of a phonon increases lattice vibrations. Radiative recombination in indirect semiconductors is low compared to that in direct semiconductors. The absorption coefficient α_{ind} of an indirect semiconductor material is given as

$$\alpha_{\mathrm{ind}} \propto (h\nu - E_{\mathrm{g}} - E_{\mathrm{p}})^2, \tag{2.13}$$

$$\alpha_{\mathrm{ind}} \propto (h\nu - E_{\mathrm{g}} + E_{\mathrm{p}})^2, \tag{2.14}$$

for phonon emission and phonon absorption, respectively.

Figure 2.1 shows absorption coefficient and absorption length of both direct and indirect semiconductor devices versus photon energy E. Figure 2.1 depicts that direct semiconductors such as $CuInSe_2$ shows a steeper increase of the absorption

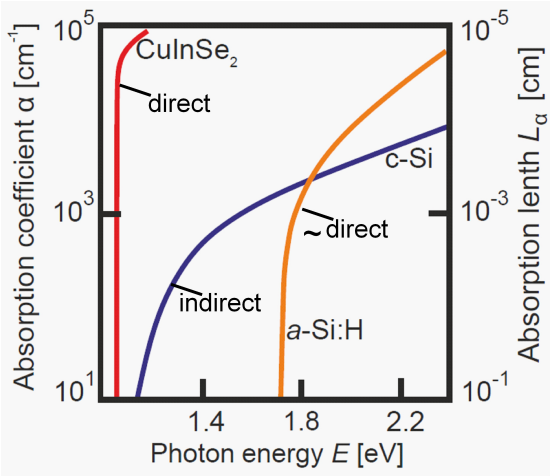

Figure 2.1.: Absorption coefficient and absorption length of $CuInSe_2$, c-Si and *a*-Si:H devices, illustrated after [49]. Direct semiconductors such as $CuInSe_2$ show steeper increase of the absorption coefficient, and consequently a smaller absorption length at the band-gap than that of the indirect semiconductors.

coefficient with respect to small increase of the photon energy E than that of indirect semiconductors, e.g. c-Si. Direct semiconductor materials have larger absorption coefficient α close to their band-gap energy, i.e. a stronger light absorption. Since the absorption length L_α is inversely proportional to the absorption coefficient α, the indirect-semiconductors have longer absorption length than the direct semiconductors. $Cu(In,Ga)Se_2$ (CIGS) is a direct semiconductor. Hydrogenated amorphous silicon (*a*-Si:H) is a quasi-direct semiconductor. This work focuses on the analysis of EL measurements of CIGS and *a*-Si:H devices.

2.1.2. p-n and p-i-n junctions

Figure 2.2 shows the banddiagrams of various types of p-n-junctions such as p-n homojunction, p-n heterojunction, and p-i-n heterojunction, which are described in detail below.

A p-n homojunction shown in Fig. 2.2(a) is formed by connecting a p-type

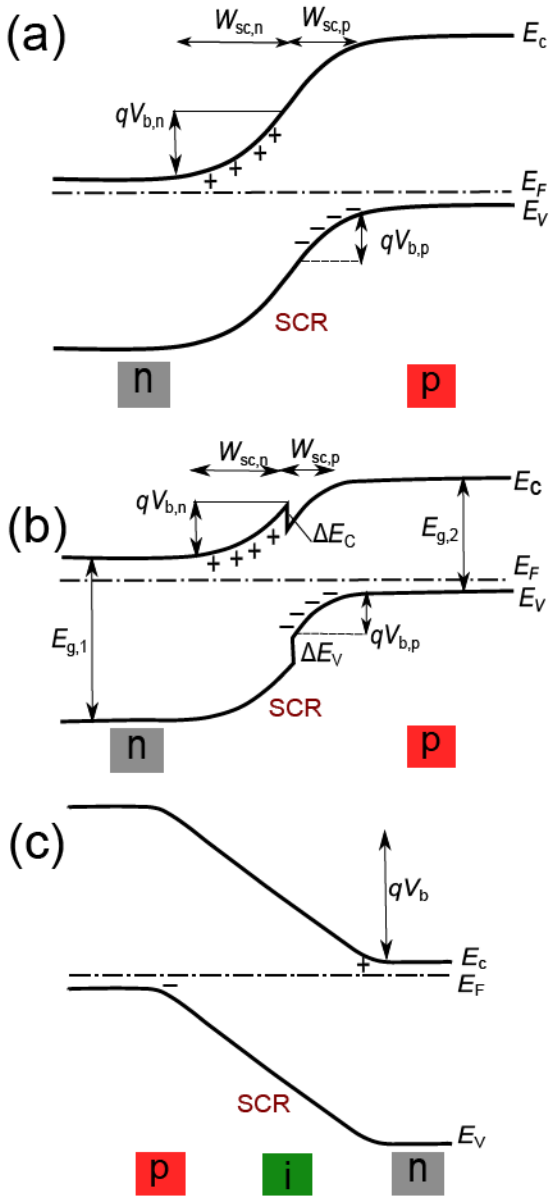

Figure 2.2.: Banddiagrams of (a) a p-n homojunction, (b) a p-n heterojunction [49], and (c) a p-i-n heterojunction.

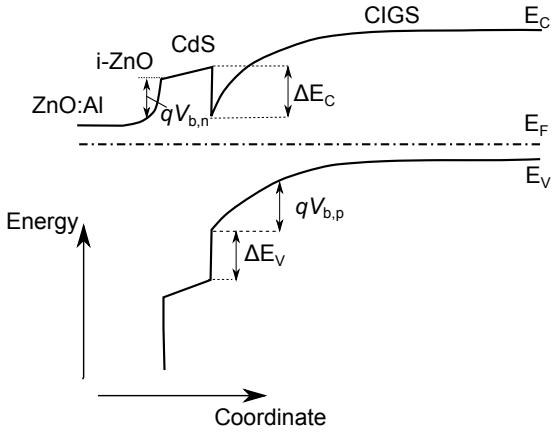

Figure 2.3.: Banddiagram of a CIGS heterojunction solar cell with valence band and conduction band discontinuities.

doped and an n-type doped semiconductor, which allows the diffusion of electrons into the p-type material, holes into the n-type material due to concentration gradients. By this diffusion process, electrons and holes leave behind ionized shallow donors and acceptors, respectively. This process results in a depletion region, also called the space charge region (SCR). In the SCR, an electric field is created due to the ionization of positive donors and negative acceptors, which prevents the diffusion of further electrons into the p-region and holes into the n-region. The width of the SCR depends on the doping concentration. The total width of the SCR is the sum of the widths of the space charge regions $W_{\mathrm{sc,p}}$ and $W_{\mathrm{sc,n}}$ in p-type and n-type region, respectively.

The Fermi energy level E_{F} is shown in Fig. 2.2(a). The built-in voltage is the sum of the built-in voltages of the n- and the p-type regions ($V_{\mathrm{b,n}} + V_{\mathrm{b,p}}$). Typical solar devices with a p-n homojunction structure are for example crystalline silicon solar cells.

Figure 2.2(b) shows the banddiagram of a p-n heterostructure. In contrast to a homojunction, a heterojunction is formed if two semiconductor materials with different band-gap energies $E_{\mathrm{g},1}$ and $E_{\mathrm{g},2}$ are brought into contact. A CIGS device consisting of several layers from various materials is an example for a p-n heterostruc-

ture. The band diagram of a heterojunction ZnO/CdS/CIGS solar cell is shown in Fig. 2.3. More details on the device structure of a CIGS solar cell is given in Sec.2.3.1. The front contact layers from ZnO:Al and i-ZnO have a band-gap energy of $E_{\mathrm{g,ZnO}} = 3.3$ eV and $E_{\mathrm{g,ZnO:Al}} = 3.3$ eV [50]. The CdS buffer layer has a band-gap energy of approximately $E_{\mathrm{g,CdS}} = 2.4$ eV [50]. The band-gap of the CIGS absorber layer can range from $E_{\mathrm{g}} \approx 1.02$ eV to 1.7 eV, depending on the Ga-content [51, 52]. The conduction band discontinuity ΔE_{C} at the absorber(CIGS)/buffer(CdS) layer is approximately 0.3 eV [53]. The valence band discontinuity ΔE_{V} is ≈ -0.8 eV [53].

For *a*-Si:H thin-film solar cells, a p-n junction structure is not as effective as for other solar technologies. The main reason is the poor electronic properties of the doped layers. In addition it can be beneficial for a low mobility device as *a*-Si:H to have a wide SCR. Therefore, a p-i-n junction structure as shown in Fig. 2.2(c) is used to enlarge the depletion region. Additionally, the i-layer has a low defect density, and therefore, the lifetime of the photogenerated charge carriers can be increased.

2.1.3. Recombination processes

In this section, various recombination processes are briefly presented. Recombination is the reciprocal process of generation of electron-hole pairs. During the recombination process, electrons in the conduction band or in defect levels (traps) within the band-gap are captured by holes in traps or in the valence band and/or holes in the valence band can be captured by electrons in traps. Figures 2.4(a-c) illustrate radiative (band-to-band) recombination, Auger and Shockley-Read-Hall (SRH), respectively.

In this thesis, radiative recombination is an important recombination process because it is the fundamental process for luminescence. Radiative recombination occurs when an electron n in the conduction band recombines with a hole p in the valence band, and thereby, emits a photon γ (see Eq. (2.15)) [54]. In direct band-gap semiconductors, such as $Cu(In,Ga)Se_2$, the radiative recombination mechanism is the dominant recombination process.

$$n + p \rightarrow \gamma. \tag{2.15}$$

The radiative recombination rate at which electrons and holes recombine are

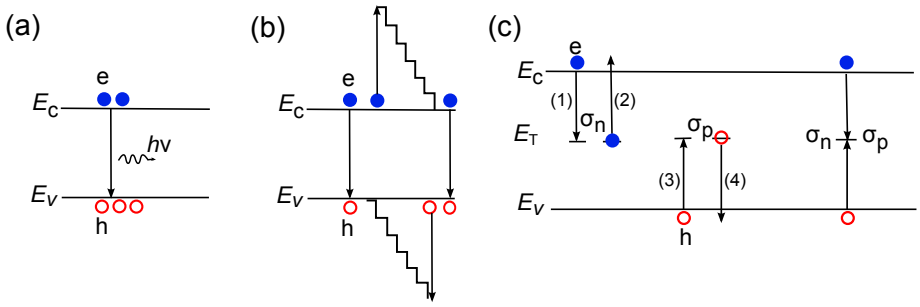

Figure 2.4.: Recombination mechanisms in semiconductors: (a) Band-to-band recombination, (b) Auger recombination, (c) Shockley-Read-Hall (SRH) recombination.

proportional to the carrier densities

$$R_{\mathrm{r}} = Bnp. \tag{2.16}$$

Here B is the bimolecular recombination constant, n is the density of electrons and p is the density of holes. From Kirchhoff's law and the detailed balance principle [55], at equilibrium, the radiative recombination rate R_0 equals the generation rate G_0

$$R_0 = \frac{n_0}{\tau} = \int_0^\infty \alpha \phi_{\mathrm{bb}}(E) dE = G_0, \tag{2.17}$$

where n_0 is the equilibrium concentration of minorities, τ is the lifetime of minority carriers, and α is the absorption coefficient. Under a forward applied voltage V, the radiative recombination rate $R_{\mathrm{r}}(x)$ at position x depends on the concentration of excess minority carriers Δn. From Eq. (2.17), it follows

$$R_{\mathrm{r}}(x) = \frac{\Delta n(x)}{\tau}. \tag{2.18}$$

Auger recombination requires three carriers. An electron and a hole recombine in a band-to-band transition and then the resulting energy is transferred to a third electron or hole. Therefore, the Auger recombination rate for electrons is similar to that of band-to-band recombination, which receives the resulting energy from the electron-hole recombination. The Auger recombination rate is given by

$$R_{\mathrm{Aug}} = C_{\mathrm{n}} n^2 p + C_{\mathrm{p}} p^2 n, \tag{2.19}$$

where C_n and C_p are the coefficients of the Auger recombination for electrons and holes, respectively. Auger recombination depends strongly on the doping concentration. For n-type semiconductors with $n \gg p$, then R_{Aug} is proportional to n^2. Analogously, for p-type semiconductor ($p \gg n$), R_{Aug} is proportional to p^2. Auger is the dominant recombination mechanism in indirect semiconductor such as silicon solar cells.

Shockley-Read-Hall (SRH) recombination is recombination through defect levels caused by the presence of impurities, e.g. foreign atoms, or structural defects (see Fig. 2.4(c)). The SRH recombination process requires two particles and occurs via trap energy levels E_T within the band-gap. The possible processes are
(1) an electron from the conduction band can be trapped by an empty trap,
(2) a filled trap can emit an electron back into the conduction band,
(3) an empty trap can capture a hole from the valence band,
(4) a trap filled with a hole can emit a hole back into the valence band.

The recombination rate R_{SRH} is given by [56]

$$R_{SRH} = \frac{np - n_i^2}{(n + n_1)\tau_p + (p + p_1)\tau_n}, \tag{2.20}$$

where n, p are the density of the electrons and holes, τ_p, τ_n are the life time of the holes and electrons, respectively. The parameters p_1 and n_1 are the hypothetical hole and electron concentrations in the valance band and the conductance band, respectively, if $E_F = E_T$. It follows

$$n_1 = N_C \exp\left(-\frac{E_C - E_T}{kT}\right), \tag{2.21}$$

$$p_1 = N_V \exp\left(-\frac{E_T - E_V}{kT}\right). \tag{2.22}$$

The lifetimes of the excess minority hole and electron, respectively, are defined by

$$\tau_p = (N_T \sigma_p v_{th})^{-1} \tag{2.23}$$

$$\tau_n = (N_T \sigma_n v_{th})^{-1}, \tag{2.24}$$

where N_T is the trap density, σ_p, σ_n are the hole and electron capture cross sections, and v_{th} is the carrier thermal velocity [56].

2.2. Applications of the reciprocity theorem

This section presents the reciprocity theorem [43,44], which is applied to the analyses of EL measurements given in this thesis.

Electroluminescence results from the radiative recombination of the injected charge carriers by applying a forward voltage bias to a solar device, which is the reciprocal process of the standard operation of a solar cell. For a solar cell, the external quantum efficiency $Q_{\mathrm{e}}(E)$ is an important quantity. The relationship between the external quantum efficiency and electroluminescence emission ϕ_{el} is given by the reciprocity theorem [43], which is written as

$$\phi_{\mathrm{el}}(E) = Q_{\mathrm{e}}(E)\phi_{\mathrm{bb}}(E)\left[\exp\left(\frac{qV_{\mathrm{j}}}{kT}\right) - 1\right]. \tag{2.25}$$

The external quantum efficiency $Q_{\mathrm{e}}(E)$ is defined as the ratio of the number of carriers collected by the solar cell to the number of photons of a specific wavelength impinging on the surface of the device

$$Q_{\mathrm{e}}(E) = \frac{1}{q}\frac{dJ_{\mathrm{sc}}}{d\phi_{\mathrm{in}}(E)}, \tag{2.26}$$

where $d\phi_{\mathrm{in}}(E)$ is the incident photon flux in the energy interval dE, which leads to dJ_{sc}. The external quantum efficiency $Q_{\mathrm{e}}(E)$ can also be expressed as the integral of the product of the generation rate $g(x, E)$ and the collection probability $F(x)$

$$Q_{\mathrm{e}}(E) = \int_0^d g(x, E)F(x)dx. \tag{2.27}$$

The reciprocity theorem [43, 44] is used for both spectrally and spatially resolved EL analysis. For the analysis of spectrally resolved EL measurements, the EL emission $\phi_{\mathrm{el}}(E)$ can directly be calculated from the measured $Q_{\mathrm{e}}(E)$ and vice versa according to the relationship between $\phi_{\mathrm{el}}(E)$ and $Q_{\mathrm{e}}(E)$, if the EL spectrum is independent of the applied voltage, or in other words, $\phi_{\mathrm{el}}(E)$ is directly proportional to $Q_{\mathrm{e}}(E)$

$$\phi_{\mathrm{el}}(E) \propto Q_{\mathrm{e}}(E). \tag{2.28}$$

The spatially resolved EL analysis makes use of the relation between the local EL emission $\phi_{\mathrm{el}}(E, \mathbf{r})$ and the local junction voltage $V_{\mathrm{j}}(\mathbf{r})$ to determine the absolute

value for the local junction voltage. Here, $\mathbf{r} = (x, y)$ is the local position of the solar cell's surface. For the analysis of EL images, Eq. (2.25) is rewritten as

$$\phi_{\mathrm{el}}(E, \mathbf{r}) = Q_{\mathrm{e}}(E, \mathbf{r})\phi_{\mathrm{bb}}(E)\left[\exp\left(\frac{qV_{\mathrm{j}}(\mathbf{r})}{kT}\right) - 1\right]. \tag{2.29}$$

In most cases, the interpretation of spatially resolved EL measurements uses the camera signal of each pixel $S_{\mathrm{cam}}(\mathbf{r})$, which is the product of the proportionality $S_0(\mathbf{r})$ and the local junction voltage $V_{\mathrm{j}}(\mathbf{r})$ [32, 33], that is

$$S_{\mathrm{cam}}(\mathbf{r}) = S_0(\mathbf{r}) \exp\left(\frac{qV_{\mathrm{j}}(\mathbf{r})}{kT}\right), \tag{2.30}$$

where $qV_{\mathrm{j}} \gg kT$ and $S_0(\mathbf{r})$ is given by

$$S_0(\mathbf{r}) = \int Q_{\mathrm{cam}}(E) Q_{\mathrm{e}}(E, \mathbf{r}) \phi_{\mathrm{bb}}(E) dE \tag{2.31}$$

because of the spectrally dependent quantum efficiency $Q_{\mathrm{cam}}(E)$ of the camera. Note that here, the spatial influence of the external quantum efficiency $Q_{\mathrm{e}}(E, \mathbf{r})$ on the EL intensity is neglected since the spatial impact of the local junction voltage on the EL intensity is much stronger due to the exponential relation between $V_{\mathrm{j}}(\mathbf{r})$ and $\phi_{\mathrm{el}}(E, \mathbf{r})$.

The determination of the absolute junction voltage [38] of each individual cell V_{j} and of the entire module V_{m} from EL images is described as follows.

From Eq. (2.30), the absolute local junction voltage $V_{\mathrm{j}}(\mathbf{r})$ can be calculated by

$$V_{\mathrm{j}}(\mathbf{r}) = \frac{kT}{q} \ln\left(S_{\mathrm{cam}}(\mathbf{r})\right) + V_{\mathrm{off}} = V_{\mathrm{j}}'(\mathbf{r}) + V_{\mathrm{off}}, \tag{2.32}$$

where $V_{\mathrm{j}}'(\mathbf{r})$ is the relative local junction voltage and V_{off} is the offset voltage, which is defined by

$$V_{\mathrm{off}} = \frac{kT}{q} \ln\left(S_0(\mathbf{r})\right). \tag{2.33}$$

From the superposition principle, the offset voltage V_{off} can be determined by comparing the sum of the relative junction voltage of each individual cell V_{j}' from the EL measurements carried out at different injected current densities J to the open circuit voltage V_{oc} of the same sample measured for a short circuit current density $J_{\mathrm{sc}} = J$ equaling the injected current density during the EL experiment [57]. This comparison gives

$$V_{\mathrm{oc}}|_{J_{\mathrm{sc}}=J} = \sum_{k=1}^{N} V_{\mathrm{j,k}}'|_{J=J_{\mathrm{sc}}} + NV_{\mathrm{off}} = \sum_{k=1}^{N} V_{\mathrm{j,k}}|_{J=J_{\mathrm{sc}}}, \tag{2.34}$$

where N is the number of cells in the module.

The average relative voltage for each cell in the module V_{j}' is calculated in two steps. In the first step, a line-scan of the relative junction voltage V_{j}' is obtained by averaging the relative local junction voltage $V_{\mathrm{j}}'(\mathbf{r})$ over the entire length of the module. In the second step, $\overline{V_{\mathrm{j}}'(\mathbf{r})}$ is obtained by averaging the relative junction voltage from the line-scan over the entire width of each cell.

The absolute junction voltage of each individual cell V_{j} is finally determined by

$$V_{\mathrm{j}} = \overline{V_{\mathrm{j}}'(\mathbf{r})} + V_{\mathrm{off}}. \tag{2.35}$$

Furthermore, another reciprocity relation is derived based on the reciprocal relation between the standard solar operation and EL, i.e. the relation between the EL efficiency of the light-emitting diodes Q_{LED} and the open-circuit voltage of the device [58]. With the help of this relation, the EL efficiency Q_{LED} can be predicted from the open-circuit voltage or vice versa.

The maximal open-circuit voltage of a solar device is the open-circuit voltage of an ideal solar cell according to Shockley and Queisser. Shockley and Queisser assumed that in an ideal solar cell, the generated carriers can be perfectly collected, radiative recombination is the only recombination process, the absorptance follows a step-like function ($a(E \geq E_{\mathrm{g}}) = 1$, $a(E < E_{\mathrm{g}}) = 0$), and that the diode ideality factor n_{id} equals one [9]. In a real solar device, the absorptance $a(E)$ equals $Q_{\mathrm{e}}(E) < 1$ and both radiative and non-radiative recombination exist. In order to calculate the losses of the open-circuit voltage in a real device due to non-radiative recombination, it is important to know the open-circuit voltage with only presence of radiative recombination, i.e. $V_{\mathrm{oc,r}}$, which is given by

$$V_{\mathrm{oc,r}} = \frac{kT}{q} \ln\left(\frac{J_{\mathrm{sc,r}}}{J_{\mathrm{0,r}}} + 1\right). \tag{2.36}$$

Here, $J_{\mathrm{sc,r}}$ is the radiative short-circuit current density

$$J_{\mathrm{sc,r}} = q \int_0^\infty \phi_{\mathrm{in}}(E) Q_{\mathrm{e}}(E) dE, \tag{2.37}$$

and the radiative saturation current density is given by

$$J_{\mathrm{0,r}} = q \int_0^\infty \phi_{\mathrm{bb}}(E) Q_{\mathrm{e}}(E) dE. \tag{2.38}$$

Moreover, the electroluminescencent efficiency Q_{LED} is defined as

$$Q_{\mathrm{LED}} = \frac{J_{\mathrm{r}}(V)}{J_{\mathrm{r}}(V) + J_{\mathrm{nr}}(V)} = \frac{J_{0,\mathrm{r}} \exp\left(qV/kT\right)}{J_{\mathrm{r}}(V) + J_{\mathrm{nr}}(V)}. \tag{2.39}$$

If the device is operated under open-circuit voltage, the sum $J_{\mathrm{r}}(V) + J_{\mathrm{nr}}(V)$ equals J_{sc}. The LED quantum efficiency Q_{LED} of the device is then given by

$$Q_{\mathrm{LED}}(V_{\mathrm{oc}}) = \frac{J_{0,\mathrm{r}} \exp\left(qV_{\mathrm{oc}}/kT\right)}{J_{\mathrm{sc}}}. \tag{2.40}$$

From Eqs. (2.36) and (2.40), the loss in V_{oc} due to non-radiative recombination is calculated by

$$\Delta V_{\mathrm{oc}} = V_{\mathrm{oc,r}} - V_{\mathrm{oc}} = -\frac{kT}{q}\left[\ln\left(Q_{\mathrm{LED}}(V_{\mathrm{oc}})\right)\right]. \tag{2.41}$$

Equation (2.41) [58] describes the relation between Q_{LED} and the real open-circuit voltage V_{oc}, which enables the prediction of the LED quantum efficiency Q_{LED} and the determination of the losses in the open-circuit voltage due to non-radiative recombination.

The reciprocity theorem shown in Eq. (2.25) is based on Donolato's theorem [59] and Würfel's generalized Planck's law [48]. Thus, the reciprocity theorem holds only when both Donolato's theorem and Würfel's generalized Planck's law hold. The validity of Donolato's theorem requires the validity of the superposition principle.

The superposition principle holds if the J/V_{il} characteristic under illumination is the dark J/V characteristic shifted by a constant factor, i.e. the photogenerated current density J_{ph}, which equals the short-circuit current density J_{sc} under illumination. In other words, the photogenerated current density should be independent of voltage so that the superposition principle holds. The photogenerated current density depends on the generation rate $g(x, E)$ and the collection of carriers $f_{\mathrm{c}}(x)$, which is defined as

$$J_{\mathrm{ph}} = q\int_0^{\infty} \phi_{\mathrm{in}}(E) Q_{\mathrm{e}}(E) dE = \int_0^{\infty}\int_0^{d} g(x, E)\phi_{\mathrm{in}}(E) f_{\mathrm{c}}(x) dx dE. \tag{2.42}$$

The generation rate $g(x, E)$ is independent of the voltage and photon flux. Therefore, the voltage dependence of J_{ph} results from the voltage dependence of the charge carrier collection, which leads to the violation of the superposition principle, and thus of Donolato's theorem.

Disordered, low mobility p-i-n thin-film solar cells such as amorphous and microcrystalline, show voltage-dependent carrier collection. Thus, the photocurrent is also voltage-dependent and consequently, the superposition principle does not hold for *a*-Si:H and μc-Si:H devices. Violation of the superposition via violation of Donolato's theorem is not compatible with the reciprocity relation because the photovoltaic quantum efficiency $Q_e(E)$ becomes voltage bias dependent.

EL analyses based on the reciprocity theorem have been done for CIGS thin-film solar cells [38,58,60], crystalline silicon solar cells [60,61], organic solar cells [41], and GaInP/InGaAs/Ge multijunction solar cells [57,62]. In the case of *a*-Si:H thin-film devices, applying the reciprocity theorem for analysis of the EL signal is not as straight-forward as for the above-mentioned solar technologies because of the violation of the superposition principle, and because the radiative ideality factor is larger than unity. The detailed analysis of EL images of *a*-Si:H thin-film solar cells and modules by using a modification of Eq. (2.29) is introduced in chapter 7.

The reciprocity theorem described in Eq. (2.25) has also been further extended to the case of photoluminescent emission $\phi_{pl}(\phi_{exc}, E)$ resulting from the photoexcitation ϕ_{exc} by Rau [44]. This generalized reciprocal relation [44] is given by

$$\phi_{em}(E) = \phi_{sc}(E, \phi_{exc}) + \phi_{el}(E, V_j) = \phi_{sc}(E, \phi_{exc}) + Q_e(E)\phi_{bb}(E)\left[\exp\left(\frac{qV_j}{kT}\right) - 1\right]. \tag{2.43}$$

Equation (2.43) shows that the emission $\phi_{em}(E)$, as a function of photon energy E, is a superposition of the EL emission ϕ_{el} stimulated by the junction voltage V_j and the short circuit (sc) emission ϕ_{sc} resulting from the photoexcitation ϕ_{exc}.

2.3. Thin-film solar cells

For standard crystalline silicon (c-Si) solar cells, the absorber thicknesses are several hundreds μm, whereas the absorber thicknesses of thin-film solar cells are only several μm or even several hundred nm. This thesis focuses on the application of the EL characterization technique to Cu(In,Ga)Se_2 (CIGS) and hydrogenated amorphous silicon (*a*-Si:H) thin-film solar cells or modules. Therefore, in this section the device structures of CIGS and *a*-Si:H are introduced.

2.3.1. Cu(In,Ga)Se_2 solar cells

Solar cells and modules based on the chalcopyrite compound Cu(In,Ga)Se_2 achieve the highest efficiency among all thin-film solar cell technologies [15]. A typical device structure of a CIGS solar cell with a substrate configuration is shown in Fig. 2.5(a).

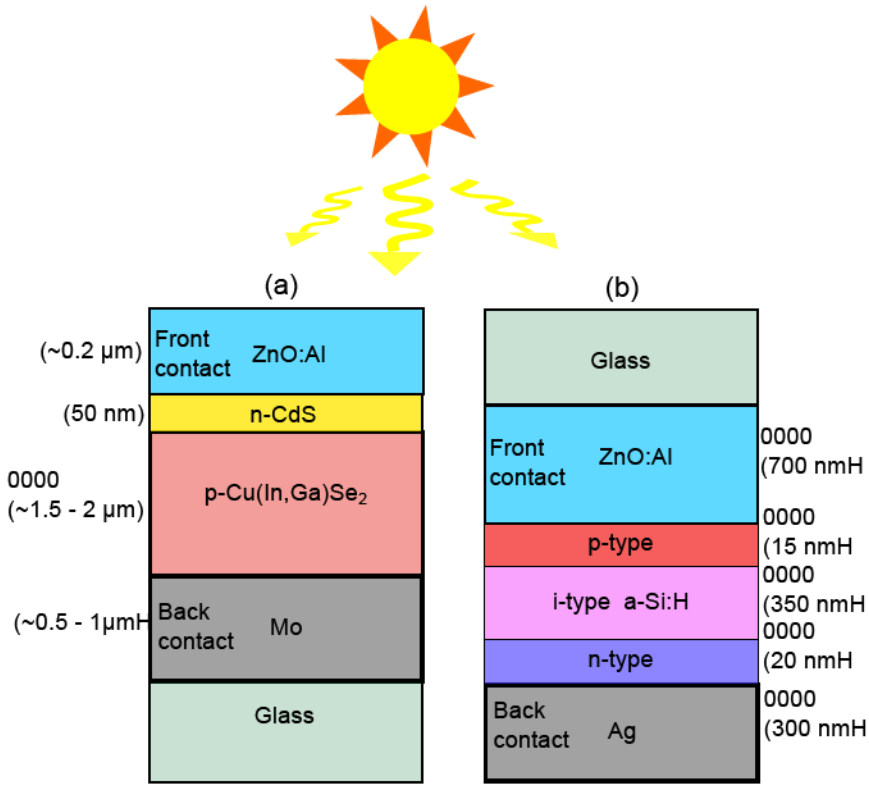

Figure 2.5.: (a) Typical device structure of a CIGS thin-film solar cell with a substrate configuration. (b) Typical p-i-n device structure of an *a*-Si:H thin-film solar cell with a superstrate configuration.

The device starts with a glass substrate. A commonly used substrate for CIGS solar cells is Na-containing glass. The reason for using this kind of glass is

to improve the electronic properties of the device, since the diffusion of Na into the absorber improves the growth of the absorber [63–67]. For the back contact, a thin molybdenum (Mo) layer with a thickness of approximately 0.5-1 µm is sputtered on the glass substrate because Mo provides a good ohmic contact for the majority carriers and a low recombination rate for minority carriers [68–73]. Furthermore, Mo also plays an important role for adhesion of the absorber film, and supports the transport of Na from the glass substrate into the CIGS absorber.

The absorber material is the quaternary $Cu(In,Ga)Se_2$ direct semiconductor, which is deposited on top of the Mo layer usually by the vacuum co-evaporation [74,75]. Subsequently, a thin cadmium sulfide (CdS) n-type semiconductor of around 50 nm is deposited onto the CIGS absorber. CdS is commonly prepared by a chemical bath deposition (CDB) [76], and serves as a buffer layer because many of its physical properties, e.g. band gap and refractive index, are between those of the ZnO window layer and CIGS absorber layer [50]. The CdS deposition provides a complete covering of the rough CIGS absorber surface [77], and a good passivation of the CIGS/CdS interface [50]. The standard sequence of the window layer consists of 50 nm of intrinsic zinc oxide (i-ZnO) and 150 nm of aluminium doped (ZnO:Al), which serve as the transparent conductive oxide (TCO) front electrode in this device. The role of the i-ZnO layer in the CIGS device is discussed in Ref. [78], in which the authors discussed that the local series resistance provided by the i-ZnO mitigates the effects of the electrical inhomogeneities, which limit the open-circuit voltage of the device.

In this thesis, the investigated samples are large-area (30×30 cm^2) CIGS modules from Manz AG, formerly Würth Solar GmbH&Co. KG. The large-area CIGS modules consist of 64 individual cells with a cell length of 30 cm and a cell width of 0.4 cm. CIGS modules are fabricated in an inline process consisting of the co-evaporation of a CIGS absorber on a Mo-covered glass substrate (3 mm) [18,20,79]. During the fabrication process, the monolithic interconnection is achieved using three scribing steps (see Fig. 2.6). In the first step, the electrical separation of the Mo back contact of the individual cells is done by a laser scribing (P1) process. In the second step, the series connection of the cells in the modules is realized by a mechanical scribe down to the Mo layer (P2). Subsequently, the transparent ZnO window layer is deposited. To complete the monolithic integration of the module,

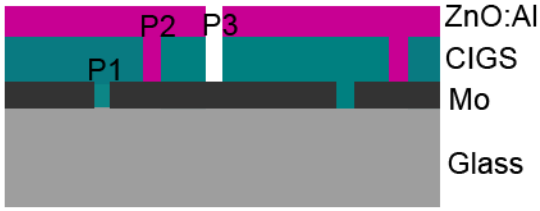

Figure 2.6.: Series connections of CIGS solar cells with different scribing steps P1 (laser scribe), P2 and P3 (mechanical scribes), which are done successively.

a third scribing step (P3) is carried out with a mechanical scribe to separate the cells [79]. For the spectrally resolved measurements presented in chapter 4, a cell fragment of (4×9 mm^2) is cut from a large-area (30×30 cm^2) module. For the analysis of different defect types in CIGS devices shown in chapter 6, module and cell fragments of different sizes are also cut from large-area modules.

2.3.2. *a*-Si:H solar cells

The most commonly used *a*-Si:H device structure has a so called superstrate configuration, which is shown in Fig. 2.5(b). Glass is usually used as a superstrate, which enables light to come through the front TCO contact to the absorber layer, and also mechanically supports the device. Due to their transparency and high conductivity, materials such as ZnO or SnO_2 are chosen for the TCO front contact. To enhance the optical path length of incoming light, the front contact and the back contact are textured (not shown in Fig. 2.5(b)). For the preparation of *a*-Si:H films, either plasma enhanced chemical vapor deposition (PECVD) [80, 81] or hot wire chemical vapor deposition (HWCVD) [82–84] is usually used. The p-type (≈ 15 nm), intrinsic i-type (≈ 350 nm), and n-type (≈ 20 nm) *a*-Si:H are sequentially deposited in a single chamber or in a multi-chamber system. Finally, the *a*-Si:H device is completed with a silver back contact.

For this work, single *a*-Si:H devices are used, which are fabricated at the Institute of Energy- and Climate Research (IEK-5 photovoltaics) in a superstrate configuration with Glass/TCO/*a*-Si:H p-i-n/ZnO/Ag layer stack. The glass used

for the samples is from the company Corning, where the in-house ZnO as the TCO is deposited onto it, and from the company Asahi, glass type VU, which already includes SnO as the TCO. The p-, i-, and n-layers are subsequently deposited by PECVD. Detailed information about the different preparation steps can be found elsewhere [80, 81]. The substrate area of the investigated *a*-Si:H modules is (10×10 cm^2), the active module area is (8×8 cm^2). The module consists of eight series connected cell stripes with a length of 8 cm and a width of 1 cm.

2.4. Electrical characterization of solar cells

2.4.1. Current/Voltage characteristics

For an ideal solar cell, the dark current density J_d under an applied voltage V follows the Shockley diode equation

$$J_\mathrm{d} = J_0 \left[\exp\left(\frac{qV}{kT}\right) - 1 \right], \tag{2.44}$$

where J_0 is the saturation current density and kT the thermal voltage. The total current density J results from the sum of J_d and the photon-generated current density J_ph under illumination, which equals the short circuit current density J_sc

$$J = J_0 \left[\exp\left(\frac{qV}{kT}\right) - 1 \right] - J_\mathrm{sc}. \tag{2.45}$$

The short circuit current density J_sc is obtained from Eq. (2.45) if the applied voltage V equals zero. The open circuit voltage is defined as the voltage drop over a sample under illumination when the total current J is zero. It follows from Eq. (2.45)

$$V_\mathrm{oc} = \frac{kT}{q} \ln\left(\frac{J_\mathrm{sc}}{J_0} + 1\right). \tag{2.46}$$

Illuminated J/V characteristics are measured by a sun simulator, under standard testing conditions (STC), i.e. a sample temperature of 25°C and AM1.5G spectrum. Figure 2.7 shows an illuminated characteristic of a solar cell measured at STC. J/V measurements are used to derive the output parameters of a solar cell, i.e. J_sc, V_oc, the voltage at the maximum power point (mpp) (V_mpp), the current

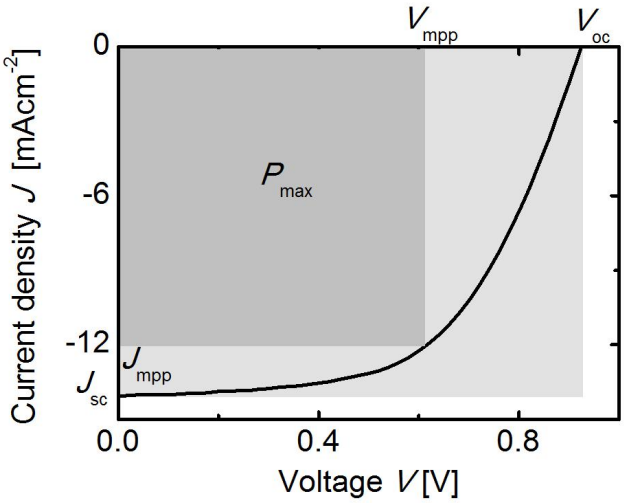

Figure 2.7.: J/V characteristic of a solar cell under illumination. The maximal power density P_{max} is the product of the current density and the voltage at maximal power point (mpp) J_{mpp}, V_{mpp}. The fillfactor FF is defined as the ratio of P_{max} (small rectangle) to the product $J_{\mathrm{sc}}V_{\mathrm{oc}}$ (large rectangle).

density at the maximum power point (J_{mpp}). The maximal power density (P_{max}), the fillfactor FF and the efficiency η are determined by the following equations

$$P_{\mathrm{max}} = V_{\mathrm{mpp}} J_{\mathrm{mpp}}, \tag{2.47}$$

$$FF = \frac{P_{\mathrm{max}}}{V_{\mathrm{oc}} J_{\mathrm{sc}}}, \tag{2.48}$$

$$\eta = \frac{P_{\mathrm{max}}}{P_{\mathrm{in}}}. \tag{2.49}$$

Here P_{in} is the optical power density of the incoming light.

Figure 2.8 shows an equivalent network of a real solar cell including series resistance R_{s} and shunt resistance R_{sh}, which significantly affect the FF and the output power of the device. Loss mechanisms in real solar cells due to various recombination processes within the junction, e.g. SRH recombination, which causes an diode ideality factor n_{id} larger than one, i.e. $1 \leqslant n_{\mathrm{id}} \leqslant 2$. Therefore, the dark

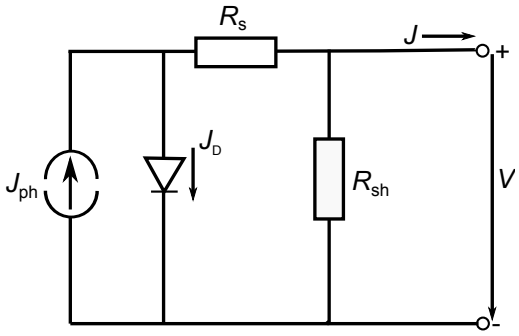

Figure 2.8.: Equivalent network of a real solar cell including series resistance R_s and shunt resistance R_{sh}

current density under a forward applied voltage is written as

$$J_d = J_0 \left[\exp\left(\frac{q(V - J_d R_s)}{n_{id} kT} \right) - 1 \right] + \frac{V - J_d R_s}{R_{sh}}. \tag{2.50}$$

The dark characteristic of a CIGS solar cell gives the information about the influences of the series resistance and shunt resistance on the device. Figure 2.9 indicates the dark J/V characteristics of a solar cell, which has three typical regions, namely, the low voltage region (I) ($V < 0.6$ V), middle voltage region (II) ($V = 0.6 - 1$ V), and the high voltage region (III) ($V > 1$ V). Note that the lower and upper limits presented here are only typical for the CIGS samples, which are investigated in this work. The deviation of the J/V curve in the low voltage range from the diode equation $J = J_0 \exp(qV/n_{id}kT)$ as shown in the middle voltage region, is caused by the influence of a shunt. The saturation of the curve in the high voltage range above 1 V results from the series resistance.

2.4.2. External quantum efficiency

The external quantum efficiency $Q_e(E)$ measurements are carried out by using a monochromator based setup [85]. A white light from a W-halogen or a Xe-arc lamp is chopped with a chopper to obtain a periodic signal, which can be used by a lock-in amplifier. The monochromatic light is then guided to a reference cell, e.g.

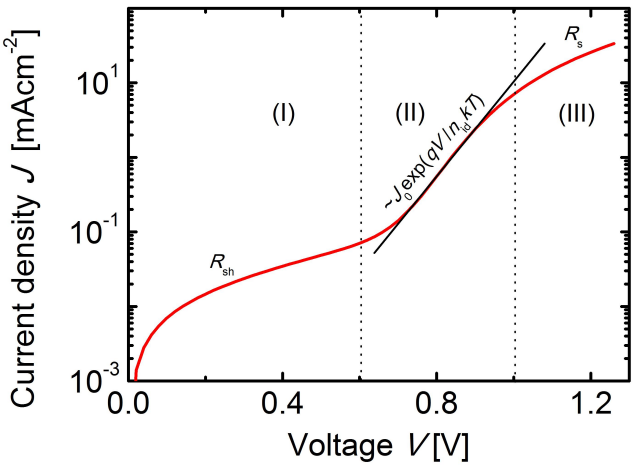

Figure 2.9.: Dark J/V characteristic of a solar cell with three typical regions: (I) low voltage region with the influence of the shunt resistance R_{sh}, (II) middle voltage region (ideal diode), (III) high voltage region with the influence of the series resistance R_{s}.

a photodiode for the absolute calibration. Another solar cell is used during the calibration and the measurement to monitor the variations in the absolute intensity of the light source. For each wavelength, the resulting $Q_{\mathrm{e}}(E)$ value is corrected by the ratio of the intensity on the monitor cell during the calibration and the measurement.

Figure 2.10 shows a typical plot of the external quantum efficiency $Q_{\mathrm{e}}(E)$ vs wavelength λ of a CIGS and an a-Si:H solar cell, in which the external quantum efficiency reaches its maximum at 630 nm and 530 nm, respectively. The external quantum efficiency $Q_{\mathrm{e}}(E)$ measurements enable the analysis of both optical and recombination losses. The optical losses consist of reflection losses and parasitic absorption, i.e. absorption in parts of the structure, which does not contribute to the photocurrent. The internal quantum efficiency Q_{i} is the efficiency resulting from the correction of the external quantum efficiency for the spectral reflectance $R(E)$.

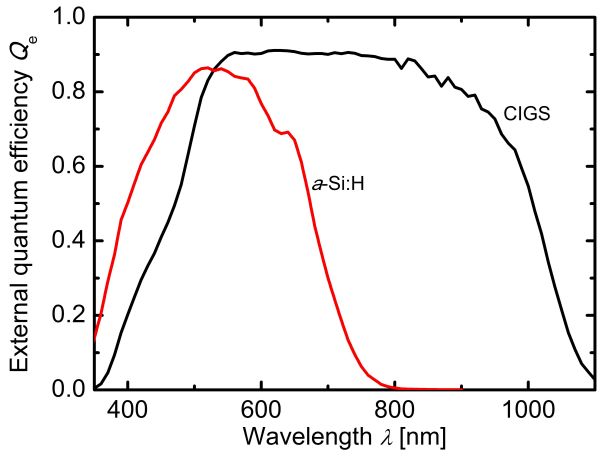

Figure 2.10.: Typical external quantum efficiencies of an *a*-Si:H and a CIGS solar cell.

Note that the internal quantum efficiency includes parasitic absorption losses.

$$Q_{\mathrm{i}}(E) = \frac{Q_{\mathrm{e}}(E)}{1 - R(E)}. \tag{2.51}$$

The recombination losses in CIGS devices occur in the different parts of the devices. An overview of the recombination losses in CIGS thin-film solar cells is given in Ref. [50]. In the short wavelength range, the losses result from the recombination in the ZnO and CdS layers. Furthermore, recombination at the interfaces, in the CIGS absorber layer and the free carrier absorption in the ZnO layer also contribute to the total losses of the CIGS devices.

3. Experimental methods and setups

In this chapter, various measurement techniques applied in this work are briefly described. Since this work mainly focuses on the analysis of spatially resolved EL measurements, the setup for EL imaging is described in detail. Furthermore, the effect of stray light on the quantitative analysis of EL images is also discussed. Additionally, some of the results presented in this thesis stem from EL, PL spectroscopy and LIT measurements. Therefore, their setups are briefly introduced as well.

3.1. Electroluminescence imaging

Electroluminescence imaging is a powerful characterization tool for photovoltaic devices, which can provide spatially resolved information of the investigated sample with high resolution and with a measurement time in the order of seconds. For EL measurements, a sample is connected to a power supply, and thereby, charge carriers are injected into the sample. The injected charge carriers recombine within the sample radiatively and cause photon emission, which is then detected by a camera, e.g., a Si-CCD or an InGaAs camera.

A simple setup for spatially resolved EL measurements is shown in Fig. 3.1. The setup includes a light-tight box, a Si-CCD camera, an optical lens, a power source, a computer, and the sample to be investigated. Ambient light is undesirable since it can distort the EL signal from the camera, therefore, a shielding is indispensable to exclude ambient light. Our setup allows the measurements of samples sized up to (40×40 cm^2). The power source is a Keithley High Voltage Source Meter Model 2420 [86], which is designed to source and measure voltages of ± 60 V and currents of ± 3 A. The maximum allowed power of the power source is 60 W. The

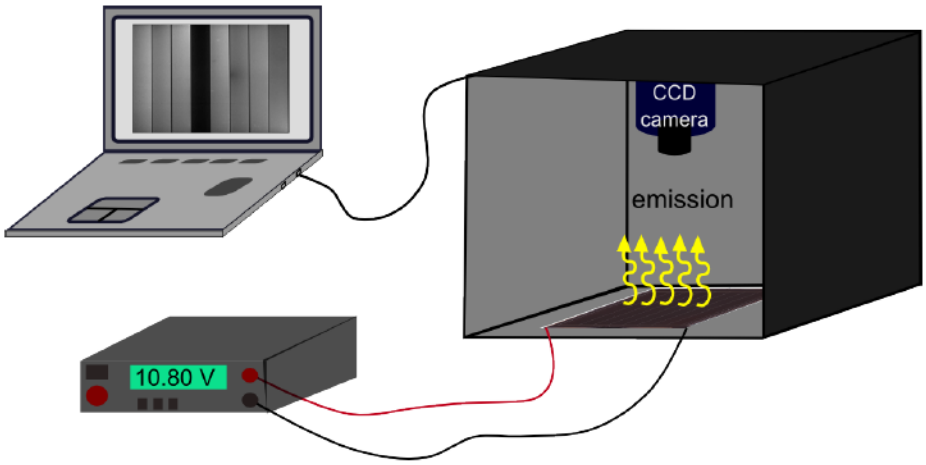

Figure 3.1.: Setup for the spatially resolved EL measurements.

samples to be measured in this thesis are CIGS and *a*-Si:H thin-film solar cells and modules as described in sections 2.3.1 and 2.3.2.

The EL images presented in this work are recorded by both cooled Si-CCD and Indium Gallium Arsenide (InGaAs) cameras. The front-illuminated Si-CCD camera from Apogee Imaging Systems (AIS) [87] has a large format (36×36 mm^2) full-frame sensor, which corresponds to an image resolution of (3056×3056 pixels) with a pixel size of (12×12 µm^2). The camera is cooled down to -20°C by a thermoelectric peltier cooler with forced air cooling. For most EL images recorded by the Si-CCD camera shown in this thesis, a (3×3) binning is used, which increases the sensitivity of the "super pixels" by a factor of nine, and shortens the required exposure time.

A low-noise InGaAs camera from Princeton Instruments systems [88] with a resolution of (640×512 pixels) is also used for both EL and PL imaging measurements. The InGaAs camera uses a thermoelectric peltier cooler for cooling down to -90°C to reduce dark current.

Figure 3.2 shows the EL spectra of different solar cell technologies, namely, *a*-Si:H, c-Si, and CIGS and the external quantum efficiencies Q_{cam}(Si) and Q_{cam}(InGaAs) of the Si-CCD and InGaAs cameras used in this work. All the spectra shown here are normalized to their respective maximum. The external quantum efficiency

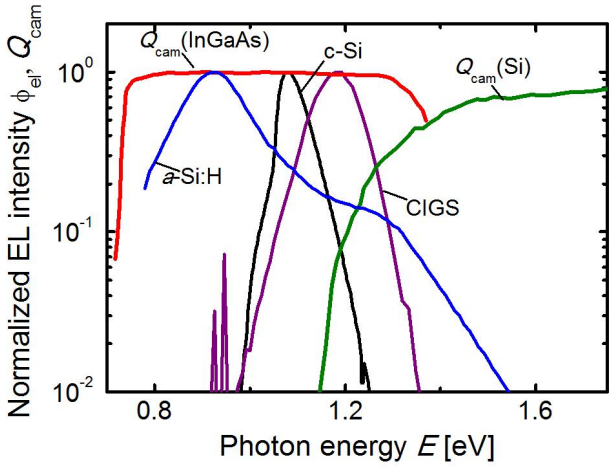

Figure 3.2.: Plot of the external quantum efficiencies $Q_{\mathrm{cam}}(\mathrm{Si})$ and $Q_{\mathrm{cam}}(\mathrm{InGaAs})$ of the Si- and InGaAs-CCD cameras, respectively, and the normalized EL spectra of a crystalline silicon solar cell, an *a*-Si:H, and a CIGS solar cell.

$Q_{\mathrm{cam}}(\mathrm{InGaAs})$ indicates that the low noise InGaAs camera enables the detection of light emitted in a wide spectral range ($800 \leq \lambda \leq 1700$ nm), corresponding to photon energies of $0.73 \leq E \leq 1.5$ eV. Therefore, the InGaAs camera is suitable for EL measurements of all three photovoltaic devices exhibited in Fig. 3.2. For the Si-CCD camera, the external quantum efficiency $Q_{\mathrm{cam}}(\mathrm{Si})$ is much lower than that of the InGaAs camera in the near infrared (NIR) range. The Si-CCD camera is sensitive in a spectral range of $350 \leq \lambda \leq 1100$ nm, corresponding to photon energies of $1.11 \leq E \leq 3.5$ eV. The EL signals from *a*-Si:H, c-Si, and CIGS are also detectable with a Si-CCD camera. Si-CCD cameras are more commonly used because they are about a factor of ten cheaper than the InGaAs cameras, and show much less noise and dark current, allowing for much longer exposure times.

Besides the camera, the lens plays a very important role for the precise fidelity of an image. Because of the large imaging area of our Si-CCD camera (3056 × 3056 pixels), the APO-RODAGON 4.5/75 mm lens with an F-number of 4.5 and

focal length of 75 mm from Stemmer Imaging GmbH, was chosen to minimize the optical aberrations.

Effects of stray light and noise on the quantitative analysis of EL images

In this thesis, spatially resolved EL measurements are carried out by applying either a constant current or a constant voltage to the sample. Additionally, a background image is recorded with the same camera settings, but the power source is switched off. The final EL image results from the image taken under bias subtracting from the background image to eliminate the dark signal of the CCD camera and the ambient light. However, the final EL image still shows non-zero intensity values at the non-active areas. This non-zero values may stem from stray light or/and noise (i.e. read-out noise, thermally generated noise).

To check for the influence of noise on the analysis of EL images, one hundred EL images are recorded at the same injection current density and with the same camera settings. The average junction voltage obtained from these EL images does not show a significant deviation compared to the junction voltage from one EL image. Therefore, noise only plays a minor role in the analysis of EL image.

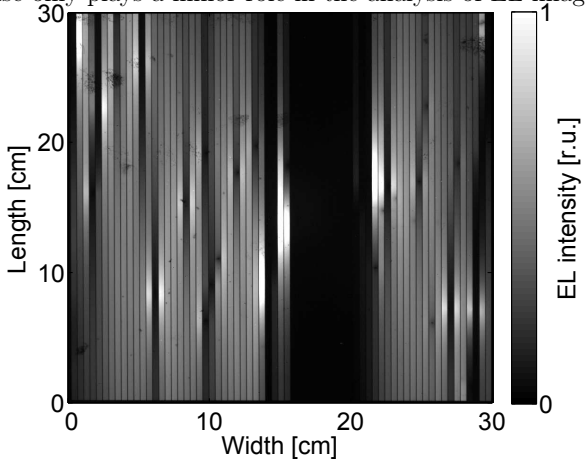

Figure 3.3.: EL image of a heavily shunted CIGS module measured by a Si-CCD camera at a constant injection current density $J = 8.3$ mAcm^{-2}.

In contrast, stray light can affect the quantitative analysis method of EL images introduced in this thesis. The stray light may stem from scattering in the lens, scattering within the sample, light spreading in the CCD [89]. If the signal from stray light is higher compared to the desirable EL signal ϕ_{el}, e.g., from defective areas, stray light will have a significant impact on the evaluation of the weak EL signal. Therefore, in order to investigate the effect of stray light in more detail, a heavily shunted module was chosen for the EL measurements.

Figure 3.3 shows an EL image of a heavily shunted CIGS (30×30 cm^2) thin-film module, which is measured at a constant current density of $J = 0.8$ mAcm^{-2}. At this low injection current density, the EL signal of the shunted cells is very low, therefore, the shunted cells appear as dark regions in the image.

Fig. 3.4(a) shows three line-scans of the EL intensity across the EL image in Fig. 3.3. These line-scans are obtained from averaging over the entire length of the respective EL images measured at different current densities of $J = [0.8, 8.3, 25.0]$ mAcm^{-2}. From the EL intensities measured at three injection current densities of $J = [0.8, 8.3, 25.0]$ mAcm^{-2}, the relative local junction voltage $V_{\mathrm{j}}'(\mathbf{r})$ is calculated according to Eq. (2.29), i.e. $V_{\mathrm{j}}'(\mathbf{r}) \propto \ln\left(\phi_{\mathrm{el}}(\mathbf{r})\right)$. Note that the local junction voltage is relative because a constant offset voltage V_{off} (see Eqs. (2.32) and (2.33)) was not considered here. The line-scans of the relative junction voltage shown in Fig. 3.4(b) are obtained by averaging $V_{\mathrm{j}}'(\mathbf{r})$ over the entire length of the module.

Both the line-scans of the EL intensity and the relative junction voltage shown in Fig. 3.4 indicate that the values of the EL intensity and, thus, the relative junction voltage at the edge of the module (marked rectangles), where no active cell area exists, differ from zero. Moreover, these values are proportional to the EL intensity of the module, which indicates that stray light, which causes this phenomenon stems from the sample itself. Note that a background image has already been subtracted to eliminate ambient light. Furthermore, Fig. 3.4 also shows that the EL intensity and the relative junction voltage of the heavily shunted cells are limited by stray light. This is because the EL intensities and the relative junction voltages of the shunted cells measured at all three injection current densities shown in Fig. 3.4 are at the same level as that caused by stray light. Therefore, the EL signal, as well as the relative junction voltage of the shunted cells are not properly detected with the presence of stray light. In order to reduce the effect of stray light, a correction for

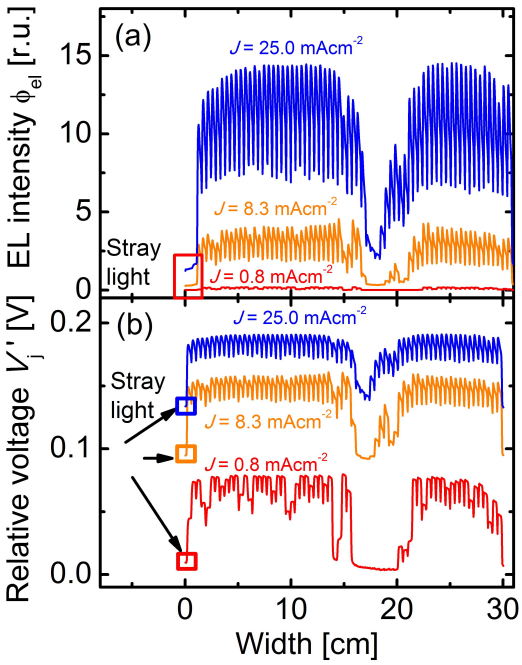

Figure 3.4.: Line-scans of the EL intensity (a) and of the relative junction voltage (b) of a CIGS thin-film solar module obtained from the EL images measured at different injection current densities of $J = [0.8,\ 8.3,\ 25.0]$ mAcm^{-2}, which show stray light effect.

stray light has been done by setting zero to the intensity next to the solar cell. Note that for this correction, local variations in the intensity of stray light are assumed to be constant throughout the sample. The result of this correction is presented in detail below.

The quantitative analysis method of EL images applied in this work enables the determination of the absolute local junction voltage $V_\mathrm{j}(\mathbf{r})$ at each position of the module and the absolute junction voltage V_j of each individual cell from EL

intensity. The absolute local junction voltage V_j is the sum of the relative junction voltage of each individual cell V_j' and the offset voltage V_{off} (see Eq. (2.35)). Here, the relative junction voltages V_j' are calculated from the line-scans shown in Fig. 3.4(b) by averaging the line-scans over the entire width of each individual cell as described in Sec. 2.2.

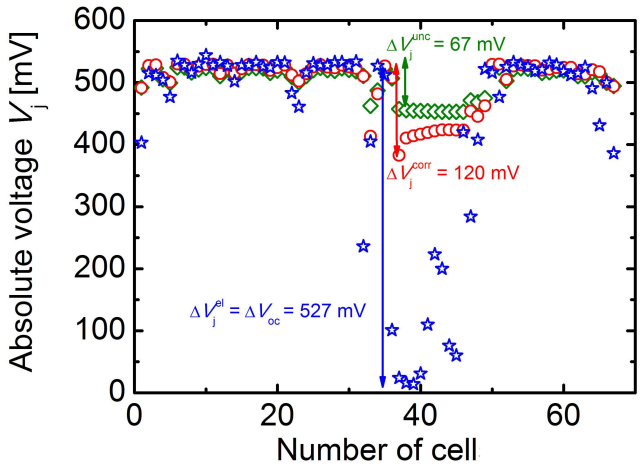

Figure 3.5.: Absolute junction voltage of each individual cell of a CIGS thin-film solar module obtained from EL images with open diamonds (uncorrected for the stray light), open circles (corrected for the stray light). The open stars are the measured open-circuit voltages [90].

The absolute junction voltages of each individual cell of the module shown in Fig. 3.3 are depicted in Fig. 3.5. The open diamonds are the voltages of different cells obtained from the voltage line-scan shown in Fig. 3.4(b) at $J = 0.8$ mAcm^{-2}. These voltages are not corrected for stray light. The voltage difference ΔV_j^{unc} between the shunted and the non-shunted cell is ≈ 67 mV for the case that stray-light is not corrected. The open circles are the voltages, which are corrected for stray light by subtracting the voltage line-scan measured at $J = 0.8$ mAcm^{-2} (see Fig. 3.4(b)) to its stray light level (red marked rectangle). From this correction, a factor close to

two is obtained for the junction voltage difference $\Delta V_{\mathrm{j}}^{\mathrm{corr}} = 120$ mV between the shunted and non-shunted cell. The open-star curve is the measured open-circuit voltage V_{oc} of each individual cell, which are carried out by using a mask to cover all the cells in the modules, which are not measured, and illuminating the cell to be measured [90]. The measured open-circuit voltage should equal the junction voltage V_{j} obtained from EL images. As shown in Fig. 3.5, the open-circuit voltage difference ΔV_{oc} between the shunted and non-shunted cell is around 527 mV. Therefore, the actual junction voltage difference $\Delta V_{\mathrm{j}}^{\mathrm{el}}$ from EL should also be in this range instead of only $\Delta V_{\mathrm{j}}^{\mathrm{corr}} = 120$ mV (see the voltage curve with open stars). The deviation of 407 mV between ΔV_{oc} and $\Delta V_{\mathrm{j}}^{\mathrm{corr}}$ shows that stray light significantly affects the quantitative evaluation of the junction voltage of heavily shunted cells, and the simple correction method for stray light mentioned here is insufficient.

As shown in Fig. 3.5, the absolute junction voltage of each individual non-shunted cell obtained from EL images, both for uncorrected and corrected for stray light, agrees well with the measured open-circuit voltage, which means that stray light does not affect the quantitative EL analysis of the non-shunted cells.

3.2. Luminescence spectroscopy

In this work, spectrally resolved EL and PL experiments are carried out for CIGS solar cells to validate the reciprocity theorem (chapter 4). Furthermore, EL and PL spectroscopy is also applied to investigate defects in CIGS devices (see chapter 6), and the analysis of *a*-Si:H solar cells in chapter 7.

For the spectrally resolved EL and PL experiments, the charge carriers are injected into the sample either by a pulsed power source (EL) or a laser (PL). The charge carriers then radiatively recombine and the resultant luminescence intensity is recorded by a detector.

In this work, the samples were mounted in a cryostat, which ensures stabilized temperature and also enables the measurements in a temperature range of $70 \leq T \leq 500$ K. This thesis only focuses on the analysis of the EL and PL spectra at room temperature $T = 300$ K.

The EL and PL spectra shown in this work are measured both by Fourier transform infrared spectrometer (FTIR) and dispersive spectrometer. The two different

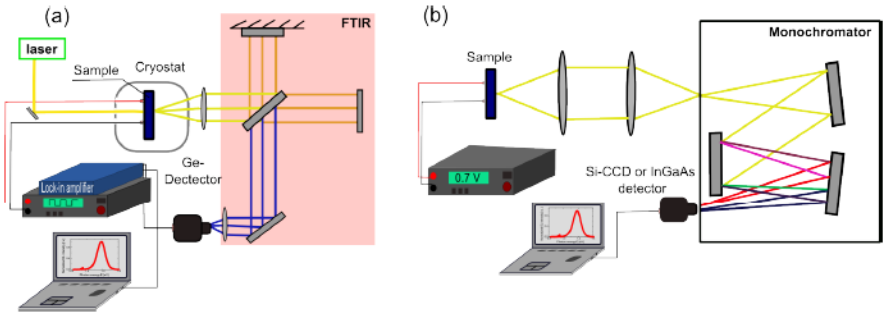

Figure 3.6.: Setup for the spectrally resolved EL and PL measurements. (a) Schematic of a Fourier transform infrared spectrometer (FTIR) in step-scan mode for the use of lock-in technique, (b) Schematic of a dispersive spectrometer.

setups for EL and PL spectroscopy are illustrated in Fig. 3.6; (a) FTIR spectrometer and (b) dispersive spectrometer.

A Fourier transform infrared spectrometer equipped with a calibrated liquid nitrogen cooled Ge-detector (Fig. 3.6(a)) is used to measure the spectral emission of the sample. The Ge-detector is sensitive in the photon energy range between 0.7 eV and 1.6 eV. In order to enhance the signal to noise ratio, a lock-in technique is used by electro-modulating the sample at a frequency of $f = 68$ Hz. The recorded luminescence is then collected by the Ge-detector, which yields an interferogram. Fourier-transformation of this interferogram finally yields luminescence spectra.

For the measurement of the PL spectra presented in this work, different laser illuminations at wavelengths $\lambda = [473, 532, 671]$ nm are used. The light intensity of the lasers is compared to a calibrated reference diode. During the PL measurements, the illuminated sample is electro-modulated (EM) with a periodic rectangular AC voltage between $V_j = 0$ V at short circuit (SC) and $V_j = V_{oc}$ at open circuit voltage (OV) conditions.

The spectrally resolved EL measurements are carried out by electro-modulation between $V_j = 0$ V and an applied forward junction voltage V_j to the solar cell. The luminescence resulting from radiative recombination of the charge carriers is recorded by the Ge-detector. The measured EL and PL spectra are corrected by a known spectrum of a calibration lamp.

A dispersive spectrometer has also been used to measure PL and EL spectra, which uses gratings to disperse the emitted light from the sample (see Fig. 3.6(b)). The dispersed light from the sample is collected by a Si-CCD or an InGaAs camera. Cooling of the cameras and long exposure times yield a high signal-to-noise ratio.

The advantages of FTIR over dispertive spectrometers are, e.g., faster measurements, better suppression of stray light, and a higher signal-to-noise ratio if the FTIR is used in connection with lock-in technique [91]. However, our FTIR setup allows the measurements of small samples of approximately (1.2×1.2 cm^2), for large modules (30×30 cm^2), which are also measured for this thesis, our setup with the dispertive spectrometer is more suitable.

3.3. Lock-in thermography

Lock-in thermography (LIT) is widely used for the detection of local heat variations caused by defects such as shunts in photovoltaic devices [27, 92]. The lock-in technique is used to allow the detection of very small temperature differences across the sample, since noise and signals arising from undesirable frequencies are filtered out. Therefore, in the case of LIT measurements, ambient light does not substantially introduce measurement error.

For LIT measurements, the sample is excited by a periodic excitation source, i.e. either an applied voltage or illumination. Due to the different excitation sources, two LIT methods are introduced, i.e. dark lock-in thermography (DLIT) using a modulated voltage as an excitation source [27,93,94] and illuminated lock-in thermography (ILIT) using LED panels or lasers for the illumination of the sample [95–97]. Through the excitation process, local current flows in the device and results in power dissipation in form of heat emission, which is detected by an infrared (IR) camera.

If the sample contains shunts, the shunts will create a path with low resistivity, where current favorably flows through. Therefore, the current density in the shunted regions is much higher than that of the surrounding, which causes high local dissipated power in the shunts. Hence, shunts appear in LIT images as bright/hot spots.

In this work, DLIT measurements used for the detection of shunts in CIGS solar cells and modules were carried out. Therefore, a DLIT setup is shown in

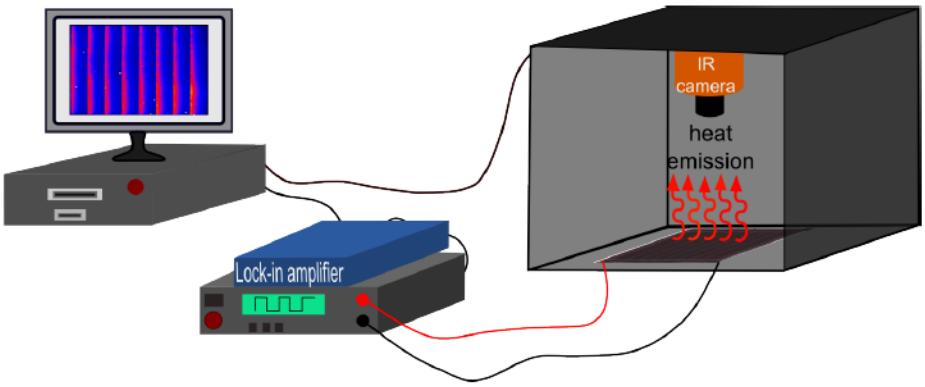

Figure 3.7.: Setup for the lock-in thermography measurements.

Fig. 3.7. The setup includes an IR camera, a computer as a control unit, and a pulsed power source. The IR camera used for the DLIT measurements in this thesis has an InSb detector, and is from Thermosensorik GmbH. The camera has a resolution of (640 × 512 pixels), and allows the detection of heat emission in the spectral ranges of short wave infrared (SWIR: 1 µm to 2.5 µm) and mid wave infrared (MWIR: 3 µm to 5 µm). For the full resolution of (640 × 512 pixels), the maximal lock-in frequency is 42 Hz, and for the reduced resolution of (256 × 256 pixels), the maximal lock-in frequency is 100 Hz.

4. Electroluminescence analysis of CIGS solar devices

This chapter focuses on the analysis of the EL and PL spectra and EL images of CIGS solar cells and modules measured at room temperature. The results from the spectrally resolved measurements serve as a validation of the reciprocity theorem [43, 44] applied to industrially produced CIGS solar cells and modules. The validity of the reciprocity theorem is especially important for the quantitative analysis of spatially resolved EL. Furthermore, both spectrally resolved luminescence and spatially resolved EL exhibit the metastable changes in CIGS devices.

4.1. Introduction

Recently, both spectrally and spatially resolved EL have been applied to CIGS solar cells and solar modules [38, 39, 58, 60, 98–102]. However, the basic principles and the physical preconditions justifying a simple quantitative interpretation of EL measurements are usually not scrutinized. This chapter is divided into two parts, in which the quantitative analysis of the EL and PL spectra of a CIGS solar cell (Sec. 4.3) and the quantitative interpretation of EL images of a CIGS module (Sec. 4.4) are represented, respectively. The quantitative EL analysis of CIGS solar cells and modules is based on the reciprocity relation between EL emission and external photovoltaic quantum efficiency $Q_e(E)$ [43, 44]. Therefore, the analysis of the EL and PL spectra especially focuses on the question, whether all aspects of this reciprocity relation are valid for industrially produced CIGS solar cells. The application of the reciprocity relation for the detailed analysis of EL images of CIGS solar modules is presented in the second part of this chapter.

Since metastable changes are important issues in CIGS solar devices, which

affect the quantitative interpretation of the experimental results presented in this thesis. Therefore, a brief introduction about these metastable changes is given here, which helps to clarify the metastable effects observed in both spectrally and spatially resolved EL measurements.

CIGS solar cells and modules are subject to metastable changes of their electronic properties upon voltage and/or light bias [103–108]. These metastable changes enhance the device efficiencies due to the improvement of the open-circuit voltage V_{oc} [109–111] or/and the fillfactor (FF) [112, 113]. The metastable improvement in CIGS contraries to the light-induced degradation in a-Si:H (also known as the Staebler and Wronski effect [114]), which is characterized by the degradation of the conductivity under illumination, and is reversible by annealing at temperatures of about 425 K [115].

Besides the enhancement of V_{oc} and FF under bias or illumination, the metastable changes during measurement time, however, challenge the electrical characterization of CIGS devices, e.g., J/V characteristics [116], Hall [107], EL [111] and EBIC [117]. Several metastable states occur in CIGS solar devices have been identified [118], e.g., relaxed state or initial state, light soaking states (red light soaking, blue light soaking, white light soaking), forward bias. In this work, three states, namely, the initial state, the white light soaking state, and the forward bias are considered. The initial state is obtained by keeping the sample in the dark without bias applied voltage at either room temperature or at elevated temperature $\approx$ 330-340 K overnight. The white light soaked state occurs under AM1.5G illumination and often at elevated temperature $\approx$ 330-350 K, and no voltage is applied to the sample. In this work, the term light soaking (LS) refers only to the white light soaking experiments. The forward bias state is reached if a forward bias voltage or current is applied to the sample, which also results in an increase of the open-circuit voltage [109].

Figure 4.1 shows the open-circuit voltage per cell $V_{\mathrm{oc,cell}}$ during three hours of light soaking under illumination of 1000 W/cm^2 and at a temperature of 50°C. The open-circuit voltage is measured directly after the sample was kept in the dark for $\approx$ 18 h for the sample to obtain its initial state. An increase of $V_{\mathrm{oc,cell}} \approx 6$ mV over the exposure time t is gained. The increase of the open-circuit voltage at high temperature range of 340 to 390 K was reported and analyzed in detail in Ref. [110].

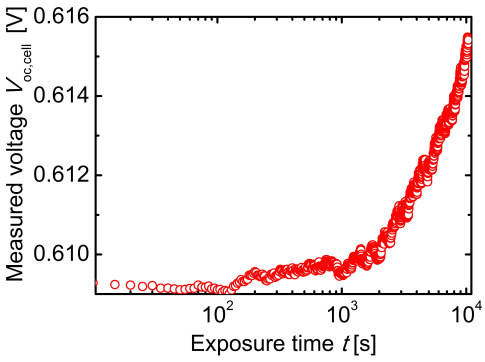

Figure 4.1.: Measured open-circuit voltage $V_{\mathrm{oc,cell}}$ per cell during three hours of light soaking under illumination of 1000 W/cm^2.

The increase of the open-circuit voltage under illumination is due to persistent photoconductivity in the bulk of the CIGS absorber [105–107], whereas the increase of the fill factor is more likely due to effects occurring close to the heterojunction [106]. Recently, the experiments results introduced by Refs. [111, 119, 120] suggest that the various metastable effects stem from a common origin, i.e the amphoteric behavior of the Se-Cu divacancy complex. The simulation results from Lany and Zunger explained that the metastable changes are an intrinsic property of the CIGS absorber material and are due to $V_{\mathrm{Cu}} - V_{\mathrm{Se}}$ divacancy complex and/or the $\mathrm{In_{Cu}}$ antisite defect [121]. Since both defects exist in multiple charge states, their influence on the electronic behavior of CIGS solar cells is rather complex, e.g. already in equilibrium the divacancy complex has three different charge configurations, namely $(V_{\mathrm{Cu}} - V_{\mathrm{Se}})^{+}$, $(V_{\mathrm{Cu}} - V_{\mathrm{Se}})^{-}$, and $(V_{\mathrm{Cu}} - V_{\mathrm{Se}})^{3-}$, dependent on the position in the band diagram of the ZnO/CdS/CIGS heterostructure [122–124] (Fig. 4.2(a)).

Injection of excess minority charge carriers via illumination or electrical bias, i.e. electrons into the neutral bulk, as well as holes into the inverted CdS/CIGS interface region will have a manifold of consequences on the charge distribution and on the electrical properties of the device (Fig. 4.2(b)). The reaction $(V_{\mathrm{Cu}} - V_{\mathrm{Se}})^{+} + e^{-} \rightarrow (V_{\mathrm{Cu}} - V_{\mathrm{Se}})^{-} + h^{+}$ will take preferably place in the neutral bulk and

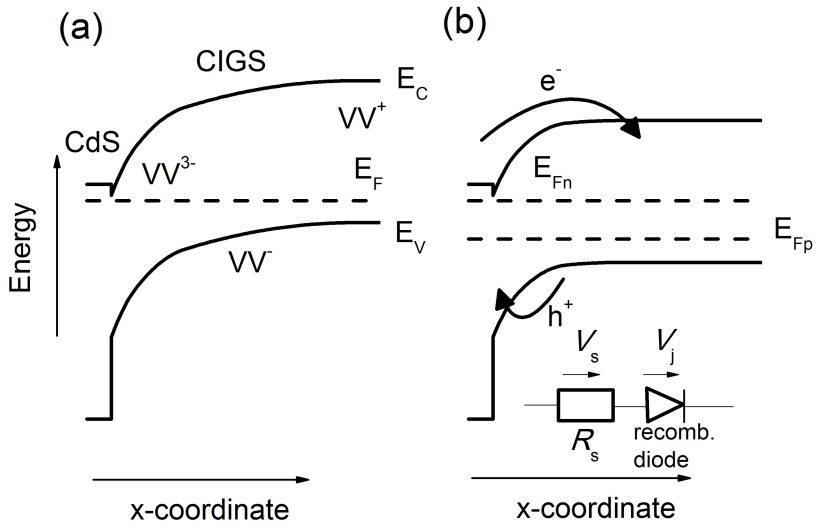

Figure 4.2.: (a) Sketch of the equilibrium band diagram of the CdS/CIGS heterojunction involving the three charge states $(V_{\mathrm{Cu}}-V_{\mathrm{Se}})^{+}$, $(V_{\mathrm{Cu}}-V_{\mathrm{Se}})^{-}$, and $(V_{\mathrm{Cu}}-V_{\mathrm{Se}})^{3-}$ of the divacancy. (b) Under light or current bias excess holes diminish the negative charge close to the CdS/CIGS interface and excess electrons increase the effective doping in the bulk of the material. The inset in (b) shows both elements of the equivalent circuit, the series resistor and the main diode that are affected by the metastable changes.

at the edge of the space charge region (SCR) leading to an increase of net doping density, thereby reducing the series resistance as well as the width of the SCR. The latter effect will reduce the overall recombination and lead to what is known as the relaxation (increase) of the open circuit voltage V_{oc} [105–107]. In contrast, the reaction $(V_{\mathrm{Cu}}-V_{\mathrm{Se}})^{3-}+2h^{+} \rightarrow (V_{\mathrm{Cu}}-V_{\mathrm{Se}})^{-}$ taking place closer to the interface region will decrease the net doping and widen the SCR.

Furthermore, the capture of holes into the state will further diminish the neg-

ative charge density in the close to interface region. As a consequence, the collection/injection barrier [117] for electrons at the CdS/CIGS interface will be decreased. Eventually, injection of minority carriers as sketched in Fig. 4.2(b) will at least result into two quite different effects: (i) the reduction of the recombination current and (ii) the reduction of the series resistance. Notably, these two effects correspond to the commonly observed features during light soaking of CIGS modules or solar cells: the increase of open circuit voltage and the increase of fill factor. Both effects are also expected to influence the EL emission of the device, since even in the simplest equivalent circuit consisting of a series resistor and a diode as sketched in the inset of Fig. 4.2(b).

4.2. Experimental conditions

This section describes the experimental conditions, under which the spectrally resolved EL and PL and the spatially resolved EL measurements are carried out in this work. For the luminescence spectroscopy measurements, the sample are CIGS solar cells (4×9 cm^2) cut from a (30×30 cm^2) CIGS solar module, which has an efficiency of 12.7% and $V_{\mathrm{oc,cell}} = 665$ mV. The different manufacturing processes of the CIGS modules are described in Sec. 2.3.1. Detailed information about the spectroscopy measurement setup and the experimental procedure are given in Sec.3.2.

Light soaking experiments were performed, in which the same samples were illuminated at $T = 400$ K for almost 3 h with illumination intensity of approximately one sun for the samples to achieve their saturated state. After this LS process, the EL and PL spectra of the samples were subsequently measured to investigate the consequences of LS on the EL and PL intensities and their superimpose behavior. The results of the spectral measurements are represented in Sec. 4.3.

The spatially EL measurements are carried out for a large (30×30 cm^2) CIGS module with an efficiency of 13.5% and $V_{\mathrm{oc,cell}} = 661$ mV. Electroluminescence images are taken one after another during the bias experiment to investigate the transient effects visible in EL images. Prior to the transient measurements, the sample was kept in the dark for ≈ 12 h at room temperature for the sample to reach its initial state. Bias experiment is performed by either applying a constant voltage to the sample or injecting a constant current into the sample. Immediately after the appli-

cation of constant voltage or current bias, EL images are recorded every five seconds with a Si-CCD camera. The analysis of the EL images are presented in Sec. 4.4.

4.3. Analysis of luminescence spectra[1]

This section shows the quantitative analysis of the measured EL and EM spectra of a CIGS solar cell, and thereby, validates the reciprocity theorem given by Eq. 4.1

$$\phi_{\mathrm{em}}(E) = \phi_{\mathrm{sc}}(E, \phi_{\mathrm{exc}}) + \phi_{\mathrm{el}}(E, V_{\mathrm{j}}) = \phi_{\mathrm{sc}}(E, \phi_{\mathrm{exc}}) + Q_{\mathrm{e}}\phi_{\mathrm{bb}}(E)\left[\exp\left(\frac{qV_{\mathrm{j}}}{kT}\right) - 1\right], \tag{4.1}$$

for more detailed see Sec. 2.2. The validity of the reciprocity relation requires: (i) a quantitative relation between ϕ_{em} and $Q_{\mathrm{e}}(E)$, (ii) a linear superposition of EL emission ϕ_{el} from the driven voltage V_{j} and short circuit (SC) emission ϕ_{sc}, (iii) that the spectral shape of the EL emission is unaltered at different bias conditions, and (iv) that the EL emission ϕ_{em} follows a diode law with a radiative ideality factor of unity [44]. For the quantitative analysis of the EL measurements, it is of utmost importance to verify the implications (i) to (iv). Note that detailed information about the setup and measurement techniques for the EL and PL spectra can be found in Secs. 3.2 and 4.2.

Up to now, the validity of the implications (i) and (iii) have been verified for crystalline silicon solar cells [60,61], high efficiency CIGS solar cells from laboratory [58, 60], organic solar cells [41], and GaInP/GaInAs/Ge multijunction solar cells [57, 62]. In the following, the validity of the predictions (i) and (iii) is verified for industrially produced CIGS solar cells.

Figure 4.3 shows the measured EL spectrum $\phi_{\mathrm{el,direct}}(E)$ of a (4×9 cm^2) CIGS solar cell (solid line). According to Eq. (2.29), the external quantum efficiency $Q_{\mathrm{e,el}}(E)$ (solid line) is then calculated from the measured EL spectrum $\phi_{\mathrm{el,direct}}(E)$. Vice versa, the EL spectrum $\phi_{\mathrm{el,Qe}}$ (open triangles) can be determined from the measured external quantum efficiency $Q_{\mathrm{e,direct}}(E)$ (open triangles) as well. The solid curves and the open triangles presented in Fig. 4.3 indicate that the calculated EL spectrum $\phi_{\mathrm{el,Qe}}$ agrees well with the experimental EL spectrum $\phi_{\mathrm{el,direct}}(E)$, and the calculated $Q_{\mathrm{e,el}}(E)$ fits consistently well to the measured $Q_{\mathrm{e,direct}}(E)$. These results

[1] Work jointly carried out with T.M.C. Müller as published in [125]

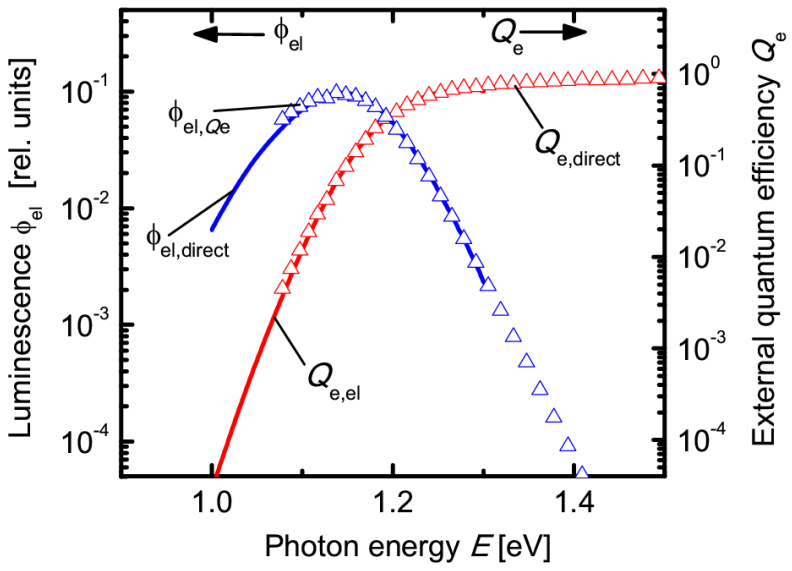

Figure 4.3.: Figure 4.3 shows: EL spectrum $\phi_{\mathrm{el,direct}}(E)$ of a CIGS solar cell (4×9 cm^2) measured by a Ge-detector at room temperature $T = 300$ K (solid line), the calculated external quantum efficiency $Q_{\mathrm{e,el}}(E)$ from Eq. (2.29) (solid line), the measured $Q_{\mathrm{e,direct}}(E)$ (open triangles), and the calculated EL spectrum $\phi_{\mathrm{el,Qe}}$ from the experimental external quantum efficiency $Q_{\mathrm{e,direct}}(E)$ (open triangles).

ensure the quantitative determination of $Q_{\mathrm{e,el}}(E)$ from $\phi_{\mathrm{el,direct}}(E)$ and of $\phi_{\mathrm{el,direct}}(E)$ from $Q_{\mathrm{e,direct}}(E)$ for industrially produced CIGS solar cells, which means that the implication (i) is also valid for such solar cells. The EL intensity $\phi_{\mathrm{el}}(E)$ given in Eq. (2.29) can be now written as

$$\phi_{\mathrm{el}}(E) \propto Q_{\mathrm{e}}(E) \exp\left(\frac{qV}{kT}\right). \tag{4.2}$$

The validity of the implication (iii), i.e., the EL spectra are unaltered under different bias conditions, is tested for the same CIGS sample as shown in Fig. 4.3. For this reason, EL spectra are measured at various injection current densities $J =$

[35.8, 17.2, 7.3] mAcm^{-2} before light soaking (LS) and $J = [28.9, 6.8, 0.8]$ mAcm^{-2} after LS. Figure 4.4 shows the EL spectra (open circles) before LS (a) and after LS (b). In both cases, the shapes of the EL emission measured under different injection current densities J are unaltered, which means that the EL spectra are independent of bias conditions. This result states that the precondition (iii) is validated for industrial CIGS devices. The validity of the requirement (iii) also points to the fact that the EL intensity $\phi_{\mathrm{el}}(E)$ is directly proportional to the external quantum efficiency $Q_{\mathrm{e}}(E)$ by a constant proportionality factor $\exp(qV/kT)$.

The implication (ii) presupposes that EL emission ϕ_{el} and SC emission ϕ_{sc} superimpose linearly. In order to check for the validity of (ii), PL spectra of the same sample are measured. As mentioned in Sec.3.2, the PL spectra are measured using electro-modulation techniques (EM) switching the applied junction voltage between $V_{\mathrm{j}} = 0$ V (SC condition) and the illumination corresponding the open-circuit voltage $V_{\mathrm{j}} = V_{\mathrm{oc}}$ (OV condition). Therefore, in this thesis the measured PL spectra are EM spectra. Note that the EM spectra are obtained from the measurements carried out at an illumination leading to short circuit current densities J_{sc} equaling the injection current densities J from the EL measurements. The derivation between J_{sc} and J is $\approx 4\%$.

Figure 4.4 shows the EM spectra (solid lines) before LS (a) and after LS (b). Both the EM spectra before and after LS are unaffected by the applied bias conditions, which is the same as already shown for the EL spectra. Furthermore, it is also expected that the EL emission measured at different injection current densities J should be the same as the EM emission measured at $J_{\mathrm{sc}} = J$. Surprisingly, a discrepancy between the EL and EM intensities is observed. At low injection current densities $J = 7.3$ mAcm^{-2} before LS (Fig. 4.4(a)) and $J = [0.8, 6.8]$ mAcm^{-2} after LS (Fig. 4.4(b)), only a slight deviation between the EL and EM emission is observed. At higher injection current densities, the EM intensity is noticeably higher than the EL intensity. To highlight the difference between the EL and EM emission, the intensity ratios $\Theta_{\mathrm{el}} = \phi_{\mathrm{el}}/\phi_{\mathrm{EM,max}}$ of the EL spectra (open circles) and $\Theta_{\mathrm{EM}} = \phi_{\mathrm{EM}}/\phi_{\mathrm{EM,max}}$ (solid lines) of the EM spectra are illustrated in Fig. 4.4 before LS (c) and after LS (d). The observation exhibited in Figs. 4.4(a,b) is also reflected in Figs. 4.4(c,d). Moreover, the difference in the intensity ratios Θ_{el} and Θ_{EM} at $J = 7.3$ mAcm^{-2} before LS is more pronounced than the discrepancy between the

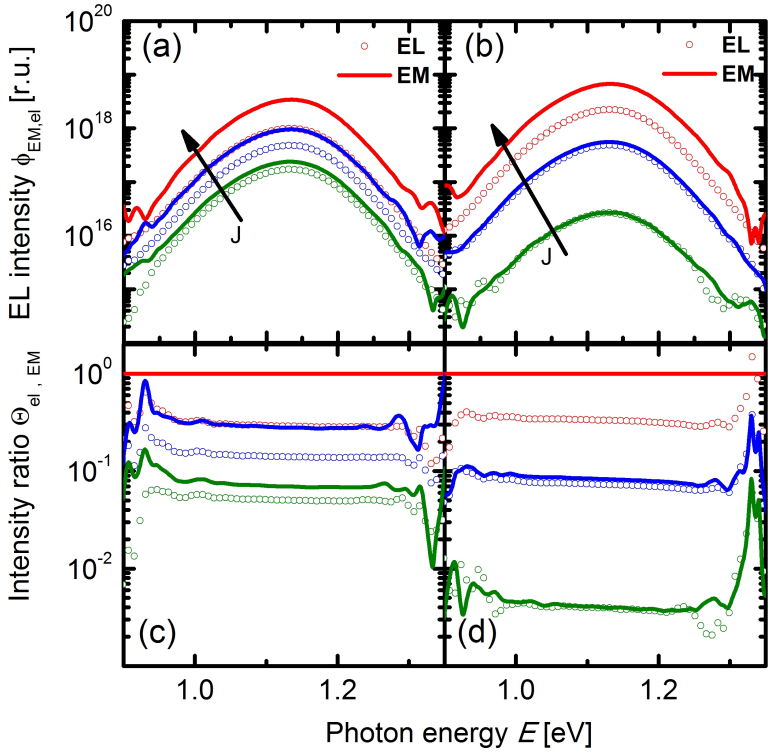

Figure 4.4.: EL spectra (open circles), EM spectra (solid lines) of the same investigated solar cell (4×9 cm^2) measured under different injection current densities at room temperature $T = 300$ K: (a) before light soaking (LS) at different injection current densities $J = [35.8, 17.2, 7.3]$ mAcm^{-2} (EL), $J_{sc} = J$ (EM). (b) after LS of 3 h at $T = 400$ K and $J = [28.9, 6.8, 0.8]$ mAcm^{-2} (EL), $J_{sc} = J$ (EM). (c) Intensity ratios $\Theta_{el} = \phi_{el}/\phi_{EM,max}$ of the EL spectra (open circles) and $\Theta_{EM} = \phi_{EM}/\phi_{EM,max}$ of the EL spectra (solid lines) shown in (a) before LS. (d) Intensity ratios Θ_{el} (open circles) and Θ_{EM} (solid lines) shown in (b) after LS.

EL and EM intensities at $J = 7.3$ mAcm^{-2} illustrated in Fig. 4.4(a). After LS, the intensity ratios $\Theta_{\rm el}$ equals $\Theta_{\rm EM}$ at $J = [0.8, 6.8]$ mAcm^{-2}, respectively.

The result presented in Fig. 4.4 points to the fact that the implication (ii) is only valid in a limited range of the injection current density and is affected by the history of the sample. For further investigation of the reason for the discrepancy between EL and EM emission, the integral or omni-spectral EL and EM intensities of the same investigated samples as in Fig. 4.4 are measured under larger range of injection current densities using a Ge-detector without FTIR. Figure 4.5(a) exhibits the omni-spectral EL $\phi_{\rm el}$ before/after LS (open/full squares) and omni-spectral EM $\phi_{\rm EM}$ before/after LS (open/full circles) vs. the applied voltage V and $V = V_{\rm oc}$, respectively. In the low voltage regime ($V = V_{\rm oc} \leq 0.6$), the logarithm of the omni-spectral EM and EL follow a straight line and the integral EL intensity is almost the same as the integral EM intensity, which is consistent with the results presented in Fig. 4.4 at low injection current densities. At the voltage above 0.6 V, the integral EL data saturate because of the series resistance. The saturation of EL curve reduces after LS performance due to a reduction of the series resistance (see Sec. 4.4.2). Moreover, at the voltage above 0.6 V, the EM curve slightly deviates from straight line in both cases, before and after LS. The straight line presents the fit of Eq. (4.3) to the EM curve, which yield a radiative ideality factor $n_{\rm r} = 0.96$. The radiative ideality factor $n_{\rm r}$ is defined as

$$n_{\rm r}(V_{\rm oc}) = \frac{q}{kT}\left.\frac{dV_{\rm oc}}{d\ln(\phi_{\rm EM})}\right|_{J_{\rm sc}=J} = \frac{q}{kT}\left.\frac{dV_{\rm oc}}{d\phi_{\rm EM}}\phi_{\rm EM}\right|_{J_{\rm sc}=J}. \tag{4.3}$$

The deviation of the value $n_{\rm r} = 0.96$ from unity may result from a slight dependence of the voltage on the current collection [126]. However, the value of $n_{\rm r}$ is also not affected by light soaking.

Figure 4.5(b) exhibits the short-circuit current density/open-circuit voltage $J_{\rm sc}/V_{\rm oc}$ characteristics before/after LS (open/full circles), which are measured simultaneously to the EM measurements, and the current density/voltage J/V characteristics before/after LS (open/full squares), which are carried out simultaneously to the EL measurements. At the voltage above 0.6 V, the series resistance is also responsible for the saturation of the J/V curve. After light soaking, both $J_{\rm sc}/V_{\rm oc}$ and J/V shift to higher voltages due to the increase of the open-circuit voltage and the reduction of the series resistance under illumination [53, 109]. The non-radiative

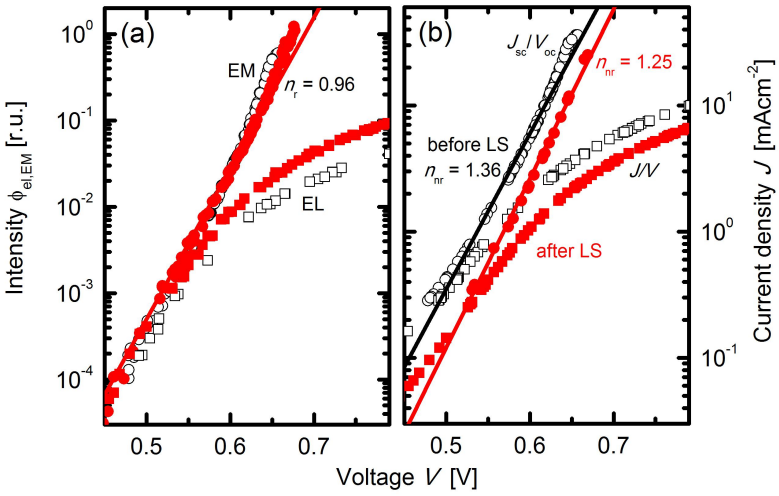

Figure 4.5.: (a) The omni-spectral EL ϕ_{el} vs. voltage V before/after light soaking (LS) (open/full squares) and the omni-spectral EM ϕ_{EM} vs. voltage $V = V_{oc}$ before/after LS (open/full circles) of the same samples as in Fig. 4.4. The radiative ideality factor $n_r = 0.96$ is obtained from the fit (red solid line) to $\phi_{EM,voc}$ before and after LS. (b) Short-circuit current density/open-circuit voltage J_{sc}/V_{oc} characteristics before/after LS (open/full circles) are measured simultaneously to the EM measurements, and current density/voltage J/V characteristics before/after LS (open/full squares) are carried out simultaneously to the EL measurements. The non-radiative ideality factor $n_{nr} = 1.36$ (before LS) and $n_{nr} = 1.25$ (after LS) results from the fit to J_{sc}/V_{oc} before LS/after LS (black solid line/red solid line).

ideality factor is given by

$$n_{nr} = \frac{q}{kT}\frac{dV_{oc}}{d\ln(J_{sc})}\bigg|_{J_{sc}} = \frac{q}{kT}\frac{dV_{oc}}{dJ_{sc}}J_{sc}\bigg|_{J_{sc}}. \tag{4.4}$$

From the fits of Eq. (4.4) to the J_{sc}/V_{oc} characteristics before and after LS, the non-radiative ideality factors n_{nr} are determined, i.e. $n_{nr} = 1.36$ before LS and $n_{nr} = 1.25$ after LS.

The value of n_{nr} becomes smaller after LS because the width of the space charge

region reduces, which causes the reduction of the non-radiative recombination in the devices. Furthermore, it is obvious that the non-raditave ideality factor n_{nr} is larger than the radiative ideality factor n_{r}.

Figure 4.6(a), expresses ϕ_{el} vs. current density J before/after LS (open/closed squares) and ϕ_{EM} vs. current density $J = J_{\mathrm{sc}}$ before/after LS (open/closed circles)of the same samples as in Fig. 4.4. Plotting ϕ_{el} and ϕ_{EM} vs. current density has a charming advantage, i.e. the elimination of the influence of the series resistance and the voltage as a parameter. Interesting is the fact that EL and EM curves deviate from each other in the injection current density range $J > 4$ mAcm^{-2} before light soaking. After light soaking, the deviation between EL and EM intensity occurs at larger injection current density $J > 15$ mAcm^{-2} and an abrupt increase of the EM intensity is observed at $J \approx 20$ mAcm^{-2}. The abnormal deviation of the integral EL and EM emission and the significant deviation of the experimental EM data from the straight line for $J > 4$ mAcm^{-2} and $J > 15$ mAcm^{-2} before and after LS, respectively, indicate a departure from the condition (iii) of Eq. (4.1). The ratio of the non-radiative and radiative ideality factor denoted as Γ is defined

$$\Gamma = \frac{n_{\mathrm{nr}}}{n_{\mathrm{r}}} = \frac{d\phi_{\mathrm{EM}}}{dV_{\mathrm{oc}}}\frac{1}{\phi_{\mathrm{EM}}} \Big/ \frac{dJ}{dV}\frac{1}{J}. \tag{4.5}$$

Fitting Eq. (4.5) to the EM curves before and after LS (straight lines) yields the values $\Gamma = 1.4$ and $\Gamma = 1.3$ before and after light soaking, respectively, because the value of n_{r} becomes smaller after LS.

Figure 4.6(b) exhibits the external luminescence efficiencies Q_{LED} vs. J before/after LS (open/closed squares) obtained from ϕ_{el} and Q_{lum} before/after LS (open/closed circles) vs. $J_{\mathrm{sc}} = J$ from ϕ_{EM}. The external luminescence efficiencies $Q_{\mathrm{LED,lum}}$ is defined as the ratio of the radiative recombination current density J_{r} and the total amount of J_{r} and the non-radiative recombination J_{nr} (see Eq. (2.40)). It follows

$$Q_{\mathrm{LED,lum}} = \frac{J_{\mathrm{r}}}{J_{\mathrm{r}} + J_{\mathrm{nr}}} = \frac{J_{\mathrm{r}}}{J}. \tag{4.6}$$

Equation (4.6) can also be expressed as the following proportionalities

$$Q_{\mathrm{LED}} \propto \frac{\phi_{\mathrm{el}}}{J} \tag{4.7}$$

and

$$Q_{\mathrm{lum}} \propto \frac{\phi_{\mathrm{EM}}}{J_{\mathrm{sc}}}. \tag{4.8}$$

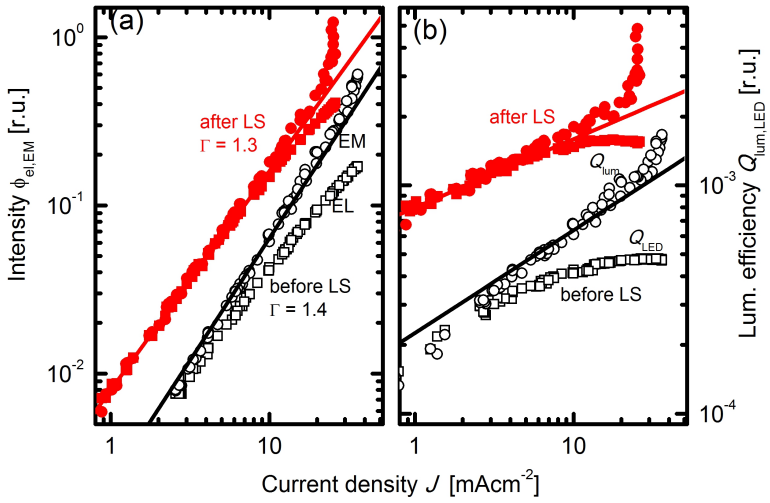

Figure 4.6.: (a) The omni-spectral EL ϕ_{el} vs. current density J before/after LS (open/closed squares) and the omni-spectral EM ϕ_{EM} vs. current density $J = J_{sc}$ before/after LS (open/closed circles) of the same samples as in Fig. 4.4. The ratio between the non-radiative and radiative ideality factors from Fig. 4.5 yields the slopes $\Gamma = 1.4$ (before LS) and $\Gamma = 1.3$ (after LS) due to Eq. (4.5). (b) External luminescence quantum efficiency efficiencies Q_{LED} before/after LS (open/closed squares) obtained from ϕ_{el} and Q_{lum} before/after LS (open/closed circles) calculated from ϕ_{EM} with the help of Eqs. (4.7) and (4.8). The black and red straight lines are directly determined from Γ in (a) and correspond to $\Gamma - 1$ in (b), respectively.

After light soaking, the external luminescence efficiencies significantly increase by a factor of three. This improvement can be explained by the reduction of the width of the SCR due to the effect of persistent conductivity and, consequently, the reduction of the amount of the non-radiative recombination. This effect is consistent with the observable shift of the J_{sc}/V_{oc} and J/V characteristics shown in Fig.4.5(b). Moreover, Fig. 4.6(b) also shows that the EL efficiency Q_{LED} obviously saturates at current densities $J > 10$ mAcm^{-2}, whereas the EM efficiency Q_{lum} dramatically

increases. The explanation for the increase of Q_{lum} bases on the assumption that the split of the quasi-Fermi levels in the bulk of the material is far larger than the open-circuit voltage V_{oc} detected at the terminals under illumination (EM). Therefore, with increasing illumination, Q_{lum} abruptly increases, whereas V_{oc} does not increase as expected. Such an effect would be explained by an electrostatic barrier between the main part of the CIGS bulk and the main region of non-radiative recombination [117]. Correspondingly, the observed saturation of Q_{LED} also results from this barrier, which hinders injection of electrons from the junction into the bulk. The defect model of Lany and Zunger may explain these observations [122]. The abnormal behavior shown in Figs. 4.6(a),(b) clearly expresses that the superposition principle is only valid in a limited injection range $J < 4$ mAcm^{-2} before light soaking, which can be expanded by light soaking $J < 15$ mAcm^{-2}.

Finally, the analysis of the spectrally resolved EL measurements at room temperature states the validity of (i), i.e. the relation between the external quantum efficiency and the EL emission of an industrially produced CIGS thin-film solar cell. The spectral shapes of the EL and EM emission measured at various injection current densities show that the EL and EM spectra are voltage-independent and are unaffected by LS (ii). A deviation between the EL and EM intensities at an injection current density $J > 4$ mAcm^{-2} (before LS) and $J > 15$ mAcm^{-2} (after LS) is observed. Therefore, the superposition principle (iii) is only warranted for a limited injection range and depends on the light soaking history of the sample. A radiative ideality factor close to unity is found (iv), which is unaffected by light soaking, whereas a non-radiative ideality factor larger than unity is determined, which becomes smaller after LS. Because of the reduction of the amount of the non-radiative recombination, the external luminescence efficiencies are found to be increased by a factor of three. The validation of the reciprocity theorem applied to CIGS solar devices is carried out using the EL and EM spectroscopy measurement results. Three of four requirements for the validity of the reciprocity theorem are met for such devices. However, the validity of all four preconditions (i) to (iv) plays an important role especially in the quantitative analysis of spatially resolved EL measurements.

4.4. Analysis of transient EL images

4.4.1. Determination of the transient juntion voltage

Before investigating the transient phenomena observed in CIGS modules via EL imaging, a brief description of determination of the transient junction voltage V_j is presented in the following part. The quantitative evaluation of the EL measurements is based on the reciprocity relation between EL emission $\phi_\mathrm{el}(E)$ and external photovoltaic quantum efficiency $Q_\mathrm{e}(E)$ according to Eq. (2.29) [43]. Inversion of Eq. (2.29) for $V_\mathrm{j} \gg kT/q$ yields

$$V_\mathrm{j} = \frac{kT}{q} \ln\left(\phi_\mathrm{el}(E)\right) + \mathrm{const} \tag{4.9}$$

and allows the determination of the junction voltage V_j except for a constant offset. The spatial distribution of the voltage V across a single cell of a thin-film module is given by

$$V(x) = V_\mathrm{b} - J_\mathrm{b} r + \frac{JwR_\mathrm{f}}{\lambda} \frac{\cosh[\lambda x]}{\sinh[\lambda w]} \tag{4.10}$$

$$\approx V_\mathrm{b} - J_\mathrm{b} r + Jr + JR_\mathrm{f}\left(\frac{x^2}{2} - \frac{w^2}{6}\right) \tag{4.11}$$

$$= V_\mathrm{b} + JR_\mathrm{f}\left(\frac{x^2}{2} - \frac{w^2}{6}\right), \tag{4.12}$$

where J denotes the current density averaged over the cell width, w the cell width, x the coordinate across the cell ($0 \leq x \leq w$), r the differential resistance between front and back contact, i.e. $r = dV/dJ$, and R_f the sheet resistance of the front window layer (back contact layer resistance is neglected). The quantity λ is given by $(R_\mathrm{f}/r)^{1/2}$. Note that Eq. (4.10) is a linear expansion around the base voltage V_b and the base current density J_b as outlined in Ref. [38]. As long as this linearization is a good approximation then Eq. (4.10) holds. Furthermore, the Laurent expansion of Eq. (4.10) around $\lambda = 0$ is used to derive the approximation in Eq. (4.11). Equation. (4.12) is obtained by setting $J_\mathrm{b} = J$. Note that Eq. (4.12) also means that V_b is chosen such that it equals the average value of $V(x)$.

Figure 4.7(a) depicts the voltage vs. current curves of the junction and the series resistance as used in the linearization leading to Eq. (4.10). As illustrated in Fig. 4.7(a), the voltage V in Eq. (4.10) is the sum $V = V_\mathrm{j} + V_\mathrm{s}$ of the junction

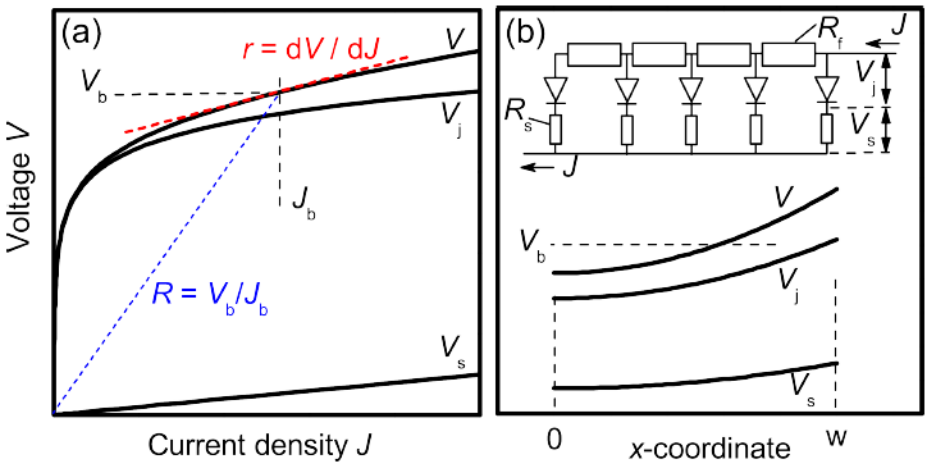

Figure 4.7.: (a) Schematic illustrating the voltage vs. current density curves for the voltage drops V_j and V_s over the junction and the series resistance, as well as $V = V_j + V_s$ for their series connection. Small voltage variations around the bias point (V_b, J_b) are linearized using the differential resistance $r = dV/dJ$, whereas the global resistance is given by $R = V_b/J_b$ as indicated by the short dashed lines. (b) Voltages $V_j(x), V_s(x)$, and $V(x) = V_j(x) + V_s(x)$ over a cell stripe $(x = 0...w)$ as given by Eqs. (4.10) and (4.13). The inset shows an equivalent circuit model for the voltage and current distribution along a cell stripe. The resistor R_f corresponds to the sheet resistance of the ZnO front contact, where the resistance of the Mo back contact is neglected.

voltage and the voltage drop V_s over the local series resistance. Accordingly, the global resistance R of this series connection at the bias point (V_b, J_b) is given by $R = V_b/J_b$, whereas the differential resistance is $r = dV/dJ$ as illustrated by the short dashed lines in Fig. 4.7(a). Furthermore, with the respective definitions for the global and differential junction and series resistances, it follows $R = R_j + R_s$ and $r = r_j + r_s$. Since the junction V_j is experimentally accessible by EL, whereas V_s is unknown, an expression for $V_j(x)$ has to be found. Because of the series connection, $V_j(x)$ is expanded around the point $V_j(J_b) = V_b R_j/R = J_b R_j$. The share of $V_j(x)$ from the spatial variations of $V(x)$ is given by the ratio r_j/r of the differential resistances.

With $J_b = J$, the local junction voltage $V_j(x)$ is obtained from

$$V_j(x) = JR_j + JR_f(\frac{x^2}{2} - \frac{w^2}{6})\frac{r_j}{r}. \tag{4.13}$$

Figure 4.7(b) schematically compares the junction voltage $V_j(x)$, the voltage drop $V_s(x)$ over the series resistance, and the voltage $V = V_j + V_s$. The inset shows an equivalent circuit illustrating in one dimension the current and voltage distribution over one cell stripe. Considering now metastable transients of V_j under constant current density, the transient voltage $V_j(x,t)$ over time t is calculated from Eq. (4.13), therefore, we obtained

$$V_j(x,t) = J(R_{j,0} + \Delta R_j(t)) + JR_f(\frac{x^2}{2} - \frac{w^2}{6})\frac{r_j}{r_0 + \Delta r(t)}. \tag{4.14}$$

Note that the differential resistance r_j of a diode is given by

$$r_j = \frac{n_{id}kT}{qJ} \tag{4.15}$$

and is not expected to change under constant current as long as the diode ideality factor n_{id} and thermal voltage kT/q are unchanged. Thus, transients of the EL intensity (corresponding to transients of V_j) under constant current bias are entirely determined by changes ΔR_j and ΔR_s.

4.4.2. Quantitative analysis of transient EL images

In the following, the results of the transient EL measurements are quantitatively analyzed. Note that detailed information about the experimental procedure is illustrated in Sec.4.2. Besides the determination of the transient junction voltage shown in Sec.4.4.1, the overview of the metastable changes introduced in Sec.4.1 is relevant for understanding the observable phenomena presented in this section. In this section, bias experiments are conducted at both constant applied voltage V_{ext} and constant current density J_{ext}.

Figure 4.8 shows EL images recorded from the central part of a CIGS module under application of a constant injection current density $J_{ext} = 34$ mAcm^{-2} (a), and of a constant voltage of $V_{ext} = 50$ V, corresponding to a mean voltage of ($V_{cell} = V_b = 0.78$ V) per cell (b), after 5 s and after 195 s during the bias experiments. Note that the cell voltage V_{cell} obtained from the experiments corresponds to the

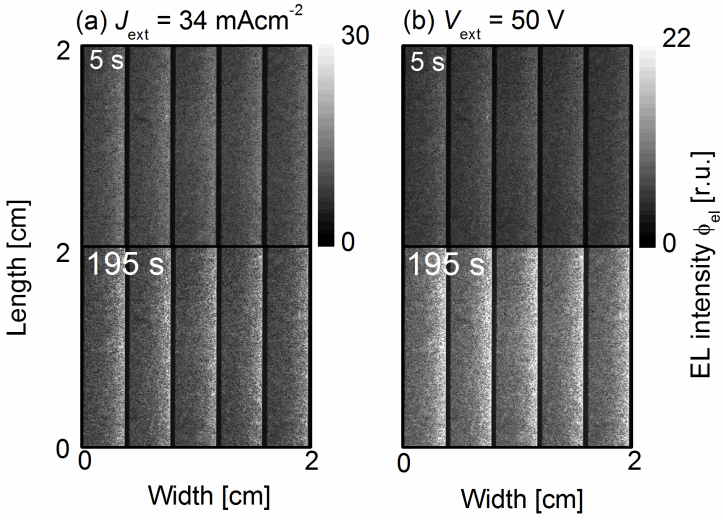

Figure 4.8.: EL images showing a detail of the emission of the mini-module (2×2 cm^2), which are recorded at: (a) constant injection current density J_{ext} = 34 mAcm^{-2}, (b) constant applied voltage V_{ext} = 50 V (V_{cell} = 0.78 V) after 5 s and after 195 s, respectively. The initial state was prepared by keeping the module in the dark for more than 12 h at ambient temperature.

voltage V_b used in Eq. (4.10). The EL images show the resistive effect of the ZnO sheet resistance R_f, i.e. the characteristic decay of the EL intensity ϕ_{el} from the right to the left of the cell as expected from Eq. (4.10). Furthermore, Fig. 4.8 also illustrates that the overall EL intensity from EL images recorded at the end (after 195 s) is brighter than at the beginning (after 5 s) in both situations: (a) injection of a constant current density J_{ext} = 34 mAcm^{-2} into the sample or (b) application of a constant voltage V_{ext} = 50 V (V_{cell} = 0.78 V) to the sample. Moreover, the increase of the EL intensity from the series of EL images (after 5 s and 195 s) shown in Fig. 4.8(b) is more significant than that shown in Fig. 4.8(a).

Figure 4.9 displays the average EL intensity obtained from averaging the EL intensity in both length and width directions of the EL image measured at a constant

current density of $J_{ext} = 34\ \mathrm{mAcm}^{-2}$ (filled circles) and at a constant applied voltage $V_{ext} = 50$ V (open circles), respectively, during the exposure time $t = 195$ s. The EL versus t curve exhibits that the EL intensity continuously increases during the forward bias experiment either with a constant current density or a constant applied voltage. Additionally, it is obvious that the increase of the EL intensity during the measurement time is much larger for constant applied voltage V_{ext} than for constant injection current density J_{ext}.

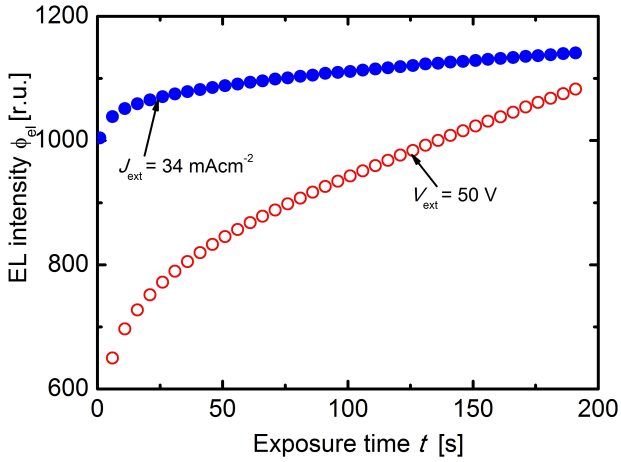

Figure 4.9.: Averaged EL intensity during the exposure time t of 195 s at a constant current density of $J_{ext} = 34\ \mathrm{mAcm}^{-2}$ (filled circles) and at a constant applied voltage of $V_{ext} = 50$ V (open circles).

Moreover, Fig. 4.10 displays the line-scans of the relative junction voltage extracted from EL images (Fig. 4.8) based on Eq. (4.9). The line-scans quantitatively show that the increase of the local junction voltage $V_j(x)$ resulting from EL experiment under a constant applied voltage in Fig. 4.10(b) is more pronounced than under a constant injection current density in Fig. 4.10(a). The effect of the series resistance of the front electrode is also clearly observable in Fig. 4.10 due to the decrease of the relative junction voltage within one cell.

From the line-scans of the relative junction voltage shown in Fig. 4.10, the average junction voltage V_j of the entire module is extracted. Note that the abso-

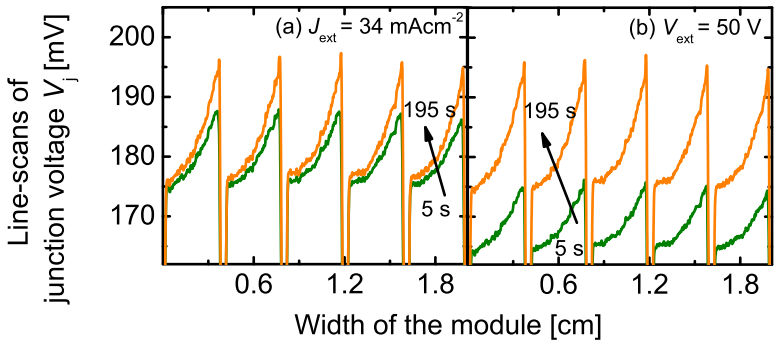

Figure 4.10.: Line-scans of the relative junction voltage determined from EL images shown in Fig. 4.8, which are recorded at: (a) a constant injection current density $J_{ext} = 34$ mAcm^{-2}, (b) a constant applied voltage $V_{ext} = 50$ V ($V_{cell} = 0.78$ V) after 5 s and after 195 s, respectively.

lute junction voltage of the entire module calculated from the EL measurements (Eq. (4.9)) have an unknown offset, which is the same for all images, therefore, it is possible to record the transient behavior of the average junction voltage V_j of the entire module over measured time. Figure 4.11(a) illustrates the transients of the average junction voltage V_j (filled circles) calculated from a series of EL images with the help of Eq. (4.9) and of the external voltage (open stars) V_{ext} under a constant current bias ($I = 400$ mA or $J_{ext} = 34$ mAcm^{-2}). The transients show an increase of the average junction voltage ($\Delta V_j = V_j(195s) - V_j(0s) \approx 3.5$ mV) during 195 s measurement time. Furthermore, Fig. 4.11(a) (open stars) unveils a decrease of the external cell voltage V_{cell} from approximately 850 mV/cell to 790 mV/cell corresponding to a decrease of the overall module resistance from 25 Ωcm^2/cell to 23.2 Ωcm^2/cell.

Analogously, EL experiments under a constant applied voltage of $V_{ext} = 50$ V or $V_{cell} = 0.78$ V show an increase of the average junction voltage $\Delta V_j \approx 12$ mV (Fig. 4.11(b), filled circles), which is obviously larger than ΔV_j resulting from the EL experiments under a constant injection current density. At the same time, the external current density J_{ext} through the device increases from 23 mAcm^{-2} to 32

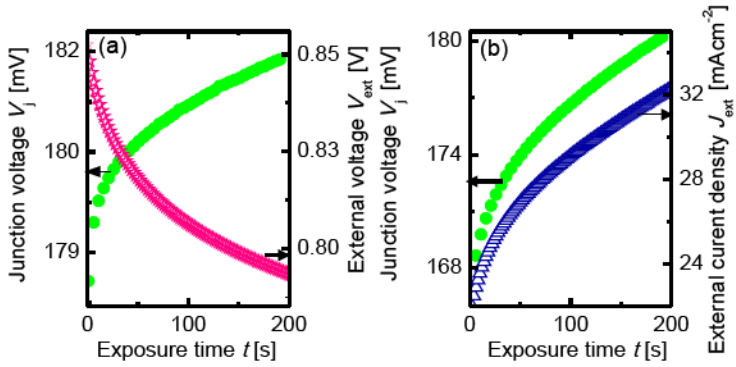

Figure 4.11.: Transients of the average junction voltage V_j (filled circles) calculated from a series of EL images with the help of Eq. (4.9) and of the external voltage (open stars) V_{ext} under a constant current bias ($I = 400$ mA or $J_{ext} = 34$ mAcm^{-2}). The transients show a decrease of V_{ext} and a simultaneous increase of the junction voltage. (b) Experiment with a constant applied voltage $V_{ext} = 50$ V ($V_{cell} = 0.78$ V) shows an increase of the junction V_j and a decrease of the current density J_{ext} (open triangles) (per unit cell area).

mAcm^{-2} (Fig. 4.11(b), open triangles) corresponding to a decrease of the overall module resistance from 34 Ωcm^2/cell to 24 Ωcm^2/cell.

The observed behavior is explained by a transient decrease of the bulk resistance R_s and an increase of the junction resistance R_j. For the voltage bias experiment, a decrease of R_s explains the increase of J_{ext}, which implies that the voltage V_j over the junction increases and as a consequence, the EL intensity increases, even without a metastable change of R_j. Note that in the present case, the effect of the series resistance resulting in a total change of the external applied voltage of 60 mV/cell is much stronger than that of recombination with a change of only 3.5 mV/cell. Furthermore, the present experimental results are consistent with additional light soaking experiments resulting in an increase of the open circuit voltage by only some mV during light exposure. The EL emission after light soaking was enhanced in a similar way as after application of electrical bias.

The enhancement of the EL emission is represented by the external EL quantum efficiency Q_{LED}, i.e. the ratio ϕ_{el}/J based on Eq. (4.7). Note that J corresponds to the externally measured current densities and the injection current density J_{ext} if the bias experiment is carried out at a constant applied voltage and a constant injection current density, respectively. Figure 4.12 depicts the improvement of $Q_{\mathrm{LED}} \approx 12\%$ during 195 s measurement time by a constant current density of $J_{\mathrm{ext}} = 34$ mAcm^{-2} (filled circles) and by a constant voltage of $V_{\mathrm{ext}} = 50$ V $Q_{\mathrm{LED}} \approx 16\%$ (open circles).

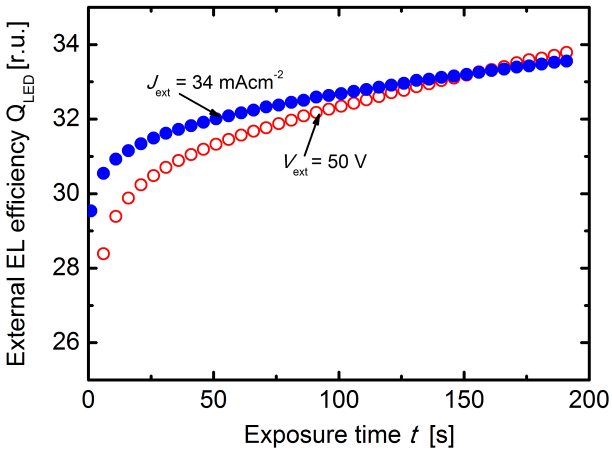

Figure 4.12.: External EL quantum efficiency Q_{LED} calculated from the ratio ϕ_{el}/J based on Eq. (4.7).

To explore the improvement of the EL emission and the external EL quantum efficiency during the bias experiment, the consequences of the transient behavior on the quantitative evaluation of the EL images is investigated. Figure 4.13(a) shows the junction voltage $V_{\mathrm{j}}(x)$ across the width of a single cell obtained by averaging the local junction voltage V_{j} along the length of the cell for the first (after 5 s) and the last (after 195 s) EL images under a constant current density $J = 34$ mAcm^{-2}. The comparison of the two curves shows that not only the average value, but also the shape of the curve changes considerably. Especially, the difference $V_{\mathrm{w0}} = V_{\mathrm{j}}(w) - V_{\mathrm{j}}(0)$ increases from 13 mV to 17 mV during the time of 195 s being more than the change

$\Delta V_{\mathrm{av}}(t) = \Delta V_{\mathrm{av}}(t) - \Delta V_{\mathrm{aw}}(0)$ of the average junction voltage (cf. Fig. 4.13(b)). This finding has an important consequence on the evaluation of EL images. From Eq. (4.13) it follows that

$$V_{\mathrm{w0}} = J R_{\mathrm{f}} \frac{w^2}{2} \frac{r_{\mathrm{j}}}{r}. \tag{4.16}$$

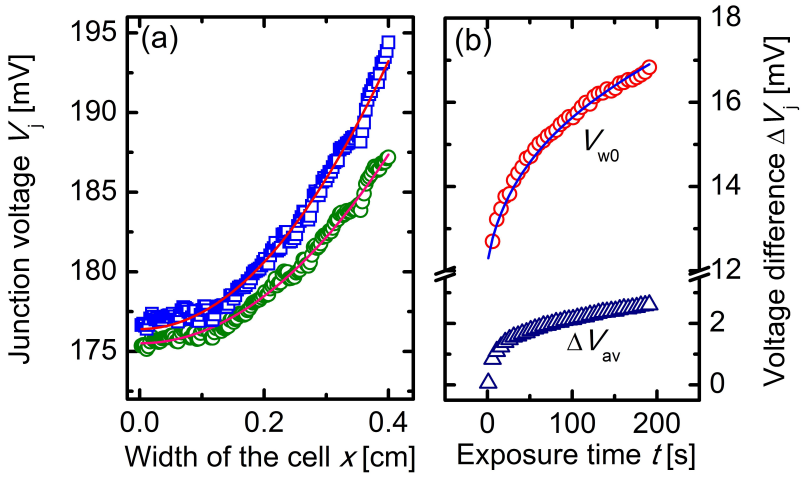

Figure 4.13.: Quasi-linescan (symbols) obtained by averaging the detected voltage V_{j} along the length of the cell plotted vs. the width of a single cell for the first (5 s) (open circles) and the last (195 s) (open squares) image of the electrical bias experiment under constant current bias ($J = 34$ mAcm^{-2}). Solid lines correspond to quadratic fits according to Eq. (4.14). (b) Time evolution of the difference $V_{\mathrm{w0}} = V_{\mathrm{j}}(w) - V_{\mathrm{j}}(0)$ (open circles) and the average voltage $\Delta V_{\mathrm{av}}(t) = \Delta V_{\mathrm{av}}(t) - \Delta V_{\mathrm{aw}}(0)$ (open triangles) during application of electrical bias. The solid line shows that a transient of V_{w0} can be predicted with the help of Eq. (4.17) from the time evolution of the external voltage $V_{\mathrm{ext}} = 50$V shown in Fig. 4.8(b).

Neglecting the series resistance in Eq. (4.16) ($r = r_{\mathrm{j}}$) would lead to a misleading interpretation concerning the ZnO sheet resistance R_{f} being directly determined by V_{w0} because the current density J_{ext} and the width w of the cell are known. In the

present case, different values of R_j are found at different times of bias experiment. In fact, the transient V_{w0} is described by the change of the series resistance during the measurement. From Eqs. (4.14) and (4.15) we obtained

$$V_{w0}(t) = JR_f \frac{w^2}{2} \frac{r_j}{r_0 + \Delta r(t)} = R_f \frac{w^2}{2} \frac{n_{id} kT/q}{r_0 + \Delta V_{cell}(t)/J}. \tag{4.17}$$

where r_0 is the initial differential resistance. Because of $\Delta r = \Delta V_{cell}/J$, the transient of V_{w0} can be directly related to that of the simultaneously recorded transient ΔV_{cell} of the external voltage shown in Fig. 4.11(b). The solid line in Fig. 4.13(b) shows the values for V_{w0} calculated with the help of Eq. (4.17) using $r_0 = 5.5\ \Omega\text{cm}^2/\text{cell}$ and $R_f n_{id} kT w^2/2q = 66\ \text{V}\Omega\text{cm}^2$. Unfortunately, this approach does not allow us to determine R_f and n_{id} independently. A combination of reasonable numbers $R_f = 21\ \Omega_{sq}$ and $n_{id} = 1.5$ would satisfy the fitting. However, the good quality of the fit which connects experimental values determined from details of the EL measurement with the externally measured voltage transient shows the self-consistency of the explanation for the observed transient behavior.

The present section investigates the metastable effects in CIGS solar modules by using time resolved measurement of the external voltage and simultaneously recording EL images. By combining these two measurements, the metastable effects on the resistivity and on the recombinatoric properties of the solar modules are distinguished from each other. Both relaxation phenomena increase the radiative, as well as the photovoltaic efficiency of the device under operation. Furthermore, the results show that the quantitative evaluation of EL images is strongly affected by the metastable transients in CIGS modules because of the influence of the bulk resistance on the EL emission. Nevertheless, even details of the EL measurement are self-consistently explained.

4.5. Summary

In this chapter, the spectrally and spatially resolved EL measurements are quantitatively analyzed for the case of industrially produced CIGS solar cells and modules. The resulting findings from these analyses are listed below:

- The reciprocity theorem is validated with the help of the luminescence spectroscopy measurements. The results from this validation are:

1. The relation between EL emission and photovoltaic quantum efficiency is valid.
2. The EL and EM intensities are unaltered under different bias conditions and unaffected from LS experiment.
3. The radiative ideality factor is close to unity.
4. EL and EM superimpose linearly only in a limited range of the applied forward bias or illumination. This range depends on LS history of the sample $J \leq 4\text{mAcm}^{-2}$ before LS and $J \leq 15\text{mAcm}^{-2}$ after LS.

- The external EL quantum efficiency Q_{LED} increases 300% (after LS), 16% (after bias experiment by constant current density J_{ext}), and 12% (after bias experiment by constant applied voltage V_{ext}). The improvement of Q_{LED} after LS is consistent with the reduction of the amount of non-radiative recombination due to the reduction of the non-radiative ideality factor after LS. The enhancement of Q_{LED} after bias experiment results from the reduction of the bulk series resistance and an increase of the junction resistance.

- The spectrally and spatially EL measurements do not sufficiently explain the origin of metastable changes in CIGS solar devices. Nevertheless, both spectrally and spatially EL provide a consistent picture of the observable metastable effects. The discrepancy between EL and EM emission may point to the origin of the metastabilities and their consequences on the performance of the devices.

- Luminescence is also a powerful tool for the investigation of recombination processes and the effects of resistances and metastable behavior on the CIGS devices.

5. Analysis of shunts with a network simulation method

Defects (shunts) in Cu(In,Ga)Se_2 (CIGS) based solar modules significantly affect the module efficiencies. The combination of electroluminescence (EL) and dark lock-in thermography (DLIT) imaging techniques represents a useful tool for the investigation of such defects. This chapter presents a detailed study on shunts in CIGS modules. With the help of a simulation tool based on the network simulation method (NSM) using a variable, adaptive mesh [45], the effect of the sheet resistances of the front and back electrodes with regard to the presence of shunts on the cell performance is qualitatively analyzed.

5.1. Introduction

Shunts are defects, which cause a locally increased dark forward current flow. Such defects can lead to a reduced V_{oc} and FF. Recently, investigation of shunts in silicon solar cells has been carried out using EL, PL and LIT [95, 127–132]. For CIGS solar cells, shunts are also qualitatively analyzed using EL, PL, and LIT [133, 134]. All of the works mentioned above either used EL, PL, LIT separately or compared them to each other to gain more information about shunts and their effect on the devices. EL and DLIT images are not only in a good agreement but also complement one another. For instance, DLIT is appropriate for localizing shunts, whilst EL is suitable for detecting potential variations around the shunts. A method is demonstrated in this work, which combines both EL and DLIT to analyze shunts and their effect on CIGS solar cells and modules. In this chapter, an EL image of a CIGS solar module consisted of several in series connected cell stripes is presented, which shows a cross-talk effect occurred in the adjacent cells of a shunted cell. Therefore, to understand

the cross-talk effect of a defect, it is important to know how the neighboring cells are involved. For this reasons, the observed cross-talk is investigated by modeling several cells including a shunted cell, using finite sheet resistances for both back and front electrodes to analyze the electrical interaction between the cells. This chapter is organized as follows.

Firstly, a simulation model using network simulation method and SPICE is introduced. Secondly, the results of EL and DLIT measurements are presented. Thirdly, different simulations for the investigation of the cross-talk effect are shown. Finally, from the simulation results, the influencing factors of the cross-talk effect are discussed Sec. 5.5.

5.2. Network simulation method and SPICE

This section gives a brief description of the spatial modeling of thin-film solar modules using the network simulation method (NSM) and simulation program with an integrated circuit emphasis (SPICE) which was presented in Ref. [45]. Local defects, e.g. shunts are small features in the module, therefore, to quantitatively analyze the shunts, a high spatial resolution is required. To monitor the entire large-area module with a good resolution leads to excessive computation times. Moreover, the calculation time is quadratically proportional to the number of nodes [45]. Using a variable, adaptive mesh which is adapted to the local geometry and the electrical field, a high spatial resolution is obtained where needed, whilst keeping the total number of nodes to a minimum. The advantage of this method is to allows accurate simulation within a reasonable amount of time.

In this work, several series connected cell stripes, which include defects (shunts) are simulated using the NSM and SPICE. Before starting with the implementation of the NSM and SPICE, the boundary value problem for these series connected cells is introduced. First of all, for simplicity, the boundary value problem is considered for a single cell with a resistive front contact and a perfect back contact.

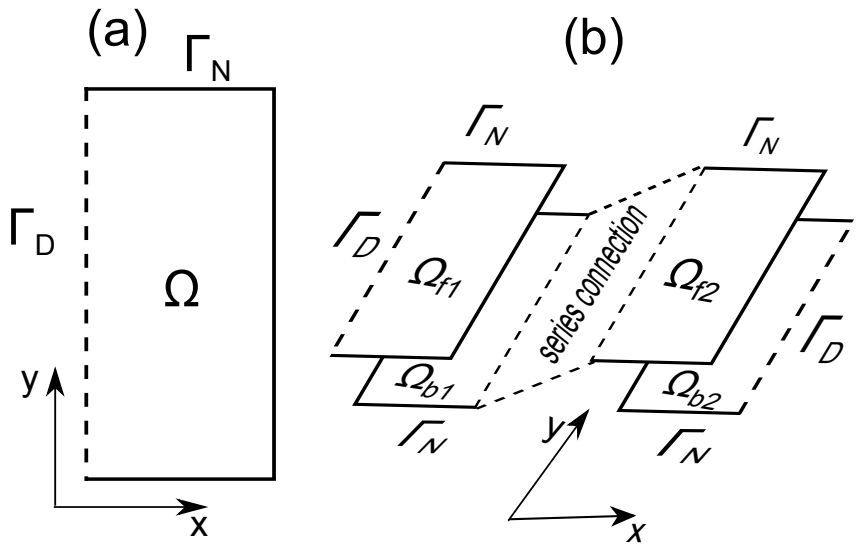

Figure 5.1.: The boundary value problem for single cell with a resistive front contact and an ideal back contact (a), and several series connected cells with non-ideal front and back contacts (b) illustrated after Ref. [45].

Figure 5.1(a) shows the boundary value problem for a single cell with a sheet resistance R_{sq} of the front contact and an ideal back contact. The boundary of the domain Ω consists of the Dirichlet and Neumann boundaries, which are denoted as Γ_{D} and Γ_{N}, respectively. On the Dirichlet boundary, the potential is fixed to V_0, whereas on the Neumann boundary the current flux out of the domain is zero or $\partial_{\mathrm{v}} V = 0$. At every position within the front electrode, current flows out or into the front electrode through the solar cell, resulting a spatial distribution of sources of current in the front electrode. The potential in an electrode in the presence of a distributed source of current, i.e. the solar cell can be described by Poisson's equation. The boundary value problem for a single cell with an ideal back contact therefore can be written as

$$\frac{d^2V(x,y)}{dx^2} + \frac{d^2V(x,y)}{dy^2} = R_{\mathrm{sq}}(x,y)J_{\mathrm{D}}(x,y,V) \qquad \text{in } \Omega_{\mathrm{D}} \qquad (5.1)$$

$$V = V_0 \qquad \text{on } T_{\mathrm{D}} \qquad (5.2)$$

$$\partial_{\mathrm{v}} V = 0 \qquad \text{on } T_{\mathrm{N}}, \qquad (5.3)$$

where V is the voltage difference between the front and back contact, J_{c} is the current density through the cell, and $E(x,y) = R_{\mathrm{sq}}J(x,y)$ is the electrical field.

More realistic is the case when the sheet resistances of both the front and back contacts are finite. The boundary value problem for a solar cell with finite sheet resistances can be written as

$$\frac{d^2V_{\mathrm{f}}(x,y)}{dx^2} + \frac{d^2V_{\mathrm{f}}(x,y)}{dy^2} = R_{\mathrm{f}}(x,y)J_{\mathrm{D}}(x,y,V) \qquad \text{in } \Omega_{\mathrm{D}} \qquad (5.4)$$

$$\frac{d^2V_{\mathrm{b}}(x,y)}{dx^2} + \frac{d^2V_{\mathrm{b}}(x,y)}{dy^2} = -R_{\mathrm{b}}(x,y)J_{\mathrm{D}}(x,y,V) \qquad \text{in } \Omega_{\mathrm{D}} \qquad (5.5)$$

$$V = V_0 \qquad \text{on } T_{\mathrm{D}} \qquad (5.6)$$

$$\partial_{\mathrm{v}} V = 0 \qquad \text{on } T_{\mathrm{N}}, \qquad (5.7)$$

where the index f and b denote the front and back electrode, respectively. Equations (5.4) and (5.5) describe two coupled Poisson's equations, one for the front and one for the back contact, respectively. The coupling is due to the spatially distributed current density $J_{\mathrm{D}}(x,y,V)$ through the solar cell, which in turn depends (non-linearly) on the voltage difference between the two electrodes.

A real solar module consists of cells, which are connected to each other in series, where the back contact of one cell is connected to the front contact of other cell. Additionally, both the front and the back contacts of the cell are non-ideal conductors, which means that the potential along the contact between two inhomogeneous cells varies. This means that the properties of one cell can have effects on neighboring cells. For that reason, modeling of several series connected cells is important to check the influence of one cell on its neighboring cells. Figure 5.1(b) shows the boundary value problem of two series connected cells with non-ideal front and back contacts. The domains of the first cell are Ω_{f1} and Ω_{b1} of the front and back contact, respectively, and of the second cell, Ω_{f2} and Ω_{b2} of the front and back contact, respectively.

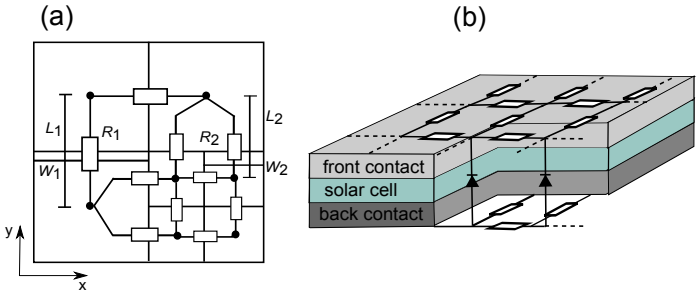

Figure 5.2.: (a) The modeling of an electrode with a variable mesh with sub-grids. The resistance of a resistor depends on its length L and its width W. In this figure, the length and the width of two resistors R_1 and R_2 are L_1, W_1 and L_2, W_2, respectively. (b) The circuit used to model the thin-film module with the help of NSM. The schematic illustrations are drawn after Ref. [45].

The network simulation method solves differential equations with a circuit equivalent. In this work, the NSM is used to solve two coupled Poisson's equations mentioned above. The coupled Poisson's equations are solved by the implementation of the NSM with a variable mesh. The front and back electrodes of a solar cell are modeled with a rectangular mesh. Figure 5.2(a) illustrates the modeling of an electrode with a rectangular variable mesh with sub-grids, i.e. each mesh cell is represented by a node which is connected with the resistance of the neighboring nodes. The resistance values R_1 and R_2 shown in Fig. 5.2(a) depend on their lengths L_1, L_2 and widths W_1, W_2, respectively, i.e. $R_1 = \frac{L_1}{W_1} R_{\mathrm{sq}}$ and $R_2 = \frac{L_2}{W_2} R_{\mathrm{sq}}$. The length L is the distance between two nodes in y-direction, whereas the width W is the distance between two nodes in x-direction. Note that for resistor which connects two nodes of different sizes, the width is defined by the node with the smallest width. Figure. 5.2(b) shows a schematic illustration a circuit of a solar cell, which is used to model a module with the NSM. Note that the diode in the schematic includes series and shunt resistances and photocurrents.

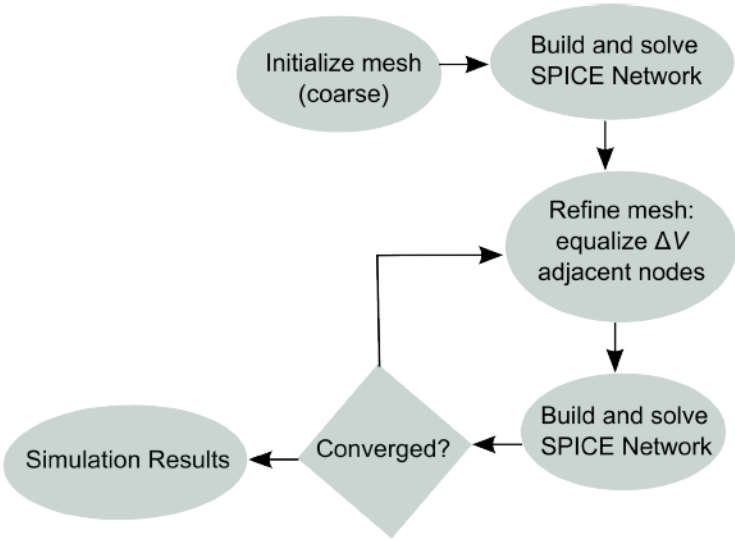

Figure 5.3.: Procedure of the SPICE simulation with a variable adaptive mesh.

For the computation of the local voltage, an initial mesh is generated from which an initial SPICE circuit is built. The simulation procedure is illustrated in Fig. 5.3. After solving the network with SPICE, the differences in junction voltage in x- or in y-direction between the adjacent nodes are computed. The adjacent nodes with the largest difference in junction voltage are chosen for splitting into smaller nodes. After refining the mesh, the SPICE network is built and solved again. The procedure is repeated until the result is converged.

The input parameters for the simulation are the diode ideality factor n_{id}, the saturation current density J_0, the injection current density J, and the geometry of the shunt (contour). Furthermore, the series resistance R_{s} of the bulk, the sheet resistances of the front and back electrodes, the shunt resistance are fit parameters, which are given in more detail in Sec.5.4. The diode ideality factor n_{id} and J_0 can be determined from the $J_{\mathrm{sc}}/V_{\mathrm{oc}}$ characteristic or from the $J/V_{\mathrm{j,ex}}$ characteristic reconstructed from the EL measurements at various injection current densities $J = J_{\mathrm{sc}}$. Here, $V_{\mathrm{j,ex}}$ is the experimental junction voltage, which is directly calculated from the local EL intensity according to Eq. (2.29). The diode ideality factor n_{id} and J_0

are given by

$$n_{\mathrm{id}} = \frac{q}{kT}\left(\frac{dV_{\mathrm{j,ex}}}{dJ}\right) J \tag{5.8}$$

$$J_0 = J/\exp\left(\frac{qV_{\mathrm{j,ex}}}{n_{\mathrm{id}}kT}\right). \tag{5.9}$$

The values n_{id} and J_0 for the module being investigated are $n_{\mathrm{id}} = 1.57$ and $J_0 = 2.36 \times 10^{-8}\mathrm{mAcm}^2$.

In order to determine the other important input parameter for the simulation, namely the contour of the shunt, a DLIT image is used because the contour of the shunt obviously appears in DLIT, whereas in EL image the contour is not visible. Note that spatial variations caused by the shunt are defined using its contour.

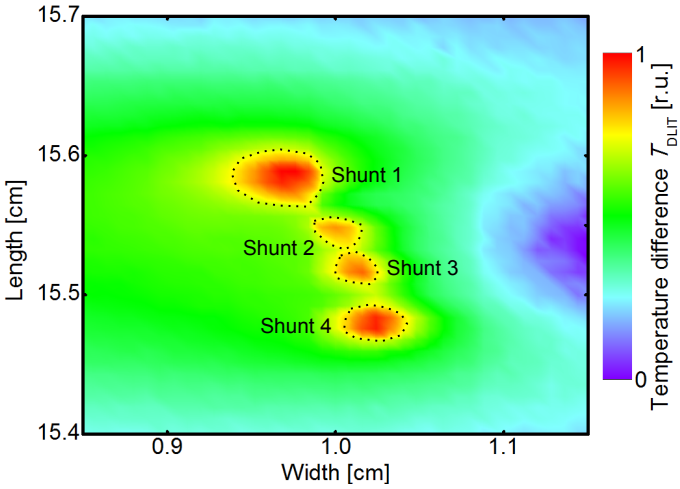

Figure 5.4.: Closed up DLIT image for the determination of the contours of the shunts for the simulation. This closed up DLIT image was measured by a micro-objective with a high resolution of 10 µm per pixel at $f_{\text{lock-in}} = 10$ Hz and 30 minutes measured time.

Figure 5.4 shows a DLIT image measured by a micro-objective with a high resolution of 10 µm per pixel at $f_{\text{lock-in}} = 10$ Hz and 30 minutes measured time. This

DLIT image displays four shunts (shunt1, shunt2 shunt3, shunt4) with different contours and areas. In order to get the geometry data of the shunts, a digitizing software (GetData Graph Digitizer) [135] is used to extract the x, y data pairs along each contour.

The simulation calculates the voltages across the back and front electrodes, from which the junction voltage $V_{\mathrm{j,sim}}$ is determined. The local EL of the front and back electrodes is also monitored, and thereby, the local power densities of the front and back electrodes can be calculated as given in Eqs. (5.11) and (5.12), respectively. The simulated local power density $P_{\mathrm{el,sim}}$ is the sum of the power densities P_{f} , P_{b} emitted at the front and the back contacts as well as the power densities P_{j} , P_{sh}, and P_{Rs} over the junction, the shunts and the bulk series resistance R_{s}

$$P_{\mathrm{el,sim}} = P_{\mathrm{f}} + P_{\mathrm{b}} + P_{\mathrm{j}} + P_{\mathrm{sh}} + P_{\mathrm{Rs}} \tag{5.10}$$

Here, P_{f} is calculated from the electrical field $|E_{\mathrm{f}}|$ of the front ZnO contact.

$$P_{\mathrm{f}} = \frac{|E_{\mathrm{f}}|^2}{R_{\mathrm{ZnO}}}, \tag{5.11}$$

and the power density P_{b} is determined by the electrical field $|E_{\mathrm{b}}|$ of the back Mo contact

$$P_{\mathrm{b}} = \frac{|E_{\mathrm{b}}|^2}{R_{\mathrm{Mo}}}. \tag{5.12}$$

The power density over the junction P_{j} follows the relation

$$P_{\mathrm{j}} = J_0 V_{\mathrm{j,sim}} \left[\exp\left(\frac{q V_{\mathrm{j,sim}}}{n_{\mathrm{id}} kT} \right) - 1 \right]. \tag{5.13}$$

The power density over the shunt P_{sh} is given by

$$P_{\mathrm{sh}} = \frac{(V_{\mathrm{j,sim}})^2}{R_{\mathrm{sh}}}, \tag{5.14}$$

where V_{Rs} is the voltage drop over R_{s} and R_{sh} is the shunt resistance.

The power density P_{Rs} can be calculated by

$$P_{\mathrm{Rs}} = \frac{(V_{\mathrm{Rs}})^2}{R_{\mathrm{s}}}. \tag{5.15}$$

From DLIT measurement, the local temperature difference T_{DLIT} can be determined instead of the absolute local power P_{DLIT}. However, the relation between the local temperature difference T_{DLIT} and P_{DLIT} is given by

$$T_{\mathrm{DLIT}} = \frac{2P_{\mathrm{DLIT}}}{\pi\sqrt{\pi} D \lambda}, \tag{5.16}$$

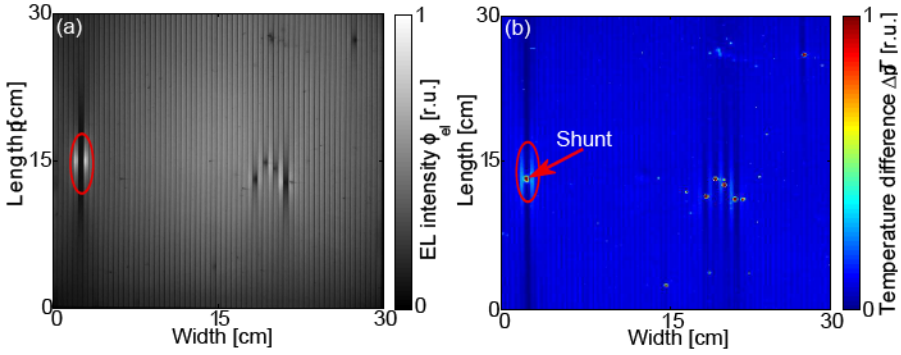

Figure 5.5.: (a) EL image of a CIGS module (30×30 cm^2) consisting of 64 cells, recorded by a Si-CCD camera at $J = 8.3$ mAcm^{-2} and 2 s exposure time. (b) 0° signal amplitude DLIT image of the same module measured at the same injection current with a lock-in frequency of $f_{\text{lock-in}} = 10$ Hz. The red ellipse marks the shunt which was investigated.

for thermally thick samples [27]. Here, D is the pixel width (referring to the sample surface) and λ is the heat conductivity. These two parameters are constant, so that T_{DLIT} is directly proportional to P_{DLIT}. Therefore, combining EL and DLIT techniques means that the local simulated power from EL measurements $P_{\text{el,sim}}$ is directly comparable to the local temperature difference T_{DLIT}.

5.3. Experimental results

This section describes the experimental results obtained from the EL and DLIT measurements of a (30×30 cm^2) CIGS module, which contains several shunted cells. The CIGS module consists of 64 individual cells (cell length $l = 30$ cm and width $w = 0.4$ cm). Detailed information on the sample is given in Sect. 2.3.1.

Figure 5.5 shows the results of the EL (a) and DLIT (b) measurements. The EL measurement was carried out at an injection current density of $J = 8.3$ mAcm^{-2}, corresponding to an injection current of $I = 0.1$ A by a Si-CCD camera using pixel binning (3×3 pixels) with an exposure time of 2 s. The EL image illustrates that

the module performance is affected by several shunted cell stripes. The scale of the EL image exhibits the local EL intensity in arbitrary units. The EL intensity in the shunted regions is very low. The marked region in Fig. 5.5(a) displays a shunted cell, which heavily affects the adjacent cell stripes, i.e. the EL intensity of the left and right non-shunted neighboring cells is noticeably high. In this thesis, this effect is named a cross-talk effect, which will be described in more detail later on.

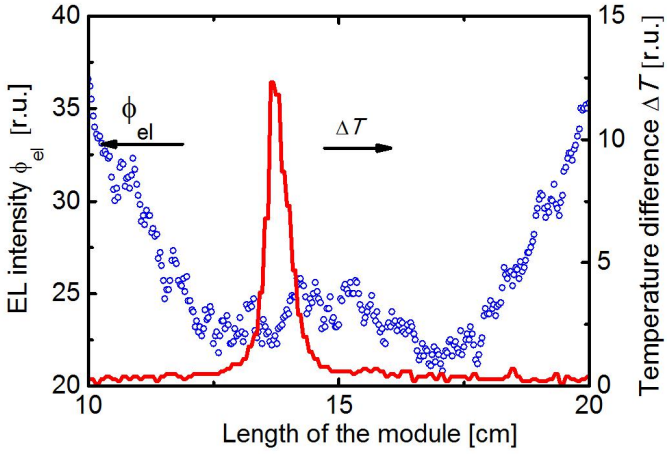

Figure 5.6.: Line-scans of EL intensity and of temperature difference resulting from averaging the EL intensity and the temperature difference over the entire width of the marked shunted cell shown in Fig. 5.5.

The DLIT image was recorded at the same injection current density of $J = 8.3$ mAcm^{-2} and at a lock-in frequency of $f_{\text{lock-in}} = 10$ Hz. The DLIT measurement was done for ≈ 30 minutes. The scale of the DLIT image displays the relative local temperature in arbitrary units. The defects appear as bright spots in the DLIT image. A qualitative comparison between the EL and the DLIT images shows that all the defects visible as dark regions in the EL image appear as bright spots in the DLIT image. The line-scans of the EL intensity (open circles) and of the temperature difference (solid curve) obtained from averaging the local EL intensity and the local

temperature difference, respectively, over the entire width of the marked shunted cell show a consistency with the result from the comparison. Note that to highlight the effect of the marked shunt on the EL intensity and the temperature difference, only a part of the line-scans close to the shunt (from $l = 10$ to 20 cm) are shown (Fig. 5.6). The EL line-scan exhibits a broader EL intensity dip at the shunt due to the low EL intensity, whereas the DLIT line-scan has a narrow form and a sharp peak at the shunt because of a high temperature difference. Moreover, it is also obvious that DLIT imaging is more feasible for the determination of the location and the geometry of shunts than EL imaging.

As mentioned in Sec.5.2, a DLIT image is used to determine the contour of the shunt, which is the input parameter for the simulation. For this reason, it is important to have a good spatial resolution. For thermally thick samples, i.e. its thickness is large with respect to the thermal diffusion length, the halo around local heat sources, which is proportional to the thermal diffusion, reduces with $1/\sqrt{f_{\text{lock-in}}}$ [27]. Therefore, for a good spatial resolution of a local heat source, a high lock-in frequency should be chosen. Note that the higher the lock-in frequency, the poorer the signal to noise ratio, hence a lock-in frequency should be high enough to gain a good resolution and low enough to have a proper signal to noise ratio. The choice of a proper lock-in frequency depends on the aims of different analysis. In this work, it is important to have a high resolution DLIT image in order to determine the position of the shunts precisely, therefore, a lock-in frequency of 10 Hz has been chosen.

Figure 5.7 illustrates the line-scans of the temperature difference by averaging the entire width of the respective DLIT images measured at different frequencies $f_{\text{lock-in}} = [0.1, 0.3, 0.5, 0.7, 1, 3, 5, 7, 10]$ Hz. The graphs show that the higher the lock-in frequency, the narrower the full width half maximum (FWHM) or the better is the spatial resolution of local heat source (shunt).

For further investigation of the defect and the correlation between these two camera-based methods, EL and DLIT images of a small area (1×2 cm^2) around the marked shunt were recorded. This area extends over 5 cells ($l = 1$ cm and $w = 0.4$ cm). The middle cell stripe is shunted. Electroluminescence measurements were carried out by a Si-CCD camera with a pixel binning (1×1 pixels) for high resolution images and a lens tube between the camera and the objective enabling a

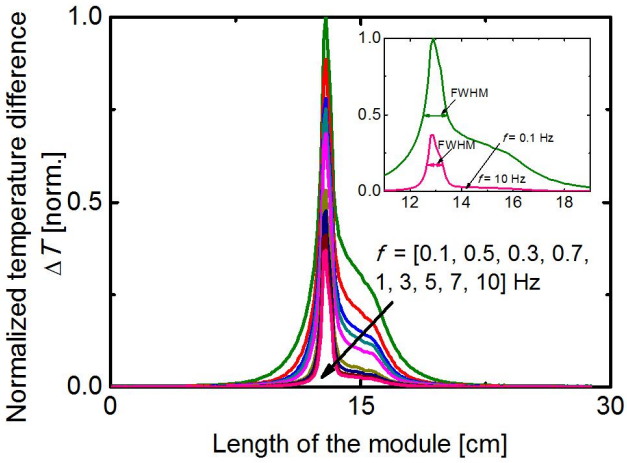

Figure 5.7.: Line-scans of the temperature difference by averaging the entire width of the respective DLIT images measured at different lock-in frequencies $f_{\text{lock-in}} = [0.1, 0.3, 0.5, 0.7, 1, 3, 5, 7, 10]$ Hz. The inset is a close-up view of the line-scans of the relative local temperature at $f_{\text{lock-in}} = [0.1, 10]$ Hz with their receptive FWHM.

close-up of the regions of interest. For the DLIT measurements, a micro-objective with a high resolution of 10 µm per pixel is used for a better focus on the shunt.

Figure 5.8(a) displays a magnification of an EL image of a small area around the shunt marked in Fig. 5.5(a). This image enables a closer look at the shunt and the effect caused by this shunt. Because of the shunt, the EL intensity of the middle cell is very low due to the low local junction voltage. The shunt quenches the EL intensity [38], which makes EL unsuitable to determine the position and the shape of a defect. In contrast, it is clearly visible in this EL image that the local EL intensity of the right and left non-shunted adjacent cells is much higher than that of the shunted cell and the non-shunted cells far away from the shunt (the first and the fifth cell in the EL image counted from left to right). This shows that the shunt exhibited in this EL image strongly affects the two directly adjacent cells, and even slightly affects the further neighboring cells. The interaction between the cells

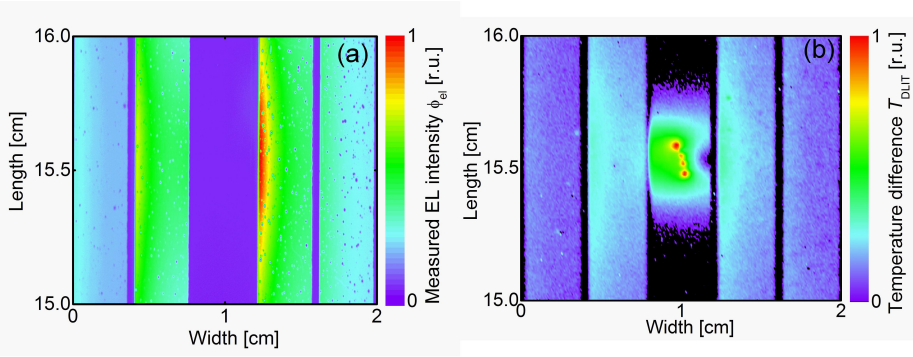

Figure 5.8.: (a) EL image of a small area (1×2 cm^2) around the shunts marked in Fig. 5.5(a). The cell width is 0.4 cm, the area expands over five cells, in which the cell in the middle is shunted. These five cells were recorded by a full frame Si-CCD camera (9.4 mega pixels) and 20 s exposure time. (b) DLIT image of the same area around the shunts shown in Fig. 5.8(a). This areas is recorded by a micro-objective with a high resolution of 10 µm per pixel at $f_{\text{lock-in}} = 10$ Hz and 30 minutes exposure time.

due to the defect in the middle cell is the so called cross-talk effect, which can be explained in more detail in Sec. 5.4.

Figure 5.8(b) illustrates a magnification of a DLIT image of the same cell stripes shown in Fig. 5.8(a). The close-up DLIT image used to determine the location of the shunt is taken with a micro-objective with a high resolution of 10 µm per pixel and $f_{\text{lock-in}} = 10$ Hz. The measured time was 30 minutes. Contrary to the EL image, the location and the geometry of the shunt are clearly observable in this close-up image, which shows that the shunt in the middle cell stripe actually consists of four shunts in close proximity with different sizes. Until now, it is assumed that the shunt to be investigated is a single shunt due to the DLIT image shown in Fig. 5.5(b). For this reason, the plural term 'shunts' is used from here on when referring to this particular shunt. With the help of this close-up DLIT image, the sizes of the shunts are extracted and used as input parameters for the SPICE model as mentioned in Sec. 5.2. The cross-talk caused by the shunt is also observable in this image because

the temperature difference of the two directly adjacent cells are slightly higher than that of the first and last cells. However, this cross-talk appears less significant than in the EL image. Furthermore, Fig. 5.8(b) also shows that the local temperature difference at the shunts has the highest value because of the high dissipated power density caused by the shunts. Besides, the values of the local temperature difference at the regions above and below the shunts are very low due to the low dissipated power in these regions.

The experimental results presented in this section show that the EL and DLIT images are in a good agreement and these two methods complement each other. Therefore, combining EL and DLIT imaging provides a qualitative analysis of such defect in CIGS devices. In the following section, a detailed investigation of the cross-talk is demonstrated using these measurement results and the simulation results.

5.4. Simulation results

As mentioned in Sec. 5.3, a cross-talk is clearly observed in measured EL image. This section presents a description of the cross-talk with the help of the simulation results considering the influencing factors such as shunts and resistances of the front and back electrodes on the cross-talk. First of all, the cross-talk can be explained as follows.

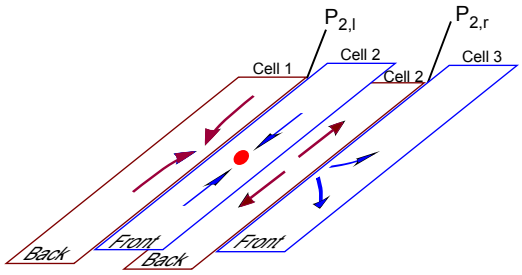

Figure 5.9.: A 2D schematic of a series interconnection of the front and back electrodes of different cells.

Figure 5.9 illustrates a 2D schematic of a series interconnection of the front

and back electrodes of different cells, where the middle cell is shunted. The back electrode of cell 1 is connected with the front electrode of cell 2 through the left $P_{2,l}$ scribing line and the back electrode of cell 2 is coupled with the font electrode of cell 3 through the right $P_{2,r}$ scribing line. The concentration of current toward the area around the shunts leads to potential variations in the front and back electrodes along the length direction of the shunted cell stripe. This leads to non-equipotential contacts to the neighboring cells, i.e. $P_{2,l}$ and $P_{2,r}$, and thus, the defect also affects the neighboring cells. Due to the non-equipotential contacts to the neighboring cells, the current densities increase in the parts of the neighboring cells in the direct vicinity of the defect. The cross-talk observed between the cells is thus the result of currents through the electrodes along the length direction of the cells, which cause the potential variations in the $P_{2,l}$ and $P_{2,r}$ scribing lines. Therefore, the potential difference in $P_{2,l}$ and $P_{2,r}$ is a measure of the cross-talk.

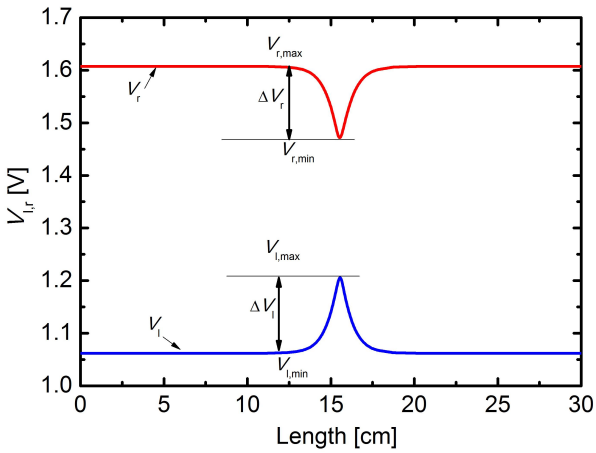

Figure 5.10.: Voltage line-scans V_l, V_r at $P_{2,l}$ and $P_{2,r}$, respectively. Voltage differences ΔV_l and ΔV_r are defined as a measure for the cross-talk.

In order to calculate the potential difference, the voltage line-scans V_l, V_r over the entire length of the module are chosen in the $P_{2,l}$ and $P_{2,r}$ lines, respectively.

Note that the voltage line-scans V_{l} and V_{r} correspond to the voltage line-scans of the front electrode V_{f} and the back electrode V_{b}. The potential difference ΔV_{l} and ΔV_{r} are given by

$$\Delta V_{\mathrm{l}} = V_{\mathrm{max,l}} - V_{\mathrm{min,l}} \tag{5.17}$$

$$\Delta V_{\mathrm{r}} = V_{\mathrm{max,r}} - V_{\mathrm{min,r}}, \tag{5.18}$$

which are illustrated in Fig. 5.10.

The potential variations along length direction that these currents induced should depend on the magnitude of the currents and the sheet resistances of the electrodes. In order to explore the effects of the shunts and the electrode sheet resistances, a simulation model using the NSM and SPICE presented in Sec. 5.2 was used to simulate the distribution of the local EL intensity, the junction voltage and the local power densities from the measured EL image shown in Fig. 5.8(a). In the following, the validation of the NSM and SPICE is introduced with the parameterization of the shunt resistances R_{sh}, the sheet resistances R_{ZnO} and R_{Mo} of the front ZnO and the back Mo contacts, respectively. Note that following from Sec. 4.4.2, the bulk series resistance R_{s}, which is in series connected with the junction affects the measured EL intensity. Therefore, it is important to include R_{s} in the model as well. Thus, the parameter set for the simulation model includes R_{ZnO}, R_{Mo}, R_{sh} and R_{s}. The parameterization is divided into two parts. In the first part, the values of the parameter set are obtained from either literature or manual adjustments of the simulated images to the experimental images. From these manual fits, the range of the individual parameters in the parameter set is roughly defined. As the result, a systematic adaption of the measurement and simulation results is developed in the second part to determine the optimum values for the parameter set.

The input parameters of $R_{\mathrm{ZnO}} = 18\ \Omega_{\mathrm{sq}}$ and $R_{\mathrm{Mo}} = 1.3\ \Omega_{\mathrm{sq}}$ were taken from Helbig et al. [38], where the authors neglected the effect of the bulk series resistance R_{s}. The input parameter of $R_{\mathrm{s}} = 0.02\ \Omega\mathrm{cm}^2$ stems from the qualitative comparison of the simulation results with varied R_{s} and the measured EL and DLIT images (Fig.5.8). The shunt resistances of $[R_{\mathrm{sh1}} = 0.005, R_{\mathrm{sh2}} = 0.02, R_{\mathrm{sh3}} = 0.02, R_{\mathrm{sh4}} = 0.008]\ \Omega\mathrm{cm}^2$ result from fitting the results of several simulations with different sets of $[R_{\mathrm{sh1}}...R_{\mathrm{sh4}}]$ to the measured results. The input parameters for the simulations are given in Tab.5.1. The effect of changing the individual parameters of the shunt

Table 5.1.: Input parameters for the SPICE simulation with varied shunt resistances.

Fixed parameters	Varied parameters
$n_{\mathrm{id}} = 1.57$	$R_{\mathrm{sh,high}} = [5, 2, 2, 8]$ [$\Omega\mathrm{cm}^2$]
$J_0 = 2.63 \times 10^{-8}$ [mAcm^{-2}]	$R_{\mathrm{sh,low}} = [0.00005, 0.0002, 0.0002, 0.00008]$ [$\Omega\mathrm{cm}^2$]
$J = 8.3$ [mAcm^{-2}]	$R_{\mathrm{sh,opt}} = [0.005, 0.02, 0.02, 0.008]$ [$\Omega\mathrm{cm}^2$]
$R_{\mathrm{ZnO}} = 18$ [Ω_{sq}]	
$R_{\mathrm{Mo}} = 1.3$ [Ω_{sq}]	
$R_{\mathrm{s}} = 0.02$ [$\Omega\mathrm{cm}^2$]	

resistances is discussed below.

Before discussing about the results illustrated in Fig. 5.11, a brief introduction of the resulting power density images is given here. The simulated local power density image results from the dissipated power in the electrodes, the junction, the defects and of the power density in the internal series resistance of the solar cell. In Appendix A, it is illustrated how the simulated power density image is constructed and where the individual contributions to the total power density stem from.

Figure 5.11 shows the simulated EL images (a-c) and the simulated power density images (d-f) resulting from different simulations with the input parameters given in Tab. 5.1. For each simulation presented in Fig. 5.11, the shunt resistances are changed, whereas all other input parameters are the same. For simplicity, ratios of 5/2/2/8 and 5/20/20/8 corresponding to $R_{\mathrm{sh1}}/R_{\mathrm{sh2}}/R_{\mathrm{sh3}}/R_{\mathrm{sh4}}$ are chosen after testing various simulations with different ratios.

With the shunt resistances of $R_{\mathrm{sh,high}} = [5, 2, 2, 8]$ $\Omega\mathrm{cm}^2$ both EL (a) and power density (d) images do not show good agreement with the measured images shown in Fig 5.8, which indicates that the chosen shunt resistances are too high. Due to the high shunt resistances, the current flows over the shunts $I_{\mathrm{sh}} = 0.0004$ A is low compared to the injection current $I = 0.1$ A, therefore, the voltage across the junction is unaffected by the shunts. As the consequence, the local simulated power density is only slightly higher at the shunts than at the surroundings. With the shunt resistances of $R_{\mathrm{sh,low}} = [0.00005, 0.0002, 0.0002, 0.00008]$ $\Omega\mathrm{cm}^2$, the shunts strongly affects the shunted cell and the adjacent cells, i.e. cross-talk effect occurs.

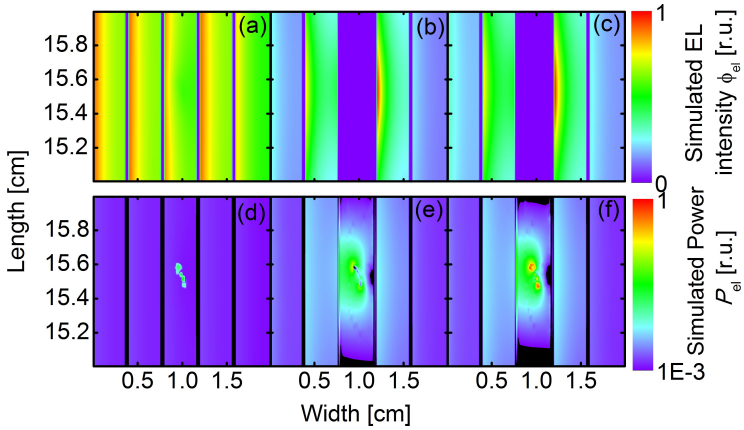

Figure 5.11.: (a-c) Simulated EL images obtained from the simulations with the input parameters given in Tab.5.1 for the cases of high, low, and optimal shunt resistances $R_{\mathrm{sh,high}} = [5, 2, 2, 8]\ \Omega\mathrm{cm}^2$, $R_{\mathrm{sh,low}} = [0.00005, 0.0002, 0.0002, 0.00008]\ \Omega\mathrm{cm}^2$, and $R_{\mathrm{sh,opt}} = [0.005, 0.02, 0.02, 0.008]\ \Omega\mathrm{cm}^2$. (d-f) Simulated power density images resulting from the same simulations mentioned in (a-c) for high, low and optimal shunt resistances.

The simulated EL image (b) shows a similarity to the measured EL image shown in Fig 5.8(a). However, the power density image (e) indicates that the values of $R_{\mathrm{sh,low}}$ are too low for the strong defect shown in the DLIT image (Fig. 5.8(b)). The EL (c) and power density images (f) for the case of $R_{\mathrm{sh,opt}} = [0.005, 0.02, 0.02, 0.008]\ \Omega\mathrm{cm}^2$ agree well with the measured images (Fig 5.8). Therefore, for all other simulations presented below, the shunt resistances of $R_{\mathrm{sh,opt}} = [0.005, 0.02, 0.02, 0.008]\ \Omega\mathrm{cm}^2$ are chosen. Note that the local dissipated power density is directly proportional to the local temperature difference as mention in chapter 5.2. Therefore, a local power density image is comparable to a temperature difference DLIT image. It is obvious from this analysis that EL is not appropriate for the determination of the shunt resistances. Despite of the two orders of magnitude difference between $R_{\mathrm{sh,low}}$ and $R_{\mathrm{sh,opt}}$, the simulated EL images are only slightly different from each other. A comparison of the simulated power density with the measured DLIT image providing more accurate values of the shunt resistances.

Table 5.2.: The input parameters for different simulations to determine the optimum values for the bulk series resistance R_s, the sheet resistances R_{ZnO} and R_{Mo} of the front and back contacts.

Fixed parameters	Varied R_s	Varied R_{Mo}	Varied R_{ZnO}
n_{id}	1.57	1.57	1.57
J_0[mAcm^{-2}]	2.63×10^{-8}	2.63×10^{-8}	2.63×10^{-8}
J[mAcm^{-2}]	8.3×10^{-8}	8.3×10^{-8}	8.3×10^{-8}
$R_{sh,opt}$ [Ωcm^2]	[5,20,20,8]×10^{-3}	[5,20,20,8]×10^{-3}	[5,20,20,8]×10^{-3}
R_s[Ωcm^2]	[0.008,0.002,0.02,0.05, 0.2,0.3,0.4,0.5,0.8,1.5,2]	0.02	0.02
R_{Mo}[Ω_{sq}]	1.3	[0:0.2:12]	1.3
R_{ZnO}[Ω_{sq}]	18	18	[0:1:40]

To find the optimum values for the other parameters such as R_s, R_{ZnO}, R_{Mo}, various simulations were done. The input parameters for different simulations are listed in Tab 5.2. There are three cases either R_s or R_{ZnO} or R_{Mo} is varied. Before introducing a method to determine the optimum values of R_s, R_{ZnO}, and R_{Mo}, the influences of the individual parameters on the simulated EL intensity will be analyzed below.

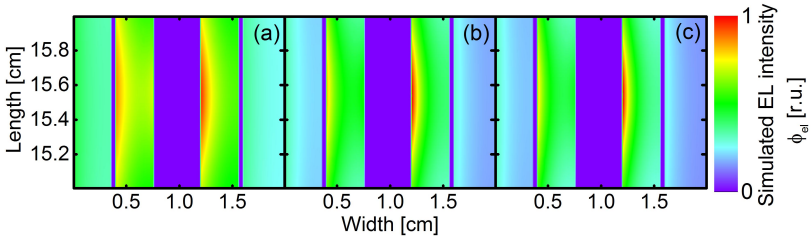

Figure 5.12.: EL images obtained from the simulations with varied R_s, where all other input parameters n_{id}, J_0, R_{ZnO},R_{Mo}, and $R_{sh,opt}$ are the same for all simulations and are given in Tab.5.2. (a) $R_s = 2$ Ωcm^2, (b) $R_s = 0.2$ Ωcm^2, (c) $R_s = 0.02$ Ωcm^2

In order to check the influence of R_s on the simulation results, different values

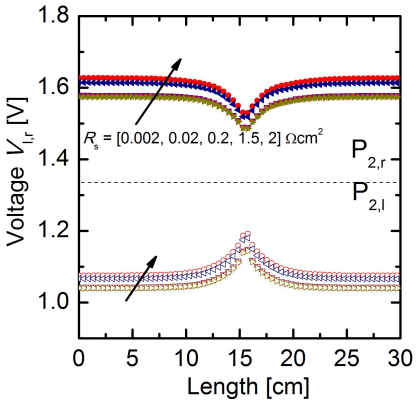

Figure 5.13.: Line-scans of the voltage along the left $P_{2,l}$ scribing line of the shunted cell (open symbols) and the right $P_{2,r}$ scribing line of the shunted cell (filled symbols) for varied values of R_s given in Tab. 5.2.

of R_s are chosen, where other input parameters are the same for different simulations with varied R_s (Tab.5.2). The values of R_s are given in Tab. 5.2. Figure 5.12 shows the EL images resulting from the simulations with varied $R_s = [2, 0.2, 0.02]$ Ωcm^2. If $R_s = 2$ Ωcm^2 (a), the simulated EL intensity is higher compared to the measured EL intensity (Fig. 5.8(a)). However, with $R_s = 0.2$ Ωcm^2 (b) and 0.02 Ωcm^2 (c), the EL images do not show a significant difference to each other and to the measured EL image in Fig. 5.8(a).

Figure 5.13 shows line-scans of the voltage along the entire length of the module for various values of R_s as listed in Tab.5.2. The voltage line-scans V_l and V_r are taken along the left $P_{2,l}$ scribing line of the shunted cell (open symbols) and the right $P_{2,r}$ scribing line of the shunted cell (filled symbols). The line-scans indicate that the voltages V_l and V_r increase with increasing R_s. However, the increase in the voltage is quite small, especially with R_s is less than one.

By varying the values of R_{ZnO} and R_{Mo}, the effect of these sheet resistances on the EL intensity can be explored. Figures 5.14(a-d) show the EL images resulting from the simulations with varied R_{ZnO} and R_{Mo}. The input parameters are given in

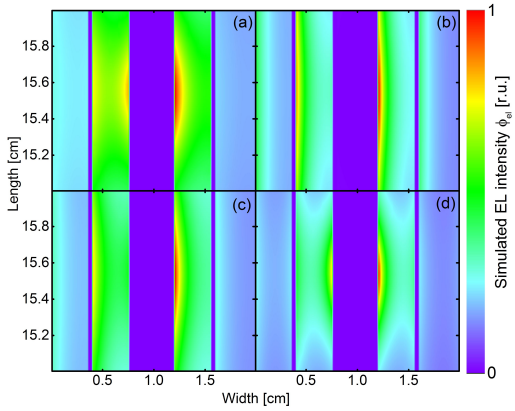

Figure 5.14.: (a) Simulated EL image with $R_{\mathrm{ZnO}} = 5\ \Omega_{\mathrm{sq}}$, $R_{\mathrm{Mo}} = 1.3\ \Omega_{\mathrm{sq}}$, (b) Simulated EL image with $R_{\mathrm{ZnO}} = 40\ \Omega_{\mathrm{sq}}$, $R_{\mathrm{Mo}} = 1.3\ \Omega_{\mathrm{sq}}$, (c) Simulated EL image with $R_{\mathrm{Mo}} = 0.4\ \Omega_{\mathrm{sq}}$, $R_{\mathrm{ZnO}} = 18\ \Omega_{\mathrm{sq}}$, (d) Simulated EL image with $R_{\mathrm{Mo}} = 12\ \Omega_{\mathrm{sq}}$, $R_{\mathrm{ZnO}} = 18\ \Omega_{\mathrm{sq}}$. The other input parameters such as n_{id}, J_0, J, R_{s}, and $R_{\mathrm{sh,opt}}$ are given in Tab.5.2.

Tab. 5.2 and $R_{\mathrm{s}} = 0.02\ \Omega\mathrm{cm}^2$. For the simulated EL image shown in Figs. 5.14(a-b), the values of R_{ZnO} are chosen as 5 Ω_{sq} and 40 Ω_{sq}, respectively, and $R_{\mathrm{Mo}} = 1.3\ \Omega_{\mathrm{sq}}$ for both simulations. With $R_{\mathrm{ZnO}} = 5\ \Omega_{\mathrm{sq}}$, the ZnO layer becomes more conductive, therefore, the current flow from the left adjacent non-shunted cells across the shunts to the right adjacent non-shunted cells is more concentrated compared to the case of the low conductive ZnO layer with $R_{\mathrm{ZnO}} = 40\ \Omega_{\mathrm{sq}}$. Therefore, the lateral distribution of the local EL intensity in Fig. 5.14(a) is larger than that shown in Fig. 5.14(b).

Analogously, Figs. 5.14(c-d) display the EL images of the simulations with varied $R_{\mathrm{Mo}} = 0.4\ \Omega_{\mathrm{sq}}$ and $R_{\mathrm{Mo}} = 12\ \Omega_{\mathrm{sq}}$, respectively, and $R_{\mathrm{ZnO}} = 18\ \Omega_{\mathrm{sq}}$ for both simulations. With $R_{\mathrm{Mo}} = 12\ \Omega_{\mathrm{sq}}$, the back Mo contact is less conductive, therefore, the lateral distribution of the local EL intensity is smaller than that shown in Fig. 5.14(c) for $R_{\mathrm{Mo}} = 0.4\ \Omega_{\mathrm{sq}}$.

In order to check the reliability of the values of the bulk series resistance R_{s} and the sheet resistances R_{ZnO} and R_{Mo} obtained from the comparison between the

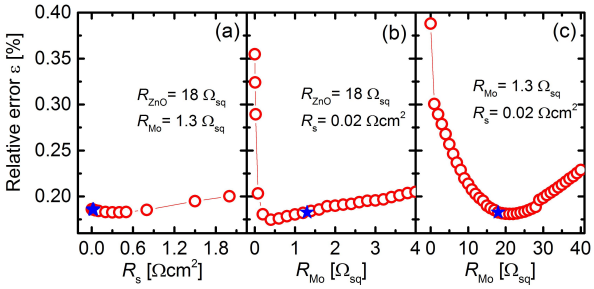

Figure 5.15.: (a) Relative global error of the simulated and measured EL images for the determination of R_s. (b) Relative global error of the simulated and measured EL images for the determination of R_{Mo}. (c) Relative global error of the simulated and measured EL images for the determination of R_{ZnO}. The parameters for all simulations mentioned here are listed in Tab. 5.2. Note that the filled stars are marked for the simulations carried out with $R_s = 0.02\ \Omega\text{cm}^2$, $R_{ZnO} = 18\ \Omega_{sq}$ and $R_{Mo} = 1.3\ \Omega_{sq}$, respectively.

measured and simulated EL images, it is important to calculate the error resulting from the model. The relative global root mean square errors ε are determined by comparing the resulting simulated EL images from various simulations mentioned below to the measured EL image as described in the following equation

$$\varepsilon = \sqrt{\phi_{ex}^2 - \phi_{sim}^2}. \tag{5.19}$$

Note, that the laser lines and part of the experimental data with strong noise are not considered in the calculation of the relative global error.

To determine the optimum value for R_s, various simulations are done with the variation of R_s. Analogously, to find the optimum values for R_{ZnO} and R_{Mo}, the simulations are carried out with varied $R_{ZnO} = [0, 1, 2, 3...40]\ \Omega_{sq}$ and $R_{Mo} = [0, 0.2, 0.4, ...12]\ \Omega_{sq}$, respectively. Note that for each simulation, only one input parameter either R_s, R_{ZnO}, or R_{Mo} is changed. Different simulations are run for different values of R_s, R_{ZnO} or R_{Mo}. The parameters for all simulations mentioned above are given in Tab. 5.2.

Figure 5.15(a) presents the relative global errors obtained from the comparisons

of the simulated EL images for varied values of R_s with the measured EL image shown in Fig. 5.8(a). The relative errors are approximately 18.5% for $R_s < 1\ \Omega\text{cm}^2$ and close to 20% for $R_s = [1.5, 2]\ \Omega\text{cm}^2$. This result is consistent with the results presented in Figs. 5.12(a-c) and Fig. 5.13. The optimum value for R_s is around 0.3 Ωcm^2, where $\varepsilon \approx 18\%$. Figure 5.15(b) shows the relative global errors of the simulated and measured EL images for the determination of R_{Mo}. The sheet resistance of the Mo layer is varied in the range of $[0,\ 0.2,\ 0.4...12]\ \Omega_{\text{sq}}$. The optimum value for R_{Mo} is around 0.4 Ω_{sq}, where the relative error is approximately 17.4%. A clear trend to define the optimum value for R_{Mo} is shown in Fig. 5.15(b). It is obvious to see that the relative global error increases when R_{Mo} gets closer to zero or becomes larger than 2 Ω_{sq}. Analogously, Fig. 5.15(c) presents the relative global error of the simulated and measured EL images for the determination of R_{ZnO}. The value of R_{ZnO} is varied in the range of $[0,\ 1,\ 2...40]\ \Omega_{\text{sq}}$. The optimum value for R_{ZnO} is around 20 Ω_{sq}, where the relative error is around 17.9%. A clear trend of the relative global error is also reached for R_{ZnO}. The filled stars in Figs. 5.15(a-c) are marked for the simulations carried out with $R_s = 0.02\ \Omega\text{cm}^2$, $R_{\text{ZnO}} = 18\ \Omega_{\text{sq}}$ and $R_{\text{Mo}} = 1.3\ \Omega_{\text{sq}}$, respectively. The clear trends in Figs. 5.15(b-c) show that the method presented here is appropriate to determine R_{Mo} and R_{ZnO}. As shown in Fig. 5.15(b-c), R_{Mo} should be in the range of $0.1\ \Omega_{\text{sq}} \leq R_{\text{Mo}} \leq 2\ \Omega_{\text{sq}}$ and R_{ZnO} should be in the range of $16\ \Omega_{\text{sq}} \leq R_{\text{ZnO}} \leq 26\ \Omega_{\text{sq}}$. However, the trend shown in Fig. 5.15(a) is not very clear to find an optimum value for R_s, which indicates that this method is not very appropriate to determine R_s precisely.

Finally, Figs. 5.16(a-b) present the simulated EL and power density images with $R_s = 0.02\ \Omega\text{cm}^2$, $R_{\text{ZnO}} = 18\ \Omega_{\text{sq}}$ and $R_{\text{Mo}} = 1.3\ \Omega_{\text{sq}}$. Both the simulated EL and the simulated power density images show good agreement with the measured EL and the measured DLIT images shown in Fig. 5.8(a-b). This result indicates that the NSM and SPICE is a good tool to reproduce the experimental results and to determine the sheet resistances of the front and the back contacts. The simulation model is also feasible to estimate the range of the shunt resistances R_{sh} and the bulk series resistance R_s. The cross-talk effects cause by the shunts and the finite sheet resistances can be analyzed with this simulation model as well. Detailed analysis of the cross-talk effects will be given in Sec. 5.5.

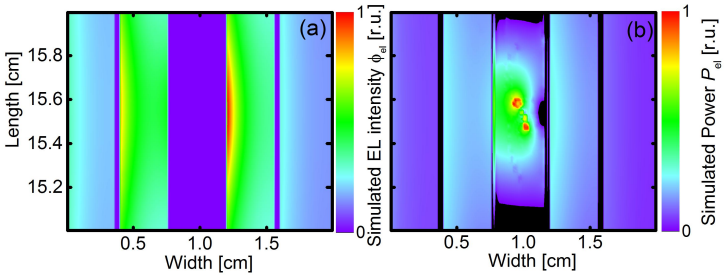

Figure 5.16.: (a) Simulated EL image with the parameters listed in Tab. 5.2, where $R_s = 0.02\ \Omega\text{cm}^2$, $R_{ZnO} = 18\ \Omega_{sq}$ and $R_{Mo} = 1.3\ \Omega_{sq}$. (b) Simulation power density image with the same parameters as used in (a).

5.5. Discussion

In this section, the cross-talk effects are further analyzed. Particularly, this section also discusses on the influences of the shunts and the sheet resistances on the cross-talk effects. Before presenting the systematic analysis of the cross-talk effects, several simulation results from a gedankenexperiment of changing the values of the sheet resistances are discussed below.

The gedankenexperiment is based on the fact that the cross-talk originates from the currents in the front and back contact, which flow along the length direction of the cells and result in the non-equipotential lines $P_{2,l}$ and $P_{2,r}$ scribing lines. The cross-talk will disappear if $P_{2,l}$ or/and $P_{2,r}$ are equipotential lines, which will occur if at least one of the sheet resistances equals zero. Three simulations are carried out for three cases, i.e. $R_{ZnO} = 0\ \Omega_{sq}$ with $R_{Mo} = 1.3\ \Omega_{sq}$, $R_{Mo} = 0\ \Omega_{sq}$ with $R_{ZnO} = 18\ \Omega_{sq}$, and $R_{ZnO} = R_{Mo} = 18\ \Omega_{sq}$. All other parameters for the simulations are given in Tab. 5.2 and $R_s = 0.02\ \Omega\text{cm}^2$.

The resulting simulated EL images for these three cases are displayed in Fig. 5.17. In both EL images (a-b) with $R_{ZnO} = 0\ \Omega_{sq}$ and $R_{Mo} = 0\ \Omega_{sq}$, no cross-talk is observed. In contrast, Fig. 5.17(c) shows a simulated EL image for the case $R_{ZnO} = R_{Mo} = 18\ \Omega_{sq}$, in which the cross-talk is obviously observed. The cross-talk

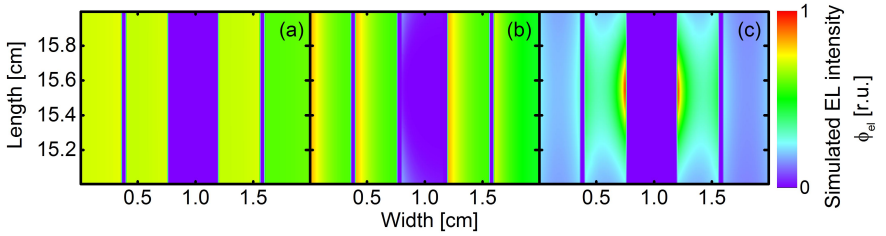

Figure 5.17.: (a) Simulated EL images for $R_{\mathrm{ZnO}} = 0\ \Omega_{\mathrm{sq}}$, $R_{\mathrm{Mo}} = 1.3\ \Omega_{\mathrm{sq}}$. (b) $R_{\mathrm{ZnO}} = 18\ \Omega_{\mathrm{sq}}$, $R_{\mathrm{Mo}} = 0\ \Omega_{\mathrm{sq}}$. (c) $R_{\mathrm{ZnO}} = 18\ \Omega_{\mathrm{sq}}$, $R_{\mathrm{Mo}} = 18\ \Omega_{\mathrm{sq}}$. All other parameters for the simulations are presented in Tab. 5.2 and $R_{\mathrm{s}} = 0.02\ \Omega\mathrm{cm}^2$.

in (c) shows a significantly high EL intensity at the right edge of the left adjacent cell and at the left edge of the right adjacent cell.

In order to compare the magnitude of the cross-talk from different simulations mentioned above, the voltage line-scans V_{l} (open symbols), V_{r} (filled symbols) are plotted in Fig. 5.18(a). It is obvious that the maximal voltage differences between the maximal and minimal values of the voltages V_{l} and V_{r} are reached when $[R_{\mathrm{ZnO}}, R_{\mathrm{Mo}}] = [18, 18]\ \Omega_{\mathrm{sq}}$ (stars). The voltage line-scans V_{l} ($R_{\mathrm{ZnO}} = 0\ \Omega_{\mathrm{sq}}$) and V_{r} ($R_{\mathrm{Mo}} = 0\ \Omega_{\mathrm{sq}}$) are straight lines, which also means that $\mathrm{P}_{2,\mathrm{l}}$ and $\mathrm{P}_{2,\mathrm{r}}$ are equipotential lines. Or in other words, the cross-talk is vanished when at least one of the sheet resistances is zero. Note that the dips observable in the voltage line-scans V_{r} ($R_{\mathrm{ZnO}} = 0\ \Omega_{\mathrm{sq}}$) and V_{l} ($R_{\mathrm{Mo}} = 0\ \Omega_{\mathrm{sq}}$) result from the fact that in the simulation model a shunt resistance of $R_{\mathrm{p2}} = 1e^{-3}\ \Omega\mathrm{cm}^2$ in the $\mathrm{P}_{2,\mathrm{l}}$ and $\mathrm{P}_{2,\mathrm{r}}$ scribing lines is assumed. The results shown in Fig. 5.18(a) also illustrate that the voltage difference is a good measure for the cross-talk.

Figure 5.18(a) also indicates that the lowest voltages V_{l} and V_{r} resulting from the simulation if $R_{\mathrm{ZnO}} = 0\ \Omega_{\mathrm{sq}}$. This is because the perfect conductivity in the front contact and the good conductivity in the back contact enabling almost current flow across the shunts. The voltage line-scans over the junction V_{j} in Fig. 5.18(b) also show that the junction voltage dramatically decreases if $R_{\mathrm{ZnO}} = 0\ \Omega_{\mathrm{sq}}$ with the same reason, i.e. almost current flow across the shunts, which leads to a low junction voltage. With $R_{\mathrm{ZnO}} = 18\ \Omega_{\mathrm{sq}}$, the junction voltage is much higher. Figure 5.18(b)

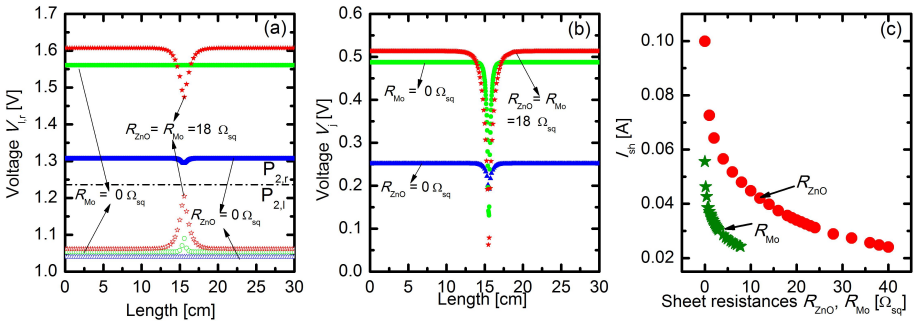

Figure 5.18.: (a) Voltage line-scans V_l, V_r obtained from the various simulations with $[R_{ZnO}, R_{Mo}] = [0, 1.3]$ Ω_{sq}, $[R_{ZnO}, R_{Mo}] = [18, 0]$ Ω_{sq}, $[R_{ZnO}, R_{Mo}] = [18, 18]$ Ω_{sq}. (b) Junction voltage line-scans V_j for different simulations mentioned in (a). (c) Dependence of the shunt current of the sheet resistances R_{ZnO} and R_{Mo}.

illustrates that the junction voltage of the shunted cell is affected by both R_{ZnO} and R_{Mo}. The results state that in a shunted module, the losses of the junction voltage of the affected cells can be reduced by finite values of both R_{ZnO} and R_{Mo}. These findings are consistent with the results from Ref. [136], in which the authors found out that in a solar cell with poor electronic quality, the losses of the open-circuit voltage can be reduced by increasing the local series resistance. However, the results presented in this work regards the effect of the interconnection of the cells in the module and the interaction between the affected cell and its adjacent cells. Thus, this work shows that the neighboring cells affect the degree in which defects are isolated. Figure 5.18(c) proves the results shown in Fig. 5.18(a-b). The current flows over the shunts I_{sh} depends on the values of the sheet resistances R_{ZnO} and R_{Mo}. The lower the values of R_{ZnO} and R_{Mo}, the higher is the shunt current. Especially, when R_{ZnO} is zero, most of the injection current $I = 0.1$ A flows over the shunts, i.e. $(I = I_{sh} \approx 0.1$ A).

To check for the influence of the position of the shunts on the cross-talk, the shunts are shifted from the original position (in the middle) close to the left edge and the right edge of the shunted cell. The effect of the position of the shunts on the

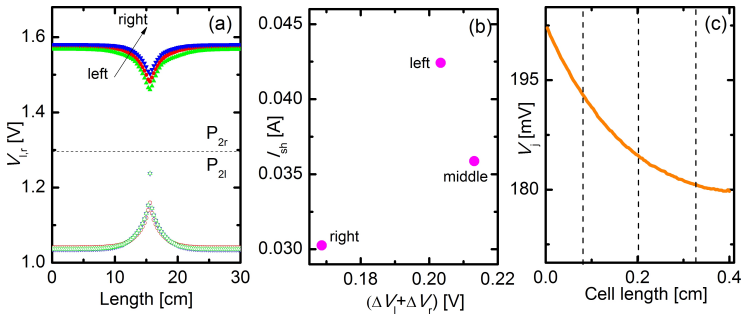

Figure 5.19.: (a) The voltage line-scans V_l (open symbols), V_r (filled symbols) from the simulations, in which the position of the shunts is changed from the middle of the cell (original position) to the left edge and to the right edge of the cell. (b) The shunt current I_sh versus the sum of the voltage differences of the front and back contacts. (c) Line-scan of the junction voltage of one cell from averaging the local junction voltage over the entire length of the cell. The dashed lines exemplify the different positions, where the contour of the shunts are shifted to.

cross-talk is shown in Fig. 5.19. The input parameters for these simulations are $R_\mathrm{s} = 0.02\ \Omega\mathrm{cm}^2$, $R_\mathrm{ZnO} = 18\ \Omega_\mathrm{sq}$, $R_\mathrm{Mo} = 1.3\ \Omega_\mathrm{sq}$ and $R_\mathrm{sh} = [0.005, 0.02, 0.02, 0.008]\ \Omega\mathrm{cm}^2$. The resulting simulated EL and power density images are presented in Appendix A. The voltage line-scans V_l (open symbols) and V_r (filled symbols) shown in Fig. 5.19(a) exhibits a slight difference in the voltages due to the change in position. The current flow across the shunts I_sh is plotted versus the sum of the voltage difference $\Delta V_\mathrm{r} + \Delta V_\mathrm{l}$ of the front and back electrodes (Fig. 5.19(b)). It is shown that the variation of I_sh for different positions of the shunts is also small. The highest value of I_sh is reached if the shunts are close to the left edge of the cell and smallest value if the shunts are close to the right edge of the cell. The reason for that is depicted in Fig. 5.19(c), which shows the junction voltage line-scan of one cell (cell width $w = 0.4$ cm) from averaging the local junction voltage over the entire length of the cell. The decreasing slope of the junction voltage from the left of the cell to the right of the cell is because of the effect of the sheet resistance of the front contact R_ZnO [38]. The voltage at the end of the cell slightly increases, which is due to the effect of R_Mo [38]. Therefore,

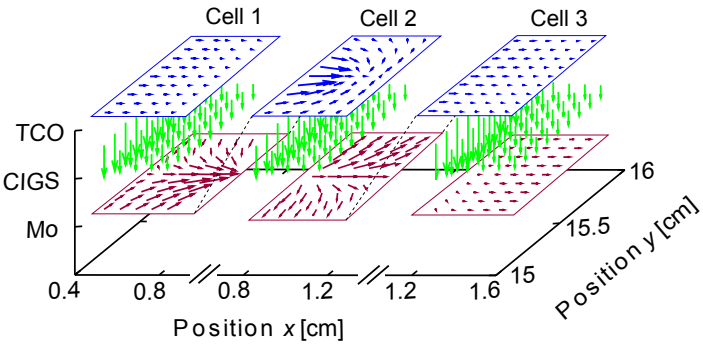

Figure 5.20.: Simulated current density flows over three in series connected CIGS solar cells, where the cell in the middle is shunted.

when the shunts are close to the left of the cell, where the voltage drop across the junction is high, the current flow across the shunts is also high. Analogously, when the shunts are close to the right side of the cell, where the voltage drop across the junction is low, the current flow across the shunts is low.

In the following, the effects of the shunt current and both sheet resistances R_{ZnO} and R_{Mo} on the measure of the cross-talk, i.e. the voltage differences ΔV_{r} and ΔV_{l} are analyzed. Figure 5.20 shows a 3D schematic of three in series connected CIGS solar cells, where the cell in the middle is shunted. The back Mo electrode (bottom) of the previous cell is connected to the front ZnO electrode (top) of the next cell and so forth. The arrows shows that the current flows from the left of the sample to the right. Within one cell, the current flows from the front electrode across the junction to the back electrode. It is obvious that the current has already been collected in the front and back electrodes of the cell 1 before flowing in the shunted cell, and quickly spreads to cell 3. Figure 5.20 clearly shows the electrical interaction of the cells, therefore, it is important for the analysis to take the effect of the interconnection of the cells into account. For simplicity, the interconnection of the electrodes described in Fig. 5.20 is illustrated in a 2D schematic (Fig. 5.21). It is clearly shown that the back sheet resistances R_{b} of cell 1 are in parallel connected to the front sheet resistances R_{f} of cell 2 and so forth. The sheet resistances R_{b} and R_{f}

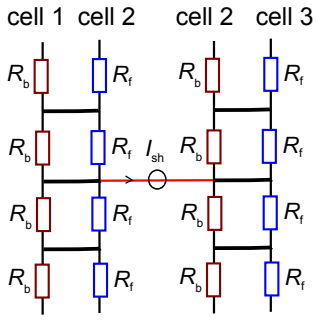

Figure 5.21.: Parallel connection of the front and back electrodes of two different cells with R_p is described in Eq. (5.20).

are the resistances of the back Mo and front ZnO electrode, which are equivalent to R_{Mo} and R_{ZnO}. The parallel connection of R_b and R_f results in a parallel resistance R_p, which is written as

$$R_p = \frac{R_b R_f}{R_b + R_f}. \tag{5.20}$$

Therefore, the total voltage difference $\Delta V = \Delta V_r + \Delta V_l$ can be expressed by the following equation

$$\Delta V \propto I_{sh} R_p. \tag{5.21}$$

Furthermore, a ratio $f = R_f/R_b$ is defined, which also describes the relationship between the front and back resistances. Note that the geometry of the device is also included in f. The relationship described in Eq. (5.21) and the ratio f allow a more systematic analysis of the cross-talk effects by varying the input parameters R_p and f more methodically. Various simulations are done by changing the values of the parallel resistance R_p, which is defined in Eq. (5.20). For each value of R_p, three simulations with $f = [0.1, 1, 10]$ are carried out. The input parameters for the various simulations are given in Tab. 5.3. The results of the simulations are presented in Fig.5.22.

Figure 5.22 presents the total voltage differences ($\Delta V = \Delta V_l + \Delta V_r$) versus the parallel resistance R_p (a) and the ratio f (b). Different symbols represent different

Table 5.3.: The input parameters for various simulations to investigate the effect of the sheet resistances $R_{\mathrm{ZnO}} = R_{\mathrm{f}}, R_{\mathrm{Mo}} = R_{\mathrm{b}}$ of the front and back contacts on the cross-talk.

Fixed parameters	$f = R_{\mathrm{f}}/R_{\mathrm{b}}$	$R_{\mathrm{p}} = R_{\mathrm{f}}R_{\mathrm{b}}/(R_{\mathrm{f}} + R_{\mathrm{b}})$
$n_{\mathrm{id}} = 1.57$	0.1, 1, 10	0.1 [Ω_{sq}]
$R_{\mathrm{sh,opt}} = [0.005, 0.02, 0.02, 0.008]$ $\Omega\mathrm{cm}^2$	0.1, 1, 10	1 [Ω_{sq}]
$J_0 = 2.63 \times 10^{-8}$ [mAcm^{-2}]	0.1, 1, 10	10 [Ω_{sq}]
$J = 8.3$ [mAcm^{-2}]	0.1, 1, 10	100 [Ω_{sq}]
$R_{\mathrm{s}} = 0.02[\Omega\mathrm{cm}^2]$		

values of R_{p} as listed in Tab. 5.3 and different positions of the shunts. Figures 5.22(a-b) include both the effect of R_{p} and I_{sh}. Nevertheless, the effect of the parallel resistance R_{p} on the total voltage difference ΔV is clearly observed in Fig. 5.22(a). The total voltage difference is high for $R_{\mathrm{p}} = 1$ Ω_{sq} and $R_{\mathrm{p}} = 10$ Ω_{sq}. For small $R_{\mathrm{p}} = 0.1$ Ω_{sq} or large $R_{\mathrm{p}} = 100$ Ω_{sq}, the voltage differences decrease. For each value of R_{p}, three points are plotted corresponding to the three values of f. The deviation of the total voltage difference at each value of R_{p} is due to the effect of the ratio f, which is illustrated in Fig. 5.22(b). The trend in Fig. 5.22(b) shows that for most of various R_{p}, the highest voltage differences occur if $f = 1$, except for the case that $R_{\mathrm{p}} = 0.1$ Ω_{sq}.

Figure. 5.18(c) illustrates that the shunt current I_{sh} strongly depends on R_{p}. A clearly observable trend shows that the higher the parallel resistance R_{p}, the lower is the shunt current I_{sh}, which is consistent with the results shown in Fig. 5.18(c). In contrast, the effects of the ratio f on the shunt current I_{sh} are much smaller. For most values of R_{p}, a slight increase of the shunt current occurs for $f = 1$. The dependency of the shunt current on R_{p} is also shown in Fig. 5.18(d) (the straight arrow). For R_{p} from 1 Ω_{sq} to 100 Ω_{sq}, the values for the shunt current for $f = 1$ are slightly higher than for other values of f. In order to focus on the effect of R_{p} and f on the cross-talk, the total voltage difference is normalized to the shunt current to eliminate the effects of the shunt current. The normalized voltage difference $\Delta V/I_{\mathrm{sh}}$ is plotted versus R_{p} and f in Figs. 5.22(e-f), respectively. By normalizing to the

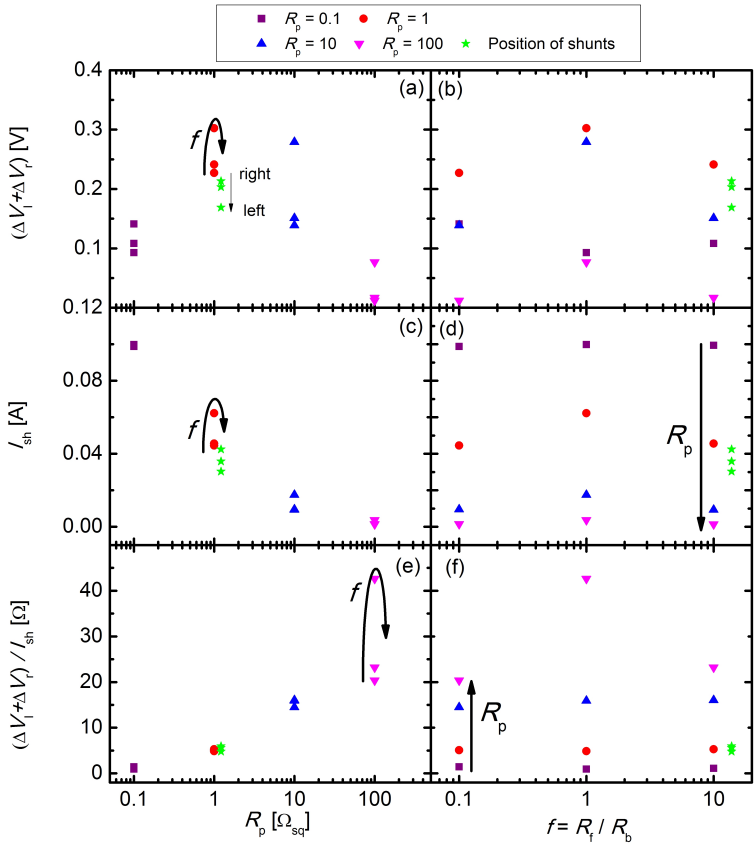

Figure 5.22.: (a-b) Voltage difference $\Delta V_\mathrm{l} + \Delta V_\mathrm{r}$ versus R_p and f. (c-d) Shunt current I_sh versus R_p and f. (e-f) Normalized voltage difference $(\Delta V_\mathrm{l} + \Delta V_\mathrm{r})/I_\mathrm{sh}$ versus R_p and f.

shunt current, a clearer trend is observed for $\Delta V/I_\mathrm{sh}$ versus R_p (e) compared to (a). The trend shows that the higher the parallel resistance R_p, the higher is $\Delta V/I_\mathrm{sh}$. For R_p from 0.1 Ω_sq to 10 Ω_sq, the ratio f only has a minor effect on $\Delta V/I_\mathrm{sh}$. With $R_\mathrm{p} = 100\ \Omega_\mathrm{sq}$, a large deviation of the normalized voltage difference for different f is visible, where the highest value for $\Delta V/I_\mathrm{sh}$ occurs when $f = 1$. Figure 5.22(f) also

supports this observation. By using a simplified model from Fig. 5.21, the effects of the parallel resistance R_{p} on the cross-talk are well understood.

It is important to mention here that the model used for the systematic analysis is a 1D model. In this model, the position of the shunts and the geometry of the device are neglected. The results in Fig. 5.19 show that the position of the shunts only slightly affect the cross-talk. The star symbols shown in Figs. 5.18(a-f) are the voltage differences obtained from varying the position of the shunts as shown in Fig. 5.19 and in Appendix A, which indicate that the effects of the position of the shunts are neglectable. However, neglecting the effects of the geometry of the device is a possible error source, which makes this model to be insufficient to explain the effects of the ratio f on the measure and the normalized measure of the cross-talk. Therefore, the full 2D problem must be considered to understand the influences of f.

In this section, the effects of the shunts and the sheet resistances on the voltage differences, or in other words on the cross-talk are analyzed in detail. It is shown that the cross-talk disappear when at least one of the sheet resistances is zero. The voltage difference is a useful measure for the cross-talk, which allows the detailed analysis of the shunts and the sheet resistances on the cross-talk. The result from this analysis shows that the cross-talk or the voltage difference strongly depends on the shunt current, the parallel resistance R_{p}. In contrast, the ratio f only has a minor effect on the voltage difference. The position of the shunts only slightly influences the shunt current and the voltage difference. A 1D model explained the effects of R_{p} well, whereas the effects of f cannot fully understood with this 1D model.

5.6. Summary

In this chapter, a detailed study of the cross-talk effect resulting from the shunts and the series resistance of the ZnO and Mo contacts has been shown with the help of EL and DLIT measurements as well as a spatial modeling using NSM and SPICE. The summary of the results from this study are presented below.

- The measured EL and DLIT images are in a good agreement and comple-

ment one another. The consistency of the simulation and measurement results proves that the spatial modeling using NSM and SPICE is a powerful tool for the detailed analysis of defects and resistive losses in CIGS devices.

- The comparison of the simulated and measured EL images is appropriate for the description of the cross-talk and for the determination of the sheet resistances of the front and back electrodes. The comparison of the simulated power density and the measured DLIT images is well suited for the localization of the shunts and for the approximation of the shunt resistances. However, this method shows a limitation for the determination of the bulk series resistance.

- The definition of the voltage difference as a measure for the cross-talk is useful for the detailed analysis of the cross-talk. Additionally, another advantage of the simulation model against the measured EL image is that the shunt current can be determined, therefore, a definition of a measure for the cross-talk from simulation results is more precise than from measured EL image.

- Further findings of this work show that in a module, which consists of several in series connected cell, the junction voltage of the shunted cell is affected by the neighboring cells. To reduce the losses of the junction voltage, the sheet resistances of the front and back electrodes should be increased.

- It is further found that the change of the position of the shunts only has a minor impact on the cross-talk. A systematic analysis of the effects of shunts and the sheet resistances shows that the cross-talk depends on the shunt current, the parallel resistance, the ratio between the sheet resistances including the effects of the geometry of the devices. A 1D model used for this analysis is good to understand the effects of the parallel resistance. However, this model is insufficient to explain the effects of the ratio between the sheet resistances.

6. Phenomenology of defects in Cu(In,Ga)Se_2 solar cells

This chapter presents a classification of commonly observed defects within large-scale industrially produced Cu(In,Ga)Se_2 thin-film solar modules. The classification of the various defect types is based on their appearances in electroluminescence (EL) images. Furthermore, different characterization techniques, such as dark thermography (DLIT), photoluminescence (PL), scanning electron microscopy (SEM), and focused ion beam (FIB) imaging, are used to obtain detailed information about the structural, electrical, and optical properties of these defect types.

6.1. Introduction

Understanding the origin of defects in a photovoltaic device is mandatory to avoid their creation during the fabrication process, and may help to optimize the process. Defects have various origins and appearances, and therefore, different consequences on the performance of the devices.

The aim of this chapter is to classify phenomenological defects in industrially produced CIGS solar modules [20, 79]. In this thesis, four types of defects in CIGS devices are presented, which are named "standard shunts", "Smears", "Freckles", and "Doughnuts" according to their respective appearance in EL images. Standard shunts also appear in solar cells produced with different technologies, such as crystalline silicon and CdTe [94,130,137–139], and have been already investigated in CIGS devices using various characterization tools such as EL, PL, LIT and scanning electron microscopy (SEM) [40, 101, 102, 133, 140]. A detailed analysis of standard shunts in CIGS sola cells and modules and their impact on the performance of the devices, e.g. the cross-talk effect is given in chapter 5. An EL image of a CIGS

module containing a standard shunt is presented in Fig. 6.1(a).

The following sections focus on the analysis of the other three defect types, namely, Smears, Freckles, and Doughnuts using various characterization techniques such as spatially and spectrally resolved EL and PL, and DLIT. For in-depth analysis of the microstructure and stoichiometry, scanning electron microscopy (SEM) and focused ion beam (FIB) imaging are also applied.

6.2. Macro- and microscopic analysis of defects in CIGS solar modules

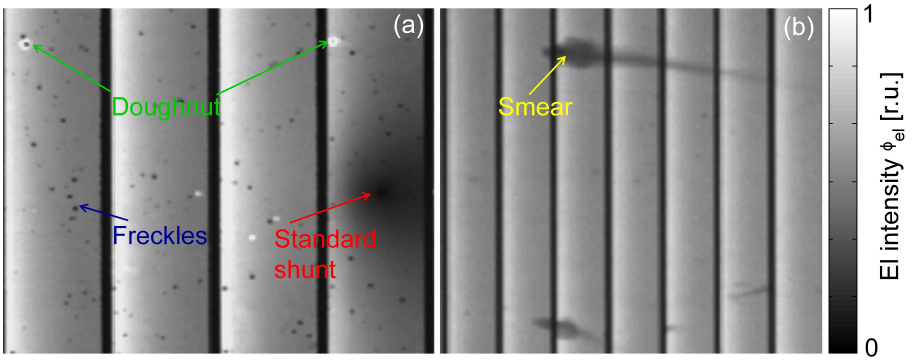

Figure 6.1.: Defect types observed in CIGS thin-film solar modules: (a) Freckles, (b) Smears, and (c) Doughnuts.

For the analysis, EL and DLIT images of CIGS samples are recorded with a high resolution (3056 × 3056 pixel) Si-CCD camera, an (640 × 512 pixels) InGaAs camera, and an infrared camera with an InSb detector (288×288 pixels), respectively (see chapter 3). Photoluminescence images are taken with the same InGaAs camera using a laser with 532 nm wavelength as an excitation source.

While EL provides information on both optical (electrically non-active) defects and (electrically active) shunts (more blurred than DLIT image), DLIT is more appropriate for the localization and detection electrical defects (shunts). By combining

both methods, optical and electrical defects can therefore be distinguished from each other.

Figure 6.1 displays Freckles (a), Smears (b), and Doughnuts (c) observed in a CIGS module. Freckles appear in EL images as dark spots with sharp contours (diameter: 10 to 200 µm). Smears consist of a small dark spot and a tail (length: 2 to 12 mm), which smears out over several cells. Furthermore, Doughnuts can be visible in EL images with various appearances. They often show a dark center (diameter: 10 to 50 µm), surrounded by a bright ring (diameter: 20 to 150 µm). In the following, all three defect types are analyzed in detail.

6.2.1. Freckles

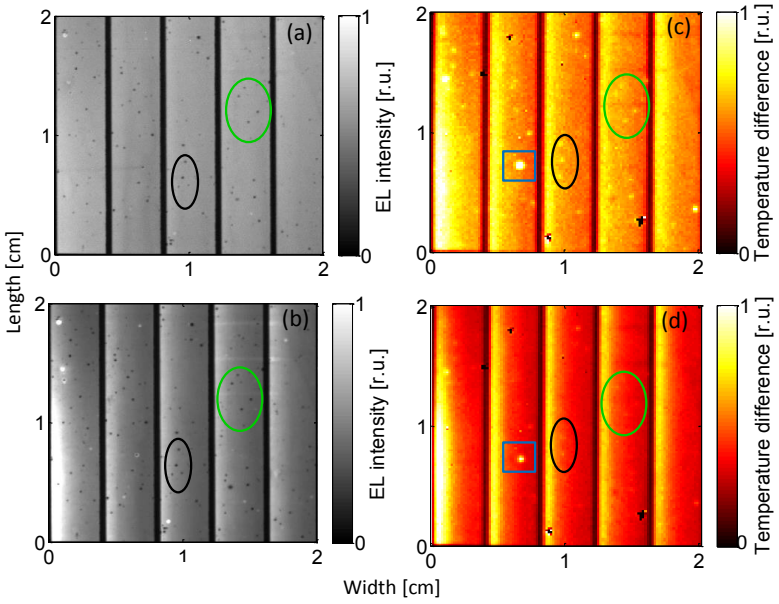

Figure 6.2.: EL images of a CIGS module containing Freckles measured at (a) a low current density $J = 2.5$ mAcm^{-2} and (c) a high current density $J = 20$ mAcm^{-2}. DLIT images of the same CIGS sample as in (a) measured at (b) $J = 2.5$ mAcm^{-2} and $f_{\text{lock-in}} = 3$ Hz and (d) $J = 20$ mAcm^{-2} and $f_{\text{lock-in}} = 3$ Hz.

Figure 6.2 illustrates EL images of a mini CIGS module (5×4 cm^2) recorded at a low injection current density $J = 2.5$ mAcm^{-2} (a) and a high injection current density $J = 20$ mAcm^{-2} (b). Freckles are clearly observable as dark spots with sharp contours (marked ellipses) in both EL images. The DLIT images measured at the same injection current densities J and with a lock-in frequency of $f_{\text{lock-in}} = 3$ Hz are presented in Figs 6.2(c,d). The Freckles (marked ellipses) are slightly visible in the DLIT image measured at $J = 2.5$ mAcm^{-2} (c) and hardly observable in the DLIT image at $J = 20$ mAcm^{-2} (d), even when the contrast in the DLIT images

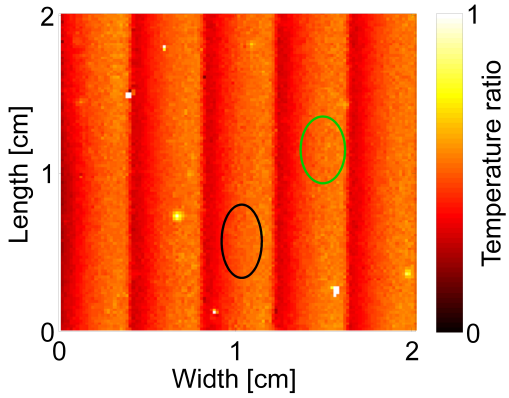

Figure 6.3.: A ratio DLIT image of a CIGS module obtained by dividing the DLIT image shown in Fig 6.2(c) to the DLIT image shown in Fig 6.2(d).

is strongly enhanced. Both EL and DLIT images reveal that the surroundings of the Freckles are not affected, which indicates that Freckles are electrically isolated defects.

A ratio image is calculated from dividing the DLIT image (c) to the DLIT image (d). The resulting ratio image is shown in Fig. 6.3. All the Freckles observable in the EL and DLIT images disappear in the ratio image. However, the shunt (marked rectangle) in the DLIT images is still observable in the ratio image, which indicates that the Freckles are not shunts, but rather electrically isolated defects. The result from the DLIT images ascribe that Freckles may originate from the difference in emissivity.

The electrically non-active nature of the individual Freckles makes them less hazardous. Or in other words, Freckles result in dead area. However, due to the large numbers they can cause active area losses, thus, reduce the short-circuit current, and consequently the efficiency of the devices. For example, the dead area caused by the Freckles shown in Fig. 6.1(a) is $\approx 4\%$ of the entire active area.

Figure 6.4 shows a microscopic EL (a) and PL (b) image of another CIGS module (5×4 cm^2), both are recorded with an InGaAs camera. The microscopic EL image shown in Fig. 6.4(a) exhibits a round Freckle with a diameter of ≈ 130 µm.

The Freckle has a sharp contour, in which the EL intensity is almost zero, whilst the surrounding area is unaffected. The microscopic PL image shown in Fig. 6.4(b) taken with the same InGaAs camera only shows a slight decrease of the PL intensity at the Freckle.

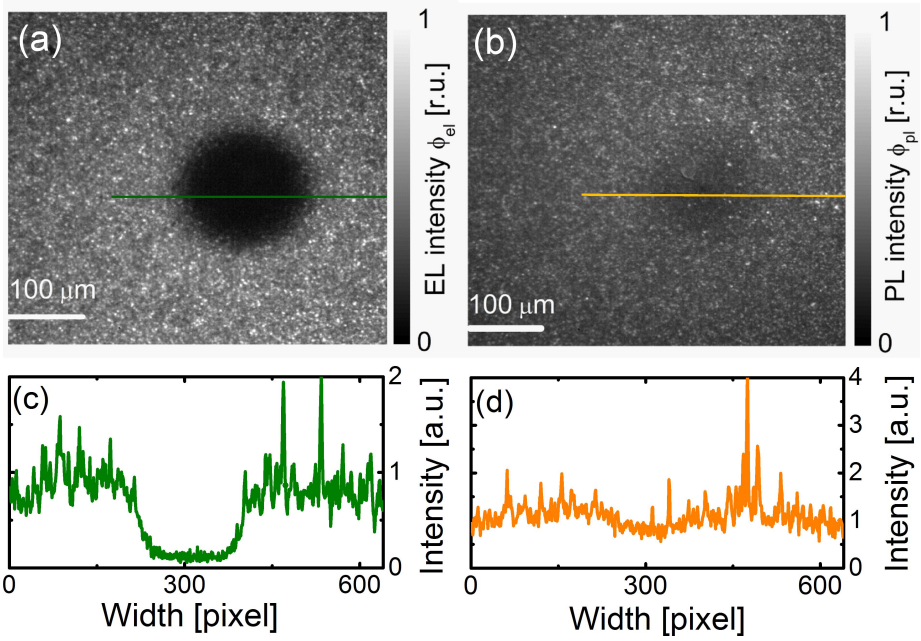

Figure 6.4.: (a) Microscopic EL image of a CIGS module (5×4 cm^2) recorded at $J = 50$ mAcm^{-2} with an InGaAs camera. (b) Microscopic PL image of the same Freckle recorded at the same injection current density and the same InGaAs camera as in (a). (c) Normalized EL line-scan along the marked line across the Freckle shown in (a). (d) Normalized PL line-scan along the marked line across the Freckle (b).

The normalized line-scan of the EL intensity presented in Fig.6.4(c) is taken from the marked line in Fig. 6.4(a). The normalized EL line-scan exhibits an abrupt decrease of the EL intensity to almost zero between the defect-free regions and the Freckle. However, the normalized PL line-scan in Fig. 6.4(d) illustrates only

a small difference between the PL intensity at the Freckle and at the defect-free regions, which indicates that the absorber material is probably unaffected. For further surface investigation of the Freckle, SEM and optical microscope are used. However, the Freckle region shows no peculiarities with these methods, which proves that the origin of the Freckle does originate from the ZnO:Al layer but most probably from either the i-ZnO or CdS or Mo layer.

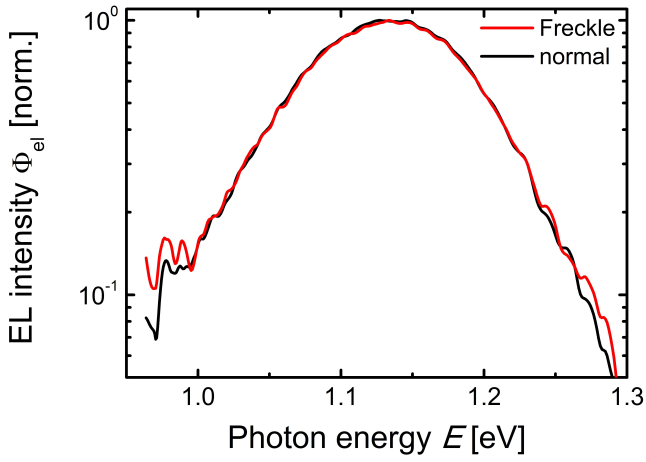

Figure 6.5.: Normalized EL spectra of the CIGS sample shown in Fig. 6.4(a) at a defect-free position and at a position of the Freckle. The spectra have the same shape and peak position.

The EL emission spectrum of a CIGS device [58, 141] is at wavelengths, where the external quantum efficiency of the Si camera drops rapidly. Therefore, a decrease in measured intensity can also mean an IR-shift of the emitted spectrum. Thus, the spectrum of the Freckles is compared to those of unaffected areas.

Figure 6.5 shows that the normalized EL spectra to their respective maximum recorded at a position of the non-defective area and at a position of the Freckle have the same shape, i.e. no peak shift is observed. This result supports the observation in the EL and PL images presented in Fig.6.4 that the Freckles results in low EL in-

tensity but the absorber material is unaffected. Note that the collected photons may partly also originate from the unaffected surrounding area. For the PL-spectroscopy (not displayed), the PL spectra at the Freckles were found to be the same as at the normal area as well. Note that all spectra were corrected for the wavelength depended spectrometer efficiency. The results from the spectroscopic measurements are consistent with the results shown in Figs. 6.4(b,d), where the PL intensity at the Freckle is slightly lower than at the non-defective areas.

6.2.2. Smears

Another defects are the so called Smears. Examples are displayed in Fig. 6.6, where (a) shows a DLIT image and (b) an EL image of a CIGS module (5×5 cm^2) recorded at $J = 16.7$ mAcm^{-2} and $f_{\text{lock-in}} = 3$ Hz before the sample was light soaked. The Smears appear in the EL image (Fig. 6.6(b)) with dark centers and with tails. However, the tails of the Smears are not obviously visible in the DLIT image (Fig. 6.6(a)). Both EL and DLIT images reveal that Smears are electrically active defects (shunts), which may have a major impact on the cell and module performance.

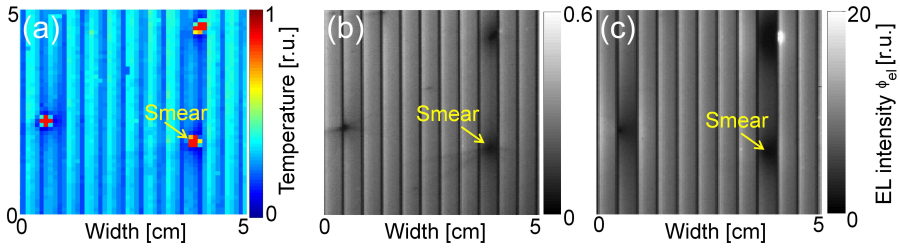

Figure 6.6.: (a) DLIT image recorded before light soaking (LS) of a CIGS module containing Smears.(b)EL image recorded before LS of the same module as in (a). (c) EL image measured after LS of the same sample as in (a).

For further investigation, the same sample was light soaked for 48 hours with a white light source (class B spectrum) of 1000 W/cm^2 at a temperature of 50°C. Another EL image was recorded at $J = 16.7$ mAcm^{-2} immediately after LS (Fig. 6.6(c)). After the LS, all of the tails vanished, whereas the centers of the Smears are more pronounced. Note that the gray-scales of the EL images recorded by a Si-CCD camera in Figs. 6.6(b) and (c) are different.

Figure 6.7 displays two line-scans of the relative local junction voltage $V'_{\text{j,cell}}$ calculated from the EL images before (dashed line) and after LS (solid line) as described in Sec. 2.2. The voltage difference between the shunted and the non-shunted cell is more pronounced after LS than before LS ($\Delta V'_{\text{j}} = 12.4$ mV compared to 7 mV), which indicates that the reduction of the junction voltage due to the

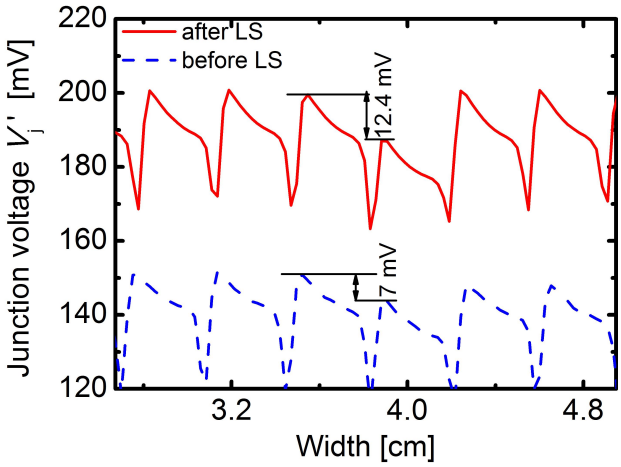

Figure 6.7.: Line-scans of the relative junction voltage calculated from the EL images shown in Figs. 6.6(b,c) before (dashed line) and after LS (solid line).

shunts is stronger after the LS experiment.

After the acquisition of the EL image (Fig. 6.6(b)), the sample was kept in the dark for 6 months at room temperature. Subsequently, an EL image of the same sample was recorded again (not shown), which shows that the tails did not return. The investigation of Smears also shows that the tail length is in the range of 0.2 to 1.2 cm. The tails often point in the same direction, which indicates a common origin related to a production step. The tails may arise from a variation in the chemical compositions of the sample. However, the more detrimental effect on the performance of the device is caused by the center (head) of the Smears, which appears as shunts in EL and DLIT images.

6.2.3. Doughnuts

The last defect type discussed in this work is the so called Doughnut, which can have various appearances in EL images. Two types of Doughnuts are commonly observed in the CIGS samples investigated in this work, which are subclassified into

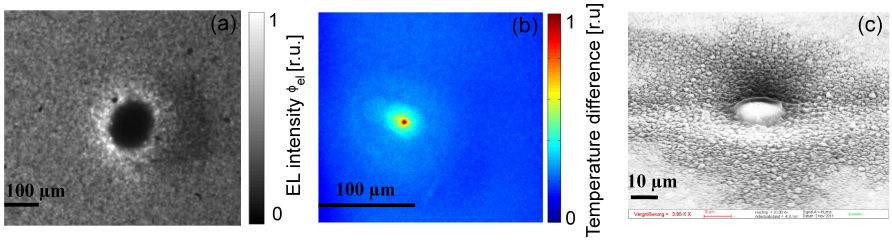

Figure 6.8.: (a) EL image recorded with a Si-CCD camera, in which a Doughnut of Type I with dark center and a bright ring is obviously observed. (b) Microscopic DLIT image of the same Doughnut shown in (a), which indicates that the Doughnut is slightly electrically active. (c) SEM image of the same Doughnut shown in (a) and (b), tilted by 45°.

Doughnut Type I and Type II.

An EL image (Figure 6.8(a)) of a CIGS module (5×5 cm^2) recorded at $J = 20$ mAcm^{-2} with a Si-CCD camera exhibits a Doughnut of Type I with a diameter of ≈ 140 µm, a dark center, and a bright ring. In the EL image, the surrounding areas of the Doughnut are unaffected. A microscopic DLIT image in Fig. 6.8(b) measured at the same current density J displays the same Doughnut as in Fig. 6.8(a). The microscopic DLIT image indicates that the center of this Doughnut (diameter $\approx$ 15-20 µm) is a very small shunt.

A 45° tilted SEM image shown in Fig. 6.8(c) also illustrates that the diameter of the center of the Doughnut is $\approx$ 15-20 µm. Furthermore, the SEM image also depicts that the center of the Doughnut has a lenticular form. It could originate from impurities.

Another Doughnut of Type I in a (30×30 cm^2) CIGS sample is presented in Fig. 6.9(a). The EL image is recorded at $J = 8.3$ mAcm^{-2} by a Si-CCD camera. The Doughnut shows the same appearance (a dark center and a bright ring) as the Doughnut exhibited in Fig. 6.8(a). Note that this Doughnut is also a natural defect observed in CIGS solar cells as all other defects mentioned in this work. To check whether, the material properties of the bright ring and the center are the same, an EL image of the same region is recorded with an InGaAs camera, which is displayed

in Fig.6.9(b). The bright ring of the Doughnut disappears in the EL image measured with the InGaAs camera, which denotes that the bright ring has a different spectrum compared to the center and the normal regions. This finding also indicates that the material properties of the bright ring are different from those of other regions.

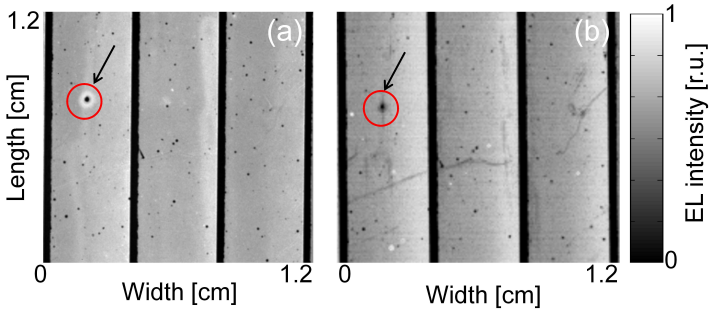

Figure 6.9.: (a) EL image of a CIGS module recorded with a Si-CCD camera, which shows a Doughnut (marked circle). (b) EL image of a CIGS module with the same marked Doughnut as in (a) recorded with an InGaAs camera.

The different appearances of the Doughnut in Figs.6.9(a,b) can be explained by Fig. 6.10, which shows the normalized EL spectrum of a CIGS solar cell and the normalized external quantum efficiencies Q_{cam}(Si) and Q_{cam}(InGaAs) of the Si-CCD and the InGaAs camera used in this thesis. If the EL spectrum of the Doughnut of Type I is shifted towards higher energies of $E \geq 1.21\ eV$, the change of the convolution of the EL spectrum with Q_{cam}(InGaAs) is negligible small, therefore, the InGaAs camera does not see the difference in the EL intensity between the normal area and the bright ring observed in the EL image with the Si-CCD camera. In contrast, the convolution of the EL spectrum of the Doughnut with Q_{cam}(Si) considerably increases, which results in the bright ring of the Doughnut.

The so-called Doughnut of Type II has a different appearance in EL image compared to the Doughnut of Type I. A microscopic EL image of a CIGS module (5×5 cm^2) recorded by a Si-CCD camera at $J = 45$ mAcm^{-2} (Fig. 6.11(a)) exhibits a large Doughnut with a diameter of ≈ 240 µm, whose center is concentric by two rings. The outer ring has the highest EL intensity, whereas the EL intensity at the

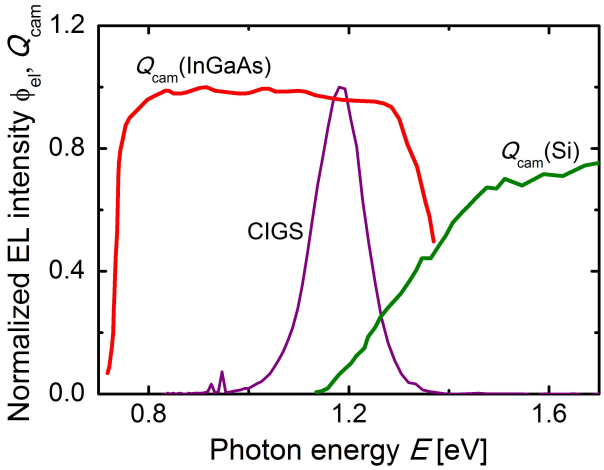

Figure 6.10.: Normalized EL spectrum of a CIGS solar cell and normalized external quantum efficiencies Q_{cam}(Si) and Q_{cam}(InGaAs) of the Si-CCD and the InGaAs camera, respectively.

inner ring is very low, even lower than that of the center. The EL intensity of the center has the same values as that of the normal region, except for the position at the scratch, where the EL intensity is almost zero. The scratch is more obvious in the PL image in Fig. 6.8(c) and in the SEM image in Fig. 6.12.

The outer and inner rings of the Doughnut in the EL image recorded by the InGaAs camera at $J = 50$ mAcm^{-2} (Fig. 6.8(b)) show the same features as in the EL image taken by the Si-CCD camera. However, the entire center of the Doughnut in Fig. 6.8(b) is dark, which indicates that the spectrum at the center may differ from that of the rings and of the normal regions. Or in other words, the material compositions at the center of the Doughnut probably differ from other regions. In the microscopic PL image (Fig. 6.11(c)) recorded with the same InGaAs camera using a 808 nm wavelength diode laser, the outer and inner rings are also visible as in the EL images. However, the center of the Doughnut has the same PL intensity as in the normal regions, which proves that the absorber material is unaffected.

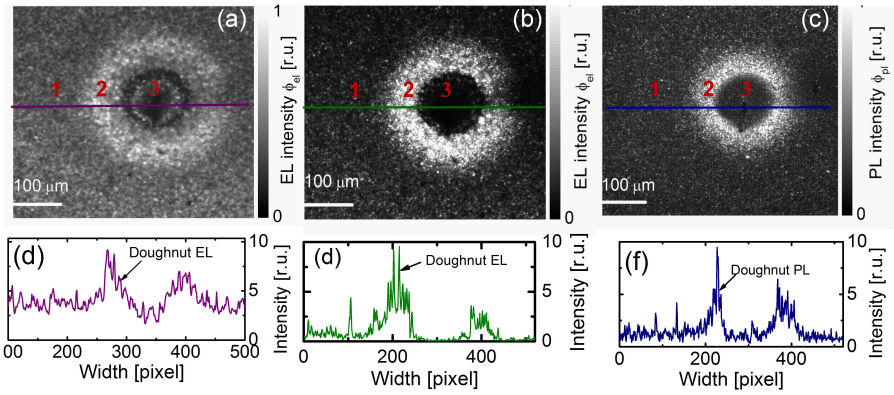

Figure 6.11.: (a) Microscopic EL image of a Doughnut of Type II recorded with a Si-CCD camera. Different regions are marked with respective numbers (1, 2, 3), namely, the normal area (1), the outer ring (2), and the center (3). (b) Microscopic EL image recorded with an InGaAs camera of the same Doughnut shown in (a). (c) Microscopic PL image recorded with an InGaAs camera of the same Doughnut shown in (a). (d) Line-scan of the EL intensity across the Doughnut shown in (a). (e) Line-scan of the EL intensity across the Doughnut shown in (b). (f) Line-scan of the PL intensity across the Doughnut shown in (c).

The EL and PL line-scans shown in Figs. 6.11(d-f) are obtained from the marked lines in Figs. 6.11(a-c) across the Doughnut. All the line-scans denote that the intensity at the outer ring is higher than that of the other regions. The EL intensity in the center of the Doughnut obtained from the Si-CCD camera (Fig. 6.11(d)) has almost the same level as in the normal regions. The normalized PL line-scan from the PL image recorded with the InGaAs camera (Fig. 6.11(f)) also shows the same trend. However, the normalized EL line-scan (Fig. 6.11(e)) taken from the InGaAs camera illustrates that the EL intensity at center is almost zero.

In order to gain further information about the origin of the Doughnut of Type II, other characterization tools are used as well, namely, SEM and FIB. For simplicity, the numbers (1, 2, 3) shown in Figs. 6.11(a,b) correspond to the normal region (1), the outer ring (2), and the center (3).

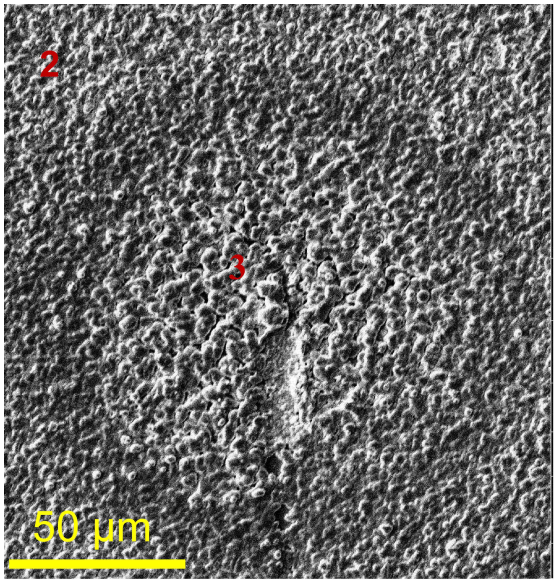

Figure 6.12.: SEM image of the same Doughnut presented in Fig. 6.11 reveals that the grains at the center of this Doughnut are more coarse than that in other regions.

An SEM image of the same Doughnut presented in Fig. 6.12 exhibits the outer ring (2), the inner ring (black ring), and the center of the Doughnut (3). It is obvious that in the center of this Doughnut (3), the grains are more coarse than those in the outer ring (2). The difference in the size of the grains also indicates that the material properties of the center may differ from that of the outer ring. The black ring shown in the SEM image corresponds to the inner ring visible in the EL image in Fig. 6.11.

For further in-depth analysis of this Doughnut, FIB cross-sections were carried out at the normal region (1) and at the black ring of the Doughnut. The SEM images presented below point out the regions where the FIB sections were taken. Figure 6.13(a) shows an SEM image of the normal region (3), which presents the position, where the FIB measurement shown Fig. 6.13(b) was carried out. The ZnO/CdS/CIGS/Mo/Glass layers exhibited in the FIB image in Fig. 6.13(b) do not show any abnormal feature.

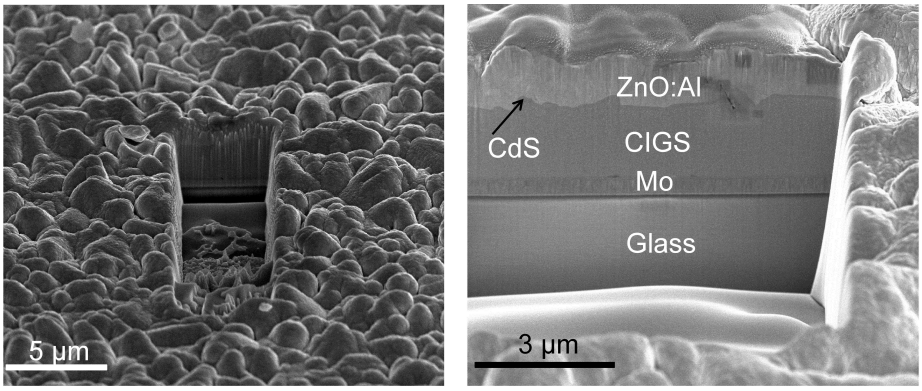

Figure 6.13.: (a) An SEM image of the normal region, which shows the location, where the FIB measurements were taken, (b) FIB image of the normal region.

Figure 6.14(b) represents a FIB cross-section of the black-ring shown in the SEM image in Fig. 6.14(a). Note that the black ring in the SEM image is the observable inner ring shown in Fig. 6.11(a). In contrast to the FIB image of the defect-free region, the FIB image of the black ring shows several abnormal features, i.e. the bright spots in the CIGS absorber layer close to the CdS/CIGS interface. Furthermore, the CIGS absorber material at the CIGS/Mo interface has a poor adhesion. Figures 6.13 and 6.14 demonstrate the difference of the ZnO/CdS/CIGS/Mo/Glass layers in the defect-free region and in the defective region. However, the reasons for these abnormal features and whether they are responsible for the black ring of the Doughnut or not, are still unknown.

As mentioned above, the SEM image in Fig. 6.12 indicates that the material properties of the outer ring (2) may differ from that of the center of the Doughnut (3), which is consistent with the result from the comparison between the EL images taken with the Si-CCD camera (Fig. 6.11(a)) and the InGaAs camera (Fig. 6.11(b)). Additionally, the result from the PL image (Fig. 6.11(c)) indicates that the difference between the absorber material at the center and at the other regions is barred.

In order to verify the results presented in SEM, EL and PL images, further investigation of the Doughnuts were carried out with EL and PL spectroscopy mea-

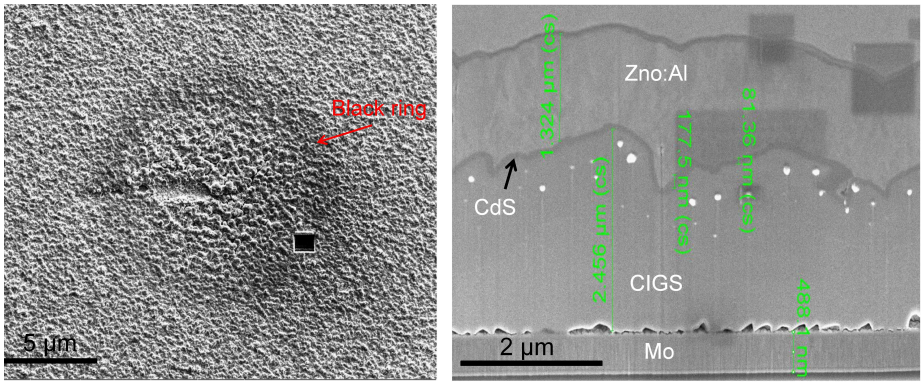

Figure 6.14.: (a) SEM image of the black ring, which shows the location, where the FIB measurement was carried out, (b) FIB image of the black ring.

surements at different positions (1, 2, 3). Note that the numbers (1, 2, 3) used here denote the normal regions, the outer ring, and the center, respectively.

The results of the EL and PL spectroscopy measurements are depicted in Fig. 6.15(a,b), respectively.

Figure 6.15(a) illustrates the normalized EL spectra of the Doughnut shown in Fig. 6.11, which are recorded at various positions, namely, at the normal position (1), the outer ring (2), and the center (3). The normalized EL spectra at the normal region and at the outer ring have the same peak energy at $E_{\text{peak}} \approx 1.13$ eV, whereas the EL spectrum at the center exhibits a shift of the peak energy to $E_{\text{peak}} \approx 1.21$ eV. Note that the shoulder at $E_{\text{peak}} \approx 1.18$ eV may stem from the EL intensity at the unaffected regions.

Figure 6.15(b) displays the normalized PL spectra, which are measured at the same positions as discussed in Fig. 6.15(a). The PL spectra are very similar to the EL spectra shown in (a). However, the peak energy of the PL spectrum recorded at the center shifts more towards higher energy $E_{\text{peak}} \approx 1.25$ eV compared to that of the EL spectrum in Fig. 6.15(a).

Both EL and PL spectra point to different the material properties of the center of the Doughnut, whilst the outer ring has the same material properties as that of the normal regions. The results from the EL and PL spectroscopy measurements are

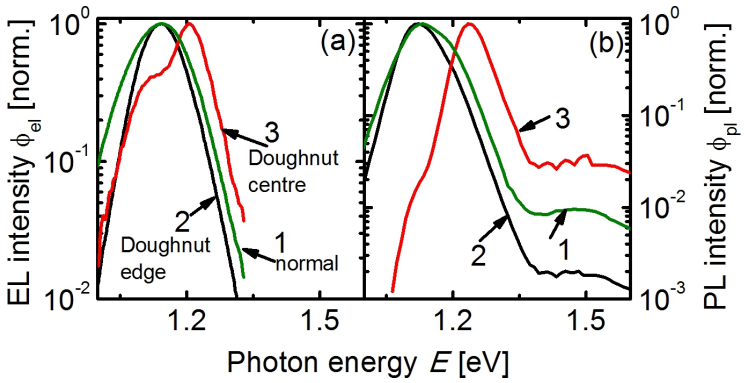

Figure 6.15.: (a) Normalized EL spectra of the Doughnut shown in Fig. 6.11 recorded at different positions, such as normal position (1), the outer ring (2), and the center (3). The normalized EL spectrum at the normal position and at the outer ring have the same peak energy at $E_{peak} \approx 1.13$ eV. The spectrum at the center is shifted to higher energy $E_{peak} \approx 1.21$ eV. (b) Normalized PL spectra of the same Doughnut shown in Fig. 6.11 recorded at the same positions as discussed in (a). The peak energy of the PL spectrum recorded at the center shifts more towards higher energy $E_{peak} \approx 1.25$ eV compared to that of the EL spectrum in (a).

consistent with the result shown in the SEM image (Fig. 6.12) and the luminescence images (Fig. 6.11) mentioned above. Note that for this Doughnut, a DLIT image (not shown here) was also taken, which shows that this Doughnut is a small shunt.

The analysis of the Doughnuts point to the fact that there are various types of Doughnuts. The two examples of Doughnuts presented in this work yield no consistent properties of the Doughnut. Using various characterization techniques, such as SEM, FIB, EL imaging, EL and PL spectroscopy measurements are important to distinguish different types of Doughnut. The results from these methods also reveal that Doughnuts are most probably caused by a difference in the material properties, which may originate from impurities.

6.3. Summary

In this chapter, a detailed study of varied defect types observed in large-area industrially produced CIGS modules is presented. With the help of various characterization tools, such as EL, DLIT, PL, SEM, and FIB images, the optical and electrical properties of the defects are analyzed.

Table 6.1 summarizes the various defect types shown in this chapter. Furthermore, the methods used for the investigations of the defects and the results from this study are also presented in this table.

- Normal shunts significantly affect the device performance. The normal shunts have various origins.
- Freckle defects shown in this work are electrically isolated defects. However, the absorber material at the Freckles is unaffected. DLIT measurements indicate that Freckles most probably result from the difference in emissivity of the materials. Freckles cause the reduction of the active area, thus, reduce the short circuit current and the efficiency of the device.
- Smears are electrically active defects, which have a center (head) and tail. The centers of the Smears are strong shunts, whereas the tails are electrically non-active. The tails appear dark in EL images and often point to the same direction, which indicates that the origin of the tails may arise from a production step.
- Doughnuts are weak shunts, which can have various appearances in EL images and may result from differences in the material properties caused by impurities.

Table 6.1.: Defect types, methods to characterize the defects, and results.

Defects	EL	PL	LIT	LS	SEM	FIB	Results
Normal shunts	✔	✔	✔	✔	✘	✘	detrimental, more pronounced after LS,
Freckles	✔	✔	✔	✔	✘	✘	no shunts, electrically disconnected, intact absorber, may originate from difference in emissivity, independent of excitation and LS conditions,
Smears	✔	✔	✔	✔	✘	✘	centers=strong shunts, tails=no shunts (tails disappear after LS).
Doughnuts	✔	✔	✔	✔	✔	✔	weak shunts, most probably from the difference in the material properties caused by impurities, no LS effect

7. EL analysis of *a*-Si:H solar cells and modules

This chapter introduces a method to quantitatively analyze the EL images of hydrogenated amorphous silicon (a-Si:H) thin-film solar cells and modules. Based on this method, the radiative ideality factors and, consequently, the absolute local junction voltages of a-Si:H thin-film devices are determined.

7.1. Introduction

Up to this point, EL imaging has been used under the assumption that the reciprocity relation is valid. The validity of Eq. (2.29) implies the proportionality described in Eq. (2.30). However, Eq. (2.29) connects a small signal analysis close to thermodynamic equilibrium (the Q_e measurement), with a situation far from equilibrium (EL under voltage bias), such that the detailed balance arguments of Refs. [43, 44] are not necessarily valid. Especially, in materials with radiative recombination via shallow band tails or deep states, such as *a*-Si:H thin-film solar cells and modules or organic solar cells, these arguments are no more valid [142–146]. Thin-film silicon solar cells, especially those made from *a*-Si:H display a pronounced dependence of the spectral shape of their EL emission on the applied bias voltage. Such a behavior is not compatible with the reciprocity relation and Eq. (2.29) becomes pointless. This means that the evaluation method used for CIGS cannot be directly applied to *a*-Si:H devices. In such situations, the definition of a phenomenological radiative ideality factor n_r is necessary for the evaluation of EL images.

This chapter presents a method for extracting the absolute local junction voltage of *a*-Si:H thin-film solar cells and modules from electroluminescence (EL) images, where the electroluminescent emission follows a diode law with a phenomenological

radiative ideality factor n_r larger than one.

7.2. Determination of the local junction voltage

The determination of the absolute junction voltage of *a*-Si:H solar modules requires a modification of the standard reciprocal theorem described in Eq. (2.29) in Sec. 2.2. Since a change of the emission spectrum $\phi_{el}(\mathbf{r}, E, V_j)$ is not foreseen in Eq. (2.29), one has to use a modified equation for the detected EL signal

$$S_{cam}(\mathbf{r}) = \int Q_{cam}(E)\phi_{el}(\mathbf{r}, E, V_j)dE = S_0(\mathbf{r}) \exp\left(\frac{qV_j(\mathbf{r})}{n_r kT}\right). \tag{7.1}$$

Equation (7.1) serves as a phenomenological equation for the evaluation of EL images in non-ideal devices such as *a*-Si:H thin-film modules.

As shown by Müller in Refs. [144, 148] radiative recombination via tail states leads to an emission following

$$\int \phi_{el}(\mathbf{r}, E, V_j)dE \propto \exp\left(\frac{qV_j(\mathbf{r})}{n_r kT}\right), \tag{7.2}$$

where the radiative ideality factor depends on the characteristic energy of the tails. Thus for a spectrally flat quantum efficiency Q_{cam} of the camera, a radiative ideality factor is well defined. With a strongly spectral dependence of Q_{cam}, the radiative ideality factor n_r determined from spectrally intergrated measurements becomes dependent on Q_{cam} as will be shown below.

The derivation of the absolute junction voltage from EL images is subsequently described in the following steps.

Firstly, the absolute junction voltage V_j of each individual cell ($i = 1...N$) is calculated from Eq. (7.2) via

$$V_j = \frac{n_r kT}{q} \ln(S_{cam}) + V_{off} = n_r V_j'^{unc} + V_{off}, \tag{7.3}$$

where V_{off} denotes an unknown offset voltage (see Eq.(2.33)), and $V_j'^{unc}$ a relative voltage value that is directly obtained from the EL signal, but that is not corrected for V_{off} nor for the ideality factor n_r.

For a solar module with N cells connected in series, the total junction voltage V_{m} of the entire module is given by the sum

$$V_{\mathrm{m}} = n_{\mathrm{r}} \sum_{k=1}^{N} V_{\mathrm{j,k}}^{\prime \mathrm{unc}} + V_{\mathrm{off}} = n_{\mathrm{r}} V_{\mathrm{m}}^{\mathrm{unc}} + N V_{\mathrm{off}}, \tag{7.4}$$

where $V_{\mathrm{m}}^{\mathrm{unc}}$ is the sum over all values of $V_{\mathrm{j,i}}^{\prime \mathrm{unc}}$. Note that the offset voltage V_{off} is the same for all cells. The offset voltage V_{off} and the radiative ideality factor n_{r} are determined by comparing measurements of $V_{\mathrm{m}}^{\mathrm{unc}}$ carried out at different injected current densities J to the open circuit voltage V_{oc} of the module measured for a short circuit current density $J_{\mathrm{sc}} = J$ equaling the injected current density during the EL experiment. Because of

$$V_{\mathrm{oc}}|_{J_{\mathrm{sc}}=J} = V_{\mathrm{m}}|_{J=J_{\mathrm{sc}}} = n_{\mathrm{r}} V_{\mathrm{m}}^{\mathrm{unc}} + N V_{\mathrm{off}}, \tag{7.5}$$

adjustment of the J/V_{m} to the $J_{\mathrm{sc}}/V_{\mathrm{oc}}$ curves yields both, V_{off} and n_{r} values.

The determination of V_{off} and n_{r} for *a*-Si:H devices requires at least two $J_{\mathrm{sc}}/V_{\mathrm{oc}}$ pairs, which is different from the approach based on Eq. (2.34), where only one $J_{\mathrm{sc}}/V_{\mathrm{oc}}$ pair is needed to determine the offset voltage V_{off} [57] and $n_{\mathrm{r}} = 1$ is presumed a priori. Note that Eq. (7.5) does not strictly require that the superposition principle is valid as both V_{oc} and the junction voltage from EL are not affected by series resistance effects. The results in [148] indicate that the largest violations of the superposition principle of *a*-Si:H cells are in fact voltage dependent series resistance effects. Another assumption behind Eqs. (7.4) and (7.5) is that average current density through a cell versus the average voltage over the cell is the same as the local current density versus the local voltage. This is valid as long as the voltage differences over the cell are small enough to assume a linear relationship between the current density and the voltage.

The quantitative analysis method applied to *a*-Si:H thin-film solar cells and modules is presented as follows.

For the EL analysis, EL emission is recorded from single *a*-Si:H solar modules (10×10 cm^2) with the active area of (8×8 cm^2) using different cameras, namely, a full frame Si-CCD-camera and an InGaAs (chapter. 3). The investigated samples consist of eight series connected cell stripes with respective areas of (8×1 cm^2). Detailed information about the fabrication of the investigated *a*-Si:H samples was discussed in Sec. 2.3.2.

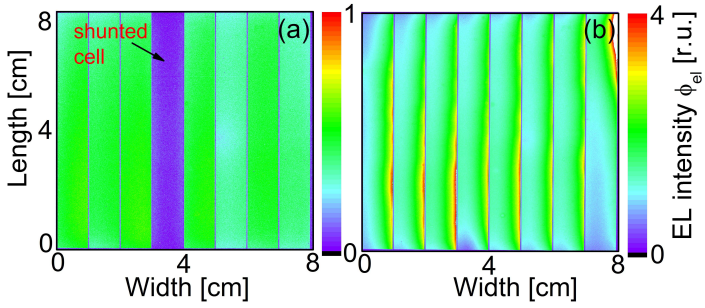

Figure 7.1.: EL images of an *a*-Si:H solar module (8×8 cm^2) recorded by a Si-CCD camera at: (a) low injection current density $J = 1.25$ mA/cm^2, (b) high injection current density $J = 15$ mA/cm^2. At low injection current density, the local EL intensity of the shunted cell is much lower compared to that of the non-shunted areas, whereas at high injection current density, the consequence of the series resistances of the contacts becomes more significant than that of the shunt.

For the determination of the absolute local junction voltage V_j, EL images of *a*-Si:H modules were recorded at different constant injection current densities J. Figures 7.1(a),(b) show EL images of an *a*-Si:H solar module (8×8 cm^2) measured with the Si-CCD camera at $J = 1.25$ mA/cm^2 and $J = 15$ mA/cm^2, respectively. The scales exhibit local EL intensities with arbitrary units. At low injection current density, the influence of shunts on the module performance is crucial. Even a weak shunt darkens the whole affected cell (see Fig. 7.1(a)). At higher injection current density, the impact of such a small shunt becomes negligible, but the effects of the series resistance become more prominent (see Fig. 7.1(b)). In general, the EL intensity becomes more inhomogeneous with increasing current densities due to the effects of series resistance. The series resistance of the front electrode typically results in a high intensity at the right side of the cell (near the P3 line) and a low intensity to the left. The local EL intensity within one cell becomes more inhomogeneous. The intensity variations in cell eight in Fig. 7.1(b) must be due to inhomogeneities in series resistance, as the EL signal from the same cell is homogeneous in Fig. 7.1(a).

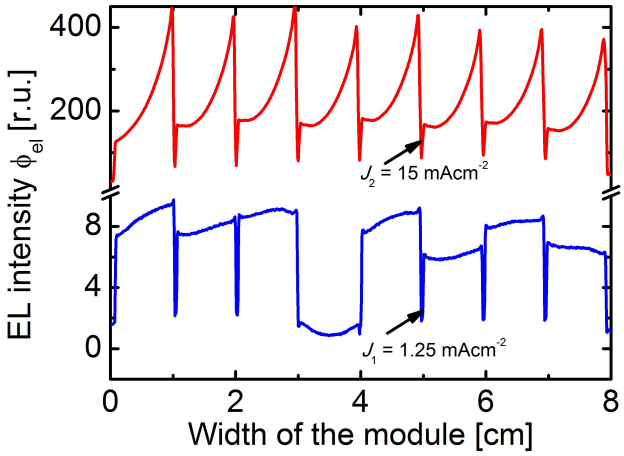

Figure 7.2.: EL line-scans obtained by averaging the entire length of the EL images recorded at different injection current densities $J = 1.25$ mA/cm^2 and $J = 15$ mA/cm^2.

Line-scans of the EL intensity shown in Fig. 7.2 are obtained from averaging the EL intensities over the entire length of EL images recorded at different injection current densities $J = 1.25$ mA/cm^2 and $J = 15$ mA/cm^2. At low injection current density, the EL line-scans illustrate that the EL intensity, and consequently the voltage difference of the shunted cell is very low. Furthermore, the deviation of the EL intensity between shunted and non-shunted cells is more pronounced. At high injection current density, the sheet resistance of the front ZnO contact is responsible for the increasing slope of the EL intensity within each cell. The sheet resistance of the back contact is much smaller than that of the front contact, therefore, the slope of the EL intensity is flat at the back contact of the cell.

Due to the fact that $n_\mathrm{r} \neq 1$, the calculation of V_m results successively from three steps demonstrated in Figs. 7.3.

Step one (Fig. 7.3(a)): The relative average junction voltage ($V'^{\mathrm{unc}}_{\mathrm{j,i}}$) of each individual cell i is calculated from the local EL intensity on Eq. (7.3), where n_r is

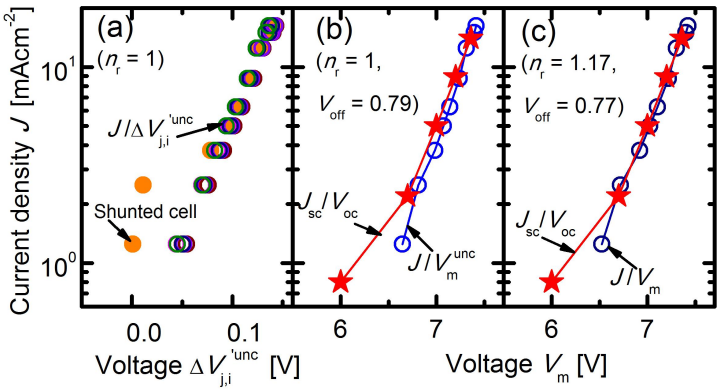

Figure 7.3.: Determination of the absolute junction voltage V_m, of the entire module in three steps. (a) ($n_r = 1$): $J/V_{j,i}^{'unc}$ curve of each individual cell. (b) ($n_r = 1$, $V_{off} = 0.79$ V): J/V_m^{unc} curve of the whole module (line with open circles), J_{sc}/V_{oc} curve (line with full stars). (c) ($n_r = 1.17$, $V_{off} = 0.77$ V): Corrected J/V_m curve (line with open circles) and J_{sc}/V_{oc} curve (full stars).

assumed to be one. At low injection based current density, the shunted cell (shown in Fig. 7.1(a)) depicts a significantly lower voltage compared to other unaffected cells.

Step two (Fig. 7.3(b)): The absolute junction voltage (V_m), which includes an offset voltage ($V_{off} = 0.79$ V), of the whole module is then calculated from Eq. (7.4), where n_r equals one. Subsequently, the J/V_m^{unc} characteristic (blue line with open circles) is fitted to the J_{sc}/V_{oc} characteristic (red line with full stars) to yield the radiative ideality factor $n_r = 1.17$ for the sample shown in Fig. 7.1.

Step three (Fig. 7.3(c)): The absolute junction voltage (V_m) is corrected by Eqs. (7.3) and (7.5) with $n_r = 1.17$ and $V_{off} = 0.77$ V. A good agreement between the J/V_m and J_{sc}/V_{oc} characteristics proves that the absolute junction voltage, and consequently the $J/V_{j,i}$ characteristics of each cell and of the whole module can be determined quantitatively from EL images. At low voltage, the shunted cell displayed in Fig. 7.1(a)) significantly affects the linear trend of the J_{sc}/V_{oc} characteristic.

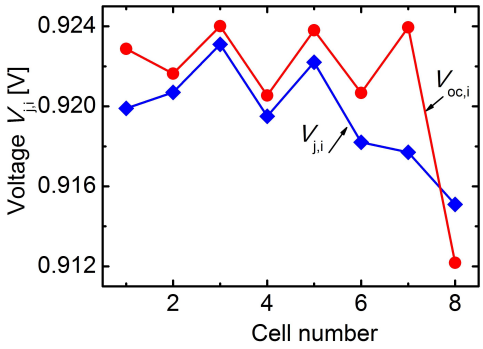

Figure 7.4.: The junction voltage of each individual cell ($V_{j,i}(J)$) (blue line with filled squares) results from the analysis described in Fig. 7.3. The open-circuit voltage of each individual cell ($V_{oc,i}(J_{sc})$) (red line with filled circles), which is independently measured with a class A solar simulator under standard test conditions (STC).

Figure 7.4 shows the open-circuit voltage of each individual cell ($V_{oc,i}(J_{sc})$) (red line with full circles), which is independently measured with a class A solar simulator under STC. The junction voltage of each individual cell ($V_{j,i}(J)$) (blue line with full squares) results from the analysis described in Fig. 7.3. Both the open-circuit voltage ($V_{oc,i}$) and the junction voltage ($V_{j,i}$) over the cell number exhibit the same trend. There is a small deviation (less than 4 mV) between the two voltages, where $V_{j,i}$ is smaller than $V_{oc,i}$ for all cells. This may result from a slight difference in the short-circuit current density J_{sc} for the V_{oc} measurement and the injection current density J for the EL measurement.

Finally, the local EL images with an arbitrary unit (see Figs. 7.1) can now be transformed into local junction voltage images with an absolute unit [V] (see Figs. 7.5(a),(b)), respectively. A good calibration of the absolute junction voltage using n_r and V_{oc} is obtained for both junction voltages of the whole module (see Fig. 7.3(c)) and of each individual cell (see Fig. 7.4). Note that the actual local junction voltage of the shunted cell that can be detected from EL at low injection

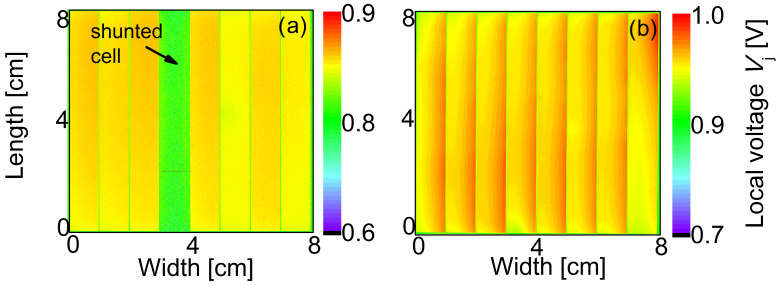

Figure 7.5.: Local junction voltage images calculated from EL images shown in Figs. 7.1 with the help of Eq. (7.2), respectively. (a) $J = 1.25$ mA/cm^2, (b) $J = 15$ mA/cm^2. The scales show the absolute value of the local junction voltage in [V].

current density $J = 1.25$ mA/cm^2 is limited by stray light (see Sect. 3.1). For this reason, the voltage in the shunted cell in Fig. 7.5(a) is beyond detection and, thus, overestimated. For the same reason, the effects of shunts are underestimated in the J/V_{m} curve as compared to the $J_{\mathrm{sc}}/V_{\mathrm{oc}}$ curve (see also Fig. 7.3(c)). However, the quantitative evaluation of the local absolute junction voltage of the shunted cell measured at high injection current density $J = 15$ mA/cm^2 and of non-shunted cells are almost unaffected by stray light.

Figure 7.6 shows EL spectra of different *a*-Si:H solar cells measured at room temperature ($T = 300$ K) and at different injection current densities J. Both samples A (open circles) and B (open triangles) show a dependency of the EL spectra on the injection current density, i.e. the ideality factor of the EL signal is wavelength dependent [147]. Figure 7.6 also shows the quantum efficiencies Q_{cam}(Si) and Q_{cam}(InGaAs) of the Si CCD and the InGaAs camera, respectively. The Si-CCD camera exhibits a strongly decreasing sensitivity towards lower photon energies having only a marginal overlap with the high energy end of the EL emission. In contrast, Q_{cam} of the InGaAs camera is roughly flat over the relevant spectral range of the EL emission of the *a*-Si:H devices.

In view of the different spectral sensitivities of the two camera systems, it is not surprising that the radiative ideality factor n_{r} resulting from an analysis with the

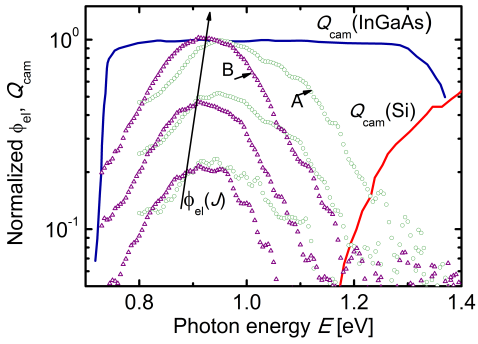

Figure 7.6.: EL spectra of two different *a*-Si:H solar cells A (open circles) and B (open triangles) at different injection current densities A: $J = [9.8, 5, 2]$ mA/cm^2, B: $J = [21, 9, 4.4]$ mA/cm^2. The external quantum efficiencies Q_{cam} of the Si and the InGaAs camera (solid lines) are also shown.

InGaAs camera differs significantly from that obtained by the Si-CCD for the same device. This work shows that ideality factors obtained from EL images recorded by the InGaAs camera are significantly higher than that from the Si-CCD. For instance, a value of $n_{\mathrm{r}} = 1.16$ is derived from the Si-CCD camera, whereas for the same device $n_{\mathrm{r}} = 1.32$ is obtained by using the InGaAs camera. This finding is consistent with the fact that radiative recombination via a band-to-defect mechanism taking place at lower photon energies has a higher n_{r} value than the high energy emission recorded by the Si-CCD device [144, 145].

Furthermore, the experimentally determined values of n_{r} vary from sample to sample by using the same camera, e.g., Si-CCD camera. It explains why the derived radiative ideality factor is influenced by the spectral sensitivity of the camera system used in the experiment. For the *a*-Si:H samples investigated in this thesis, the values of n_{r} of different samples range from 1.06 to 1.21 with the Si-CCD camera and from 1.26 to 1.32 with the InGaAs camera.

7.3. Summary

In this chapter, a method to quantitatively analyze the EL images of *a*-Si:H thin-film solar cells and modules is presented. The results from this analysis are presented below.

- The radiative ideality factors of the devices and, consequently, the absolute local junction voltage are determined from the EL images measured at different applied biases.
- It is shown that the measured n_{r} values depend on the sensitivity of the camera and vary from sample to sample.
- The applicability of the method to determine absolute junction voltages of individual cells in a module is not affected by the n_{r} value that is obtained for a particular system because the absolute junction voltage is calibrated to the measured $J_{\mathrm{sc}}/V_{\mathrm{oc}}$ characteristic.
- The method presented in this chapter can also be applied to the quantitative evaluation of EL images of other photovoltaic devices, which have radiative ideality factors $n_{\mathrm{r}} \neq 1$.

8. Conclusions and Outlook

This work presented various applications of EL imaging for the characterization of both CIGS and *a*-Si:H thin-film solar devices. The reciprocity theorem [43, 44] was validated for CIGS devices using EL and PL spectroscopy measurements. The results from this validation show that three of four requirements for the reciprocity theorem are met for CIGS solar devices. These are that the EL emission is proportional to the external quantum efficiency $Q_e(E)$, that the spectral shape of the EL and EM emission is unaltered at different bias conditions, and that the EL emission follows a diode law with a radiative ideality factor of unity. The fourth requirement, of a linear superposition of EL emission and EM emission was found to be valid only in a limited injection current density range. This range depends on history of the sample. For the samples investigated in this work, this linear superposition is valid for injection current densities below $J \leq 4\text{mAcm}^{-2}$ before light soaking and below $J \leq 15\text{mAcm}^{-2}$ after light soaking. EL images in this work were measured at an injection range of 20 mAcm^{-2} to 35 mAcm^{-2}. However, the quantitative analysis of the images is still valid because the calculated junction voltage from EL images is adjusted to the device J_{sc}/V_{oc} curves. Following this conclusion, EL images of CIGS solar cells and modules were then quantitatively analyzed based on the reciprocity theorem. The effect of metastability on the EL intensity was investigated and quantitatively analyzed. The analysis showed that the increase of the EL intensity during the irradiation time is due to the decrease of the bulk series resistance and the increase of the junction series resistance. The metastable effect on the resistivity and recombinatoric properties of the solar modules were distinguished from each other. It was found that the change in the bulk series resistance is much larger than that of the junction series resistance and therefore, that the bulk resistance strongly affects the quantitative evaluation of EL images.

A method which combines EL and LIT imaging for the analysis of shunts in

CIGS solar modules was developed. The cross-talk effect, whereby a shunt affects neighboring, non-shunted cells in a module, was observed in EL images, and explained by using a simulation model with NSM and SPICE. The results from the investigation of the effect showed that the cross-talk strongly depends on the sheet resistances of the front and back electrodes, the shunt current and the cell geometry. Furthermore, the simulation model yields information on the sheet resistances, the bulk series resistance, and the shunt resistances of CIGS solar cells and modules.

EL imaging was used to classify several common defects found in CIGS modules, namely, standard shunts, Smears, Freckles, and Doughnuts. The results of this study showed that the standard shunts significantly affect the device performance and can have various origins. Freckles are electrically isolated defects. The absorber material of the Freckles is unaffected. Freckles most probably result from the difference in emissivity of the materials, and may reduce the short circuit current and the efficiency of the device. Smears contain two electrically different sections. The center of the Smears are strong shunts, and the tails are not electrically active. Doughnuts are weak shunts, which can have varied appearances in EL images, and may result from a difference in the material properties or impurities at the site of the Doughnut compared to the normal region of the cell.

A method for quantitatively determining the local junction voltage of *a*-Si:H solar devices, which have a radiative ideality factor greater than one, was demonstrated. The value of the radiative ideality factor depends on the spectral sensitivity of the camera used for the experiments, as well as on the investigated samples.

The various applications of EL imaging presented in this thesis demonstrate that EL imaging is a powerful tool for the investigation of thin-film solar cells. Among other things, it can be used to evaluate metastable changes, various resistivities, recombination processes, and a number of electrically varying defects in CIGS devices. Quantitative analysis of *a*-Si:H solar devices from EL images has been demonstrated. From this analysis of EL images, better knowledge about the physical, optical, as well as electrical properties of different solar technologies was gained. Deeper understanding about different loss mechanisms and the origins of defects will lead to an improvement of the efficiency of solar cells and modules.

The work in this thesis can be extended in the future to yield even more understanding of the physics of thin-film devices. A 1D model used for this analysis

of the cross-talk in chapter 5 is well suited to understand the effects of the parallel resistance of the front and back electrodes. However, this model is insufficient to explain the effects of the ratio between the sheet resistances. In future work, a full 2D problem must be considered to understand these influences. Several common defects in CIGS solar cells and modules were classified in detail, however, the origins of the defects were not investigated. Further investigation of the origins of the defects will lead to the improvement of the device performance.

A. Effects of shunt position on cross-talk

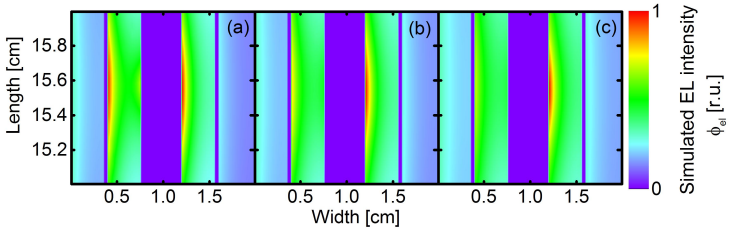

Figure A.1.: (a) Simulated EL image when the shunts are shifted close to the left edge of the shunted cell. (b) Simulated EL image when the shunts are in the middle of the shunted cell (original position). (c) Simulated EL image when the shunts are shifted close to the right edge of the shunted cell. The input parameters are given in Tab. 5.2, and $R_{\mathrm{Mo}} = 1.3\ \Omega_{\mathrm{sq}}$, $R_{\mathrm{ZnO}} = 18\ \Omega_{\mathrm{sq}}$, and $R_{\mathrm{s}} = 0.02\ \Omega\mathrm{cm}^2$.

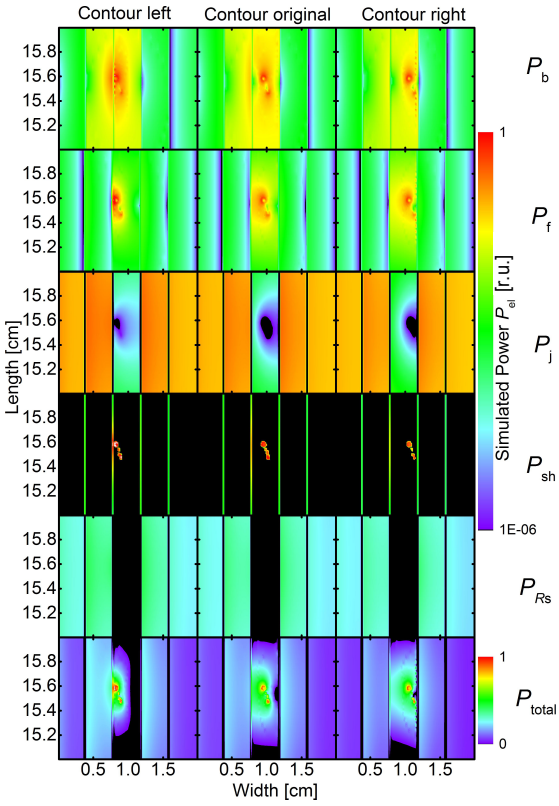

Figure A.2.: Simulated power density images with change in shunt position. The three columns represent the power density images resulting from simulations, in which the shunts are shifted from the original position of the shunts, to the left edge of the shunted cell, and the right edge of the shunted cell. The six rows present the resulting power density images of the back Mo electrode P_{b}, of the front ZnO electrode P_{f}, of the junction P_{j}, of the shunts P_{sh}, of the bulk series resistance P_{Rs}. The last row shows the total power density images, which is the sum of all power density images mentioned above. Note that these total power density images are comparable to the measured DLIT images at the same injection current density. The input parameters are given in Tab. 5.2, and $R_{\mathrm{Mo}} = 1.3\ \Omega_{\mathrm{sq}}$, $R_{\mathrm{ZnO}} = 18\ \Omega_{\mathrm{sq}}$, and $R_{\mathrm{s}} = 0.02\ \Omega\mathrm{cm}^2$.

B. List of Publications related to this work

1. T. M. H. Tran, B. E. Pieters, M. Siegloch, A. Gerber, C. Ulbrich, T. Kirchartz, and U. Rau, *Characterization of shunts in Cu(In,Ga)Se₂ solar modules via combined EL and DLIT analysis*, Proceedings of the 26th EUPVSEC, 2981 (2011)

2. T. M. H. Tran, B. E. Pieters, M. Schneemann, R. Schäffler, A. Gerber, and U. Rau, *Classification of defects in Cu(In,Ga)Se₂ solar cells and modules using electroluminescence and thermography techniques*, Proceedings of the 27th EUPVSEC, 2372 (2012)

3. T. M. H. Tran , B. E. Pieters , C. Ulbrich, A. Gerber, T. Kirchartz, and U. Rau, *Transient phenomena in Cu(In,Ga)Se₂ solar modules investigated by electroluminescence imaging*, Thin Solid Films **535**, 307 (2013)

4. T. M. H. Tran, B. E. Pieters, M. Schneemann, T. C. M. Müller, A. Gerber, T. Kirchartz, and U. Rau, *Local junction voltages and radiative ideality factors of* a-*Si:H solar modules determined by electroluminescence imaging*, MRS Proceedings, **1536**, 105 (2013)

5. T. M. H. Tran, B. E. Pieters, M. Schneemann, T. C. M. Müller, A. Gerber, T. Kirchartz, and U. Rau, *Quantitative evaluation method for electroluminescence images of a-Si:H thin-film solar modules*, Phys. Status Solidi RRL, **7**, 627 (2013)

6. U. Rau, T. C. M. Müller, T. M. H. Tran, B. E. Pieters, and A. Gerber, *Electroluminescence of Cu(In,Ga)Se₂ solar cells and modules*, MRS Proceedings, **1538**, 133 (2013)

7. T. C. M. Müller, T. M. H. Tran, B. E. Pieters, A. Gerber, R. Carius, and U. Rau, *Effect of light soaking on the electro- and photoluminescence of Cu(In,Ga)Se₂ solar cells* , Appl. Phys. Lett., **103**, 183504 (2013)

C. Curriculum vitae

Education

1989-1994	Primary school, Hung Yen-Vietnam
1994-1997	Secondary school, Hanoi-Vietnam
1998-2000	Highschool, Hanoi-Vietnam
2000-2004	Gymnasium, Lippstadt-Germany
5/2004	Abitur am Gymnasium Schloss Overhagen in Lippstadt
10/2004-6/2010	Studies of Electrical Engineering and Information Technology at RWTH Aachen University
3/2007	Vordiplom
3/2007-3/2009	Hauptstudium, main subject: Electrical Engineering and Electronics
10/2007	Student thesis: "Analyse von Solarenergiezeitreihen und Implementierung eines Verfahrens zur Ermittlung von Solarenergiezeitreihen mit MS Access und Visual Basic" at Institut für Elektrische Anlage und Energiewirtschaft
10/2010-6/2010	Diploma thesis at Institut für Energie und Klimaforschung IEK-5 Photovoltaics, Forschungszentrum Jülich GmbH Title: "Electroluminescence analysis of Cu(In,Ga)Se_2 thin-film solar cells and modules"
6/2010	Diploma at RWTH Aachen University

Work experience

6/2004-8/2004	Internship at Hella KGaA in Lippstadt
12/2008-2/2009	Student assistant at Institut für Stromrichtertechnik und Elektrische Antriebe
3/2009-8/2009	Internship at Solland Solar Cells BV in Aachen/Heerlen

Professional Experience

10/2010-12/2013	PhD student at the IEK-5 Photovoltaics
01/2014-now	Postdoc at the IEK-5 Photovoltaics

Bibliography

[1] http://www.eia.gov/forecasts/ieo/, *International Energy Outlook 2013*.

[2] P. Crompton and Y. Wu, Energ. Econ. **27**, 195 (2005).

[3] I. E. A. (IEA), IEA Paris, France (2012).

[4] http://www.map.ren21.net/GSR/GSR2012.pdf, *Renewables 2012 Global Status Report*.

[5] J. A. Turner, Science **285**, 687 (1999).

[6] A. Sayigh, Appl. Energy **64**, 15 (1999).

[7] S. R. Bull, Proc. IEEE conference **89**, 1216 (2001).

[8] F. I. F. E. ISE, *Photovoltaics Report* (2012).

[9] W. Shockley and H. J. Queisser, J. Appl. Phys. **32**, 510 (1961).

[10] M. A. Green, K. Emery, Y. Hishikawa, W. Warta, and E. D. Dunlop, Prog. Photovolt. Res. Appl. **20**, 12 (2011).

[11] J. Zhao, A. Wang, and M. A. Green, Sol. Energy Mater. Sol. Cells **65**, 429 (2001).

[12] A. Morales-Acevedo, Sol. Energy **80**, 675 (2006).

[13] N. G. Dhere, Sol. Energy Mater. Sol. Cells **95**, 277 (2011).

[14] T. Razykov, C. Ferekides, D. Morel, E. Stefanakos, H. Ullal, and H. Upadhyaya, Sol. Energy **85**, 1580 (2011).

[15] P. Jackson, D. Hariskos, E. Lotter, S. Paetel, R. Wuerz, R. Menner, W. Wischmann, and M. Powalla, Prog. Photovolt. Res. Appl. **19**, 894 (2011).

[16] http://www.fast-track.eu/news/new-world-record-solar-cell-device .html.

[17] http://www.solarserver.com/solar-magazine/solar-news/current/2013/kw43/zsw-produces-world-record-thin-film-solar-pv-cell-achieves-208-efficiency-and-overtakes-multi-crystalline-silicon technology.html.

[18] M. Powalla and B. Dimmler, Sol. Energy Mater. Sol. Cells **67**, 337 (2001).

[19] M. Powalla and B. Dimmler, Thin Solid Films **387**, 251 (2001).

[20] M. Powalla, G. Voorwinden, D. Hariskos, P. Jackson, and R. Kniese, Thin Solid Films **517**, 2111 (2009).

[21] W. Fang and K. Ito, SIAM J. Appl. Math. **52**, 1611 (1992).

[22] H. J. Möller, M. Rinio, and M. Werner, Solid State Phenom. **63**, 115 (1998).

[23] P. Edwards, S. Galloway, and K. Durose, Thin Solid Films **372**, 284 (2000).

[24] M. Sch öfthaler and R. Brendel, J. Appl. Phys. **77**, 3162 (1995).

[25] A. Van der Heide, J. Bultman, J. Hoornstra, and A. Schönecker, Sol. Energy Mater. Sol. Cells **74**, 43 (2002).

[26] J. Carstensen, G. Popkirov, J. Bahr, and H. Föll, Sol. Energy Mater. Sol. Cells **76**, 599 (2003).

[27] O.Breitenstein and M. Langenkamp, *Lock-in Thermography* (Springer Verlag Heidelberg New York, 2003).

[28] K. Bothe, G. H. Bauer, and T. Unold, Thin Solid Films **403**, 453 (2002).

[29] T. Trupke, R. A. Bardos, M. C. Schubert, and W. Warta, Appl. Phys. Lett. **044107**, 1 (2006).

[30] T. Fuyuki, H. Kondo, T. Yamazaki, Y. Takahashi, and Y. Uraoka, Appl. Phys. Lett. **86**, 262108 (2005).

[31] D. Hinken, K. Ramspeck, K. Bothe, and R. Fischer, B.and Brendel, Appl. Phys. Lett. **91**, 182104 (2007).

[32] K. Ramspeck, K. Bothe, D. Hinken, B. Fischer, J. Schmidt, and R. Brendel, Appl. Phys. Lett. **90**, 1 (2007).

[33] P. Würfel, T. Trupke, T. Puzzer, E. Schäffer, W. Warta, and S. W. Glunz, J. Appl. Phys. **101**, 123110 (2007).

[34] K. Bothe, K. Ramspeck, D. Hinken, C. Schinke, J. Schmidt, S. Herlufsen, R. Brendel, J. Bauer, J. M. Wagner, N. Zakharov, and O. Breitenstein, J. Appl. Phys. **106**, 104510 (2009).

[35] J. Haunschild, M. Glatthaar, M. Kasemann, and E. R. Rein, S.and Weber, Phys. Status Solidi RRL **3**, 227 (2009).

[36] T. Potthoff, K. Bothe, U. Eitner, D. Hinken, and M. Koentges, Prog. Photovolt. Res. Appl. **18**, 100 (2010).

[37] U. Rau, T. Kirchartz, A. Helbig, and B. E. Pieters, MRS Online Proceedings Library **1165** (2009).

[38] A. Helbig, T. Kirchartz, R. Schäffler, J. H. Werner, and U. Rau, Sol. Energy Mater. Sol. Cells **94**, 979 (2010).

[39] M. Paire, L. Lombez, J. Guillemoles, and D. Lincot, Thin Solid Films **519**, 7493 (2011).

[40] F. Runai, F. Schwäble, T. Walter, A. Fidler, S. Gorse, T. Hahn, and I. Kötschau, in *Proc. of the 37th IEEE Photovoltaic Specialists Conference*, IEEE, Seattle (2011), p. 003399.

[41] K. Vandewal, K. Tvingstedt, A. Gadisa, O. Inganäs, and J. V. Manca, Nat. Mater. **8**, 904 (2009).

[42] M. Bokalič, U. O. Krašovec, and M.Topič, Prog. Photovolt. Res. Appl. (2012).

[43] U. Rau, Phys. Rev. B **76**, 085303 (2007).

[44] U. Rau, IEEE J. Photovolt. **2**, 169 (2012).

[45] B. Pieters, IEEE J. Photovolt. **1**, 93 (2011).

[46] G. Kirchhoff, Ann. Physik **19**, 275 (1860).

[47] M. Planck, *Vorlesungen über die Theorie der Wärmestrahlung* (Johann Ambrosius Barth, 1921).

[48] P. Wuerfel, J. Phys. C **15**, 3967 (1982).

[49] U.Rau, *Photovoltaic lectures* (2013).

[50] K. Orgassa, *The Role of the Heterointerfaces in the Cu(In,Ga)Se₂ Thin Film Solar Cell with Chemical Bath Deposited Buffer Layers*, Ph.D. thesis, Universitaet Stuttgart (2004), p. 82.

[51] B. Dimmler, H. Dittrich, R. Menner, and H. Schock, in *Proc. of the 19th IEEE Photovoltaic Specialists Conference*, IEEE, New Orleans (1987), p. 1454.

[52] W. Chen, J. Stewart, B. Stanbery, W. Devaney, and R. Mickelsen, in *Proc. of the 19th IEEE Photovoltaic Specialists Conference*, IEEE, New Orleans (1987), p. 1445.

[53] U. Rau and H. Schock, Appl. Phys. A **69**, 131 (1999).

[54] P. Wuerfel, *Physik der Solarzelle* (Spektrum Akademischer Verlag, Heidelberg, Berlin, 2000), p. 65.

[55] W. van Roosbroeck and W. Shockley, Phys. Rev. **94**, 1558 (1954).

[56] S. M. Sze, *Physics of Semiconductor Devices, 2nd Edition* (Wiley, New York, 1981).

[57] T. Kirchartz, U. Rau, M. Hermle, A. W. Bett, A. Helbig, and J. Werner, Appl. Phys. Lett. **92**, 123502 (2008).

[58] T. Kirchartz and U. Rau, J. Appl. Phys. **102**, 104510 (2007).

[59] C. Donolato, Appl. Phys. Lett. **46**, 270 (1985).

[60] T. Kirchartz, U. Rau, M. Kurth, J. Mattheis, and J. Werner, Thin Solid Films **515**, 6238 (2007).

[61] T. Kirchartz, A. Helbig, W. Reetz, M. Reuter, J. H. Werner, and U. Rau, Prog. Photovolt. Res. Appl. **17**, 394 (2009).

[62] S. Roensch, R. Hoheisel, F. Dimroth, and A. W. Bett, Appl. Phys. Lett. **98**, 251113 (2011).

[63] M. Ruckh, D. Schmid, M. Kaiser, R. Schäffler, T. Walter, and H. Schock, Sol. Energy Mater. Sol. Cells **41**, 335 (1996).

[64] C. Heske, R. Fink, E. Umbach, W. Riedl, and F. Karg, Appl. Phys. Lett. **68**, 3431 (1996).

[65] B. M. Keyes, F. Hasoon, P. Dippo, A. Balcioglu, and F. Abulfotuh, in *Conference Record of the 26th IEEE Photovoltaic Specialists Conference*, IEEE, Anaheim (1997), p. 479.

[66] U. Rau, M. Schmitt, F. Engelhardt, O. Seifert, J. Parisi, W. Riedl, J. Rimmasch, and F. Karg, Solid State Commun. **107**, 59 (1998).

[67] D. Rudmann, A. F. da Cunha, M. Kaelin, F. Kurdesau, H. Zogg, A. Tiwari, and G. Bilger, Appl. Phys. Lett. **84**, 1129 (2004).

[68] W. Shafarman and J. Phillips, in *Conference Record of the 25th IEEE Photovoltaic Specialists Conference*, IEEE, Washington (1996), p. 917.

[69] T. Wada, N. Kohara, T. Negami, and M. Nishitani, Jpn. J. Appl. Phys. **35**, 1253 (1996).

[70] N. Kohara, S. Nishiwaki, Y. Hashimoto, T. Negami, and T. Wada, Sol. Energy Mater. Sol. Cells **67**, 209 (2001).

[71] K. Orgassa, H. W. Schock, and J. Werner, Thin Solid Films **431-432**, 387 (2003).

[72] L. Assmann, J. Bernède, A. Drici, C. Amory, E. Halgand, and M. Morsli, Appl. Surf. Sci. **246**, 159 (2005).

[73] E. Takahashi, S. Pethe, and N. Dhere, in *Proc. of the 35th IEEE Photovoltaic Specialists Conference*, IEEE, Honolulu (2010), p. 002478.

[74] R. Mickelsen and W. S. Chen, Appl. Phys. Lett. **36**, 371 (1980), US-Patent 4,335,266, 1982.

[75] A. M. Gabor, J. R. Tuttle, D. S. Albin, M. A. Contreras, R. Noufi, and A. M. Hermann, Appl. Phys. Lett. **65**, 198 (1994).

[76] J. Kessler, K. Velthaus, M. Ruckh, R. Laichinger, H. Schock, D. Lincot, R. Ortega, and J. Vedel, in *Proceedings of the 6th International Photovoltaic Science and Engineering Conference* (1992), p. 1005.

[77] T. Friedlmeier, D. Braunger, D. Hariskos, M. Kaiser, H. Wanka, and H. Schock, in *Proc. 25th IEEE Photovolt. Spec. Conf.*, IEEE (1996), p. 845.

[78] U. Rau and M. Schmidt, Thin Solid Films **387**, 141 (2001).

[79] B. Dimmler, M. Powalla, and R. Schaeffler, in *Proc. of the 31st IEEE Photovoltaic Specialists Conference*, IEEE, New York (2005), p. 189.

[80] B. Rech, T. Roschek, J. Mu, S. Wieder, and H. Wagner, Sol. Energy Mater. & Sol.Cells **66**, 267 (2001).

[81] T. Zimmermann, A. J. Flikweert, T. Merdzhanova, J. Woerdenweber, A. Gordijn, U. Rau, F. Stahr, K. Dybek, and J. W. Bartha, Prog. Photovoltaics Res. Appl. (2012).

[82] A. Madan and S. Morrison, Sol. Energy Mater. Sol. Cells **55**, 127 (1998).

[83] A. Mahan, Y. Xu, E. Iwaniczko, D. Williamson, B. Nelson, and Q. Wang, J. Non-Cryst. Solids **299**, 2 (2002).

[84] S. Morrison, U. Das, and A. Madan, Sol. Energy Mater. Sol. Cells **76**, 281 (2003).

[85] D. Abou-Ras, T. Kirchartz, and U. Rau, *Advanced Characterization Techniques for Thin Film Solar Cells* (Wiley-VCH Verlag GmbH & Co. KGaA, 2011).

[86] http://www.keithley.com/products/dcac/specialtysystems/optoelectronics/?mn=2420.

[87] http://www.ccd.com/alta_f9000.html.

[88] http://www.princetoninstruments.com/products/imcam/nirvana/.

[89] D. Walter, A. Liu, E. Franklin, D. Macdonald, B. Mitchell, and T. Trupke, in *Proc.of the 38th Photovoltaic Specialists Conference*, IEEE, Austin (2012), p. 000307.

[90] J. Adams, A. Vetter, F. Hoga, F. Fecher, J. Theisen, C. Brabec, and C. Buerhop-Lutz, *The influence of defects on the cellular open circuit voltage in CuInGaSe2 thin film solar modules - an illuminated lock-in thermography study*, Under submission.

[91] C. S. Hsu, Handbook of instrumental techniques for analytical chemistry **249** (1997).

[92] J. Bauer, O. Breitenstein, and J. Wagner, Electronic Device Failure Analysis **3**, 6 (2009).

[93] O. Breitenstein, J. P. Rakotoniaina, and M. H. A. Rifai, Prog. Photovolt. Res. Appl. **11**, 515 (2003).

[94] O. Breitenstein, J. P. Rakotoniaina, M. H. Al Rifai, and M. Werner, Prog. Photovolt. Res. Appl. **12**, 529 (2004).

[95] J. Isenberg and W. Warta, Prog. Photovolt. Res. Appl. **12**, 339 (2004).

[96] O. Breitenstein and J. P. Rakotoniaina, J. Appl. Phys. **97**, 074905 (2005).

[97] J. Isenberg, A. Van Der Heide, and W. Warta, Prog. Photovolt. Res. Appl. **13**, 697 (2005).

[98] I. Beckers, Thin Solid Films **431-432**, 205 (2003).

[99] L. Gütay and G. Bauer, Thin Solid Films **515**, 6212 (2007).

[100] S. Shirakata and T. Nakada, Phys. Status Solidi C **6**, 1059 (2009).

[101] S. Johnston, T. Unold, I. Repins, R. Sundaramoorthy, K. M. Jones, B. To, N. Call, and R. Ahrenkiel, J. Vac. Sci. Technol., A **28**, 665 (2010).

[102] T. Ott, F. R. Runai, F. Schwaeble, and T. Walter, Prog. Photovolt: Res. Appl. **20**, 600 (2012).

[103] M. Igalson and H. W. Schock, J. Appl. Phys. **80**, 5765 (1996).

[104] F. Engelhardt, M. Schmidt, T. Meyer, O. Seifert, J. Parisi, and U. Rau, Phys. Lett. A **245**, 489 (1998).

[105] U. Rau, M. Schmitt, J. Parisi, W. Riedl, and F. Karg, Appl. Phys. Lett. **73**, 223 (1998).

[106] P. Zabierowski, U. Rau, and M. Igalson, Thin Solid Films **387**, 147 (2001).

[107] T. Meyer, F. Engelhardt, J. Parisi, and U. Rau, J. Appl. Phys. **91**, 5093 (2002).

[108] J. T. Heath, J. Appl. Phys. **95**, 1000 (2004).

[109] M. N. Ruberto and A. Rothwarf, J. Appl. Phys. **61**, 4662 (1987).

[110] U. Rau, M. Turcu, and A. Jasenek, Thin Solid Films **515**, 6243 (2007).

[111] M. Igalson, P. Zabierowski, D. Przado, M. Urbaniak, A.and Edoff, and W. N. Shafarman, Sol. Energy Mater. Sol. Cells **93**, 1290 (2009).

[112] U. Rau, A. Jasenek, R. Herberholz, H.-W. Schock, J.-F. Guillemoles, D. Lincot, and L. Kronink, in *Proc. 2nd World Conf. on Photovolt. Energy Con.* (1998), p. 428.

[113] M. Igalson, M. Bodeg å rd, and L. Stolt, Sol. Energy Mater. Sol. Cells **80**, 195 (2003).

[114] D. L. Staebler and C. R. Wronski, Appl. Phys. Lett. **31**, 292 (1977).

[115] M. Stutzmann, W. Jackson, A. Smith, and R. Thompson, Appl. Phys. Lett. **48**, 62 (1986).

[116] D. Willett and S. Kuriyagawa, in *Proc. of the 23rd IEEE Photovoltaic Specialists Conference*, IEEE, Louisville (1993), p. 495.

[117] R. Kniese, M. Powalla, and U. Rau, Thin Solid Films **515**, 6163 (2007).

[118] R. Scheer and H.-W. Schock, *Chalcogenide Photovoltaics: Physics, Technologies, and Thin Film Devices* (John Wiley & Sons, 2011).

[119] M. Igalson, M. Cwil, and M. Edoff, Thin Solid Films **515**, 6142 (2007).

[120] S. Siebentritt and T. Rissom, Appl. Phys. Lett. **92**, 062107 (2008).

[121] S. Lany and A. Zunger, Phys. Rev. Lett. **100**, 016401 (2008).

[122] S. Lany and A. Zunger, J. Appl. Phys. **100**, 113725 (2006).

[123] a. Urbaniak and M. Igalson, Thin Solid Films **517**, 2231 (2009).

[124] S. Siebentritt, M. Igalson, C. Persson, and S. Lany, Prog. Photovolt. Res. Appl. **18**, 390 (2010).

[125] T. Müller, T. Tran, B. Pieters, A. Gerber, R. Carius, and U. Rau, Applied Physics Letters **103**, 183504 (2013).

[126] M. Eron and A. Rothwarf, Appl. Phys. Lett. **44**, 131 (1984).

[127] M. Kasemann, M. C. Schubert, M. The, M. Köber, M. Hermle, and W. Warta, Appl. Phys. Lett. **89**, 224102 (2006).

[128] O. Breitenstein, J. Bauer, and J. P. Rakotoniaina, Semiconductors **41**, 440 (2007).

[129] M. Kasemann, D. Grote, B. Walter, W. Kwapil, T. Trupke, Y. Augarten, R. Bardos, E. Pink, M. Abbott, and W. Warta, Prog. Photovoltaics Res. Appl. **16**, 297 (2008).

[130] O. Breitenstein, J. Bauer, T. Trupke, and R. A. Bardos, Prog. Photovolt. Res. Appl. **16**, 325 (2008).

[131] Y. Augarten, T. Trupke, M. Lenio, J. Bauer, O. Breitenstein, J. Weber, and R. Bardos, in *Proc. 25th Eur. Photovoltaic Solar Energy Conf. Exhib* (2009), p. 29.

[132] Y. Augarten, T. Trupke, M. Lenio, J. Bauer, J. W. Weber, M. Juhl, M. Kasemann, and O. Breitenstein, Prog. Photovolt. Res. Appl. **21**, 933 (2012).

[133] S. Johnston, I. Repins, N. Call, R. Sundaramoorthy, K. M. Jones, and B. To, in *Proc. of the 35th IEEE Photovoltaic Specialists Conference*, IEEE, Honolulu (2010), p. 001727.

[134] G. Brown, A. Pudov, B. Cardozo, V. Faifer, E. Bykov, and M. Contreras, J. Appl. Phys. **108**, 074516 (2010).

[135] http://getdata-graph digitizer.com/.

[136] U. Rau, P. O. Grabitz, and J. H. Werner, Applied Physics Letters **85**, 6010 (2004).

[137] O. Breitenstein et al., in *Proceedings of the 17th NREL Workshop on Crystalline Silicon Solar Cells and Modules: Materials and Processes* (2007), p. 61.

[138] M. Kasemann, D. Grote, B. Walter, W. Kwapil, T. Trupke, Y. Augarten, R. A. Bardos, and E. Pink, Prog. Photovoltaics Res. Appl. **16**, 297 (2008).

[139] J. Raguse, J. McGoffin, and J. Sites, in *Proc. of the 38th IEEE Photovoltaic Specialists Conference*, IEEE, Austin (2012), p. 000448.

[140] S. Johnston, T. Unold, I. Repins, A. Kanevce, K. Zaunbrecher, F. Yan, J. V. Li, P. Dippo, R. Sundaramoorthy, K. M. Jones, and B. To, J. Vac. Sci. Technol., A **30**, 04D111 (2012).

[141] T. Kirchartz, U. Rau, M. Kurth, J. Mattheis, and J. H. Werner, Thin Solid Films **515**, 6238 (2007).

[142] R. S. Crandall, J. Appl. Phys. **53**, 3350 (1982).

[143] R. A. Street, D. K. Biegelsen, and R. L. Weisfield, Phys. Rev. B **30**, 5861 (1984).

[144] T. C. M. Müller, B. E. Pieters, T. Kirchartz, R. Carius, and U. Rau, Phys. Status Solidi C **9**, 1963 (2012).

[145] T. C. M. Müller, B. E. Pieters, T. Kirchartz, and U. Rau, J. Appl. Phys. **113**, 134503 (2013).

[146] W. Gong, M. A. Faist, N. J. Ekins-Daukes, Z. Xu, D. D. C. Bradley, J. Nelson, and T. Kirchartz, Phys. Rev. B **86**, 024201 (2012).

[147] B. Pieters, T. Kirchartz, T. Merdzhanova, and R. Carius, Sol. Energy Mater. Sol. Cells **94**, 1851 (2010).

[148] T. Müller, *Light absorption and radiative recombination in thin-film solar cells*, Ph.D. thesis, RWTH Aachen (2013), Unpublished, pp.104-107.

Acknowledgements

It would be impossible for me to finish this thesis without help of supervisors, colleagues, friends and family. Writing this sentence, I suddenly remember a saying 'Remember the kindness of others. Repay the kindness with gratitude'. Therefore, it is a great pleasure for me to express my deep thankfulness to

Prof. Dr. Uwe Rau for giving me the opportunity to work and finish my thesis at his institute, for his interest, his advice, his support and his ingenious ideas.

Prof. Dr. Susanne Siebentritt for her interest in my work, for being my mentor and for kindly accepting the co-report of this thesis.

Dr. Bart Pieters for his supervision, his simulation programs, his patient, informative and interesting discussions and explanations of many physical phenomena, without his scientifical support this work would have been impossible.

Dr. Andreas Gerber for his supervision, his scientifical support, his sense of humor, his enthusiasm, encouragement and his support wherever needed.

Dr. Thomas Kirchartz and Dr. Carolin Ulbrich, Dr. Yael Augarten for their scientifical support and for their proofreading of my papers and my thesis.

Dr. Matthias Schneemann for his microscopic EL and PL measurements and his proofreading of my thesis,

Christoph Zahren, Lars Nießen, Carsten Grates, Wilfried Reetz, Hans-Peter Bochem, Elma Neumann for their technical support and for the IV, EQE, SEM, and EDX measurements.

Thomas Müller and Max Siegloch for the spectral EL and PL measurements and for introducing to me the LIT measurement method.

Joachim Kirchhoff, and Ulrike Gerhards for preparing the *a*-Si:H samples.

Dr. Raymund Schäffler, Dr. Claudia Buerhoff, Jean-Patrick Theisen and all other project members of the project 'FKZ0325149B (PV-IR-EL)' for the interesting project meetings and good collaboration.

Jean-Patrick Theisen and Boris Misic for the preparation of the samples used in this thesis.

Grabrielle Jost, Carolin Ulbrich, Marek Warzecha, Max Siegloch, David Wippler, Juri Hotovy, Etienne Moulin, Lihong Xiao, Wanjiao Böttler, Kaining Ding, Tina Leidinger, Anna Heindt, Simone Bugdol, Matthias Müller, Matthias Schneemann, Stephan Lehnen, Markus Ermes, Tsvetelina Merdzhanova, and all other members of IEK-5 for being my colleagues, my friends, for giving me a pleasant, meaningful and happy time during my work.

My parents Tran Minh Tuoc and Pham Thi He who gave me a chance to come to visit this wonderful world, raised me up, always love me, support me, and believe in me. Father, without you it would have been impossible for me to come to Germany and to have this great chance to develop myself. Mother, if I was allowed to say just one sentence, I would say 'Mama, I have already found the greatest happiness because the greatest love of all comes from you.'

My Uncle Vu Hai Nau for his care, his support, his advice, his encouragement, for sharing with me the good time as well as the difficult time, without him it would have been impossible for me to stay in Germany, to go to school, to finish my study and my thesis now. I am always grateful for all the things you did and still do for me.

My grandparents and all of my relatives in Vietnam for loving me, having taken care of me and having taught me a lot about life. Grandmothers, you were always an example of compassion, generosity, diligence, and courage for me. Grandfather, I will never forget your sayings and your wisdom. Wherever I may go, I will carry them with me and practice them.

My second mother Frau Erika de Gil and her family for teaching me not only

the German language but also a lot about German traditions, for her care and her support all the last thirteen years.

My school teachers Herr Josef Schulte, Herr Heinz Gesterkamp, Herr Peter Hoffmann and all other teachers in 'Gymnasium Schloss Overhagen' for their help, their motivation, and for giving me a chance to finish my German Abitur.

My best friend Trong Nhan Le for his motivation, his discussions about life, philosophy and religions.

And finally, my beloved sisters and brother, who always give me love, support, believe in me and stand by my side. There is nobody else or nothing else I want to be than your oldest sister.

Band / Volume 246
Nanostructured Si-alloys for silicon solar cells
K. Ding (2015), 210 pp
ISBN: 978-3-95806-024-1

Band / Volume 247
Electrochemical Texturing and Deposition of Transparent Conductive Oxide Layers for the Application in Silicon Thin-Film Solar Cells
J.-P. Becker (2015), ix, 156, XXIV pp
ISBN: 978-3-95806-027-2

Band / Volume 248
Stoffliche Charakterisierung radioaktiver Abfallprodukte durch ein Multi-Element-Analyseverfahren basierend auf der instrumentellen Neutronen-Aktivierungs-Analyse – MEDINA –
A. W. Havenith (2015), 311 pp
ISBN: 978-3-95806-033-3

Band / Volume 249
Quantitative Two-Layer Inversion and Customizable Sensor-Array Instrument for Electromagnetic Induction based Soil Conductivity Estimation
A. T. Mester (2015), viii, 119 pp
ISBN: 978-3-95806-035-7

Band / Volume 250
Partial Neutron Capture Cross Sections of Actinides using Cold Neutron Prompt Gamma Activation Analysis
C. Genreith (2015), vii, 166, XXXII pp
ISBN: 978-3-95806-036-4

Band / Volume 251
Long Term Aerosol Composition Measurements at the CESAR Tower at Cabauw, NL
P. Schlag (2015), iii, 228 pp
ISBN: 978-3-95806-037-1

Band / Volume 252
Modellbasierte Spezifikationsmethodik zur effizienten Systementwicklung von Brennstoffzellenantrieben
R. Biurrun Sotelo (2015), 255 pp
ISBN: 978-3-95806-038-8

Band / Volume 253
Three-dimensional ray-tracing simulations of convective gravity waves
S. Kalisch (2015), iii, 183 pp
ISBN: 978-3-95806-040-1

Band / Volume 254
First-Principles Study on Pyrites and Marcasites for Photovoltaic Application
T. Schena (2015), 206 pp
ISBN: 978-3-95806-041-8

Band / Volume 255
Glass-Ceramic Sealant Reinforcement for High-Temperature Applications
B. Cela Greven (2015), xi, 119 pp
ISBN: 978-3-95806-042-5

Band / Volume 256
Entwicklung planarer $Ba_{0,5}Sr_{0,5}Co_{0,8}Fe_{0,2}O_{3-\delta}$-Membranmodule zur Sauerstoffabtrennung und Analyse ihres Transportverhaltens
P. Niehoff (2015), VIII, 134 pp
ISBN: 978-3-95806-044-9

Band / Volume 257
Extension of the Reactor Dynamics Code MGT-3D for Pebble-bed and Block-type High-Temperature-Reactors
D. Shi (2015), x, 162 pp
ISBN: 978-3-95806-045-6

Band / Volume 258
Failure Analysis of Thin Film Solar Modules using Lock-in Thermography
M. Siegloch (2015), XIII, 131 pp
ISBN: 978-3-95806-047-0

Band / Volume 259
Relation between growth rate, material quality, and device grade condition for intrinsic microcrystalline silicon:
From layer investigation to the application to thin-film tandem solar cells
S. Michard (2015), vi, 184 pp
ISBN: 978-3-95806-048-7

Band / Volume 260
Quantitative analysis of spatially resolved electroluminescence of $Cu(In,Ga)Se_2$ and a-Si:H thin-film solar cells and modules
T. Tran (2015), iii, 161 pp
ISBN: 978-3-95806-050-0

Weitere ***Schriften des Verlags im Forschungszentrum Jülich*** unter
http://wwwzb1.fz-juelich.de/verlagextern1/index.asp

Energie & Umwelt /
Energy & Environment
Band / Volume 260
ISBN 978-3-95806-050-0